

SALTS IN THE AIR AND WATER UNDERSTANDING THEIR FORMATION
MECHANISM, REACTIONS AND THEIR ADVANTAGES AND DISADVANTAGES

by

Mojtaba AzadiAghdam

Copyright © Mojtaba AzadiAghdam 2019

A Dissertation Submitted to the Faculty of the

DEPARTMENT OF CHEMICAL AND ENVIRONMENTAL ENGINEERING

In Partial Fulfillment of the Requirements

For the Degree of

DOCTOR OF PHILOSOPHY

WITH A MAJOR IN CHEMICAL ENGINEERING

In the Graduate College

THE UNIVERSITY OF ARIZONA

2019

THE UNIVERSITY OF ARIZONA
GRADUATE COLLEGE

As members of the Dissertation Committee, we certify that we have read the dissertation prepared by Mojtaba AzadiAghdam, titled Salts in the Air and Water Understanding their Formation Mechanism, Reactions and their Advantages and Disadvantages and recommend that it be accepted as fulfilling the dissertation requirement for the Degree of Doctor of Philosophy.

James Farrell Date: 8/13/19
James Farrell

Armin Sorooshian Date: 8/13/19
Armin Sorooshian

Andrea Achilli Date: 8/13/19
Andrea Achilli

Kerri Hickenbottom Date: 8/13/19
Kerri Hickenbottom

Final approval and acceptance of this dissertation is contingent upon the candidate's submission of the final copies of the dissertation to the Graduate College.

We hereby certify that we have read this dissertation prepared under our direction and recommend that it be accepted as fulfilling the dissertation requirement.

James Farrell Date: 8/13/19
James Farrell
Dissertation Committee Co-Chair
Department of Chemical and Environmental Engineering

Armin Sorooshian Date: 8/13/19
Armin Sorooshian
Dissertation Committee Co-Chair
Department of Chemical and Environmental Engineering

ACKNOWLEDGEMENT

I would like to thank my advisors Dr. James Farrell and Dr. Armin Sorooshian for their immense support throughout my graduate studies.

DEDICATION

Dedicated to my mother who has patiently endured many years of being separated from her son so that he can pursue his goals.

TABLE OF CONTENT

LIST OF FIGURES	7
LIST OF TABLES	9
ABSTRACT	10
INTRODUCTION	12
CHAPTER 1: ON THE NATURE OF SEA SALT AEROSOL AT A COASTAL MEGACITY: INSIGHTS FROM MANILA, PHILIPPINES IN SOUTHEAST ASIA	13
Abstract	14
Introduction.....	16
Materials and Methods.....	17
Study Site Description	17
Size-Resolved Aerosol Measurements: July – December 2018	19
PM _{2.5} and PM _{coarse} Measurements: August 2005 – October 2007	22
Meteorological Data.....	22
Transport Modeling.....	23
κ -Köhler Theory.....	23
Calculations Related to Sea Salt	25
Results and Discussion	29
Relationships Between Sea Salt and Meteorology	29
Speciated Mass Size Distributions.....	31
Sea Salt Reactivity	33
Sea Salt Enrichment Factor Analysis.....	40
Hygroscopicity Analysis	44
Particle Morphology	48
Conclusions.....	50
CHAPTER 2: PRETREATMENT OF SECONDARY EFFLUENT FOR WATER REUSE	52
Abstract.....	53
Introduction.....	54
Materials and Method	59
Secondary Effluent.....	59

Materials.....	60
Equipment	60
Analytical Methods	60
Results and Discussion	63
Treatment Technologies.....	63
NOM Characterization for Discussed Treatment Technologies Using Parallel Factor (PARAFAC) Analysis Method	81
Conclusions.....	86
APPENDIX A – SUPPLEMENTARY MATERIAL	89
REFERENCES	96

LIST OF FIGURES

Figure 1 Location of the sample station at the Manila Observatory (MO) marked with red circle in Metro Manila, Philippines, with an additional inset map showing a wider region of the Philippines. The two rectangles represent different spatial domains over which precipitation data were obtained for comparison to the aerosol data collected at MO.

..... 18

Figure 2 MOUDI set averages of both nssNa^+ and ssNa^+ , as calculated using Equations 2-5. On the right y-axis are % Cl^- depletion values based on using total Na^+ ('Old method') and ssNa^+ ('New method'). 27

Figure 3 Air mass back-trajectories associated with MOUDI sample sets that are colored by their A) ssNa^+ and B) Cl^- concentrations at the sample site in Metro Manila.... 31

Figure 4 Mass size distributions of A) total Na^+ and Cl^- , and B) acids participating in Cl^- depletion reactions (nss and ex SO_4^{2-} , NO_3^- , organic acids) for all MOUDI sets except set 9. Set MO9 (presented with cross markers in panel A) exhibits peculiarly different behavior with a more pronounced peak in the submicrometer range for Na^+ 32

Figure 5 Water-soluble mass concentrations associated with different species categorized based on the five types of pollution characteristics. On the right y-axis is the % Cl^- depletion for each category. The 'organic acids' category includes carboxylic acids (Pyruvate, Adipate, Succinate, Maleate, Oxalate, Phthalate) and MSA. 'Other species' includes all the elements analyzed using IC and ICP-QQQ (listed in Section 2.2) that are not shown in this figure. 36

Figure 6 Average mass size distributions for Cl^- and the % Cl^- depletion for the five different pollutant categories: A) Clean, B) Highest Rain, C) Fire, D) Background and E) Continental Pollution. The bars correspond to left y-axis and lines with markers refer to the right y-axis..... 37

Figure 7 A) Volume fraction of different aerosol constituents for each MOUDI stage based on the cumulative average of all sets in Table 1. B) Corresponding κ values for

each stage as an average of all MOUDI sets. The categories in panel A refer to species defined in Table S2: “Low κ Organic Acids” include CaOxalate, MgOxalate, and ZnOxalate; “High κ Organic Acids” include Na₂Oxalate; “Low κ Inorganics” include Ca₂SO₄ and MgSO₄; “High κ Inorganics” include (NH₄)₂SO₄, K₂SO₄, Mg(NO₃)₂, NaNO₃, Na₂SO₄, CaCl₂, MgCl₂, and Ca(NO₃)₂; and “Organics” include all organics not contained in the two organic acid categories. 46

Figure 8 Size-resolved SEM-EDX characterization of representative particles containing Na and Cl collected at MO on 1 August 2018. The panels correspond to MOUDI stages with the following D_p ranges: (A/B) 1.8-3.2 μ m; (C/D) 3.2 – 5.6 μ m; (E/F) 5.6-10 μ m. Also shown for each substrate sample are O, Na and Cl distributions in the individual particles based on EDX analysis. 49

Figure 9 A) Mg, B) Ca and C) Silica removal rates at different pH values in FBCR..... 66

Figure 10 TOC concentrations of secondary effluent treated by FBCR. 69

Figure 11 EEM figures for each stage at four different pH values 73

Figure 12 SEC-OCD results for SE treated by FBCR at different pH values..... 75

Figure 13 EEM spectra for filtered and unfiltered SE, UF permeate and UF backwash. 77

Figure 14 TOC, DOC, pH value and dissolved Fe concentration for different doses of FeCl₃ for A) 20 min flocculation and B) 30 min flocculation 78

Figure 15 EEM spectra for selected Fe doses as FeCl₃ 80

Figure 16 Contour plots of five different components identified from the EEM spectra of FBCR, UF and FeCl₃ coagulation and flocculation samples using PARAFAC 82

Figure 17 F_{max} values for different conditions in A) FBCR, B) UF and C) FeCl₃ coagulation and flocculation 85

LIST OF TABLES

Table 1 Summary of MOUDI sample set details and associated meteorological conditions, total resolved water-soluble mass concentrations, and sum of ssNa^+ and Cl^-	19
Table 2 Comparison of $\text{Cl}^-:\text{ssNa}^+$ for wet and dry seasons and weekend (Saturday and Sunday) and weekdays (Monday-Friday). Data points with $\text{Ex SO}_4^{2-} < 0$ are excluded for the five columns on the right.	33
Table 3 The percent contribution attributable to different species to Cl^- depletion for different sample set categories based on pollution characteristics.	39
Table 4 Sea salt enrichment factor (ssEF) values calculated using Equation 10. ssNa^+ is used as the reference species in the sample and the control. The concentrations used in this analysis represent the sum from the three MOUDI stages (cutpoint $D_p = 1, 1.8, 3.2 \mu\text{m}$) with the highest sea salt concentrations. MO9 is not shown in the table since the ssNa^+ concentrations for all the cutpoints above $1 \mu\text{m}$ is zero.	42
Table 5 Secondary effluent water quality	59
Table 6 Highest SI values and Turbidity for different pH values in FBCR compared to secondary effluent	64
Table 7 Excitation-emission boundaries for five operationally-defined fluorescence region	70
Table 8 Turbidity, TOC and inorganic cations' concentration in UF treatment.....	76
Table 9 Comparison of the identified components of this study with previous studies...	82

ABSTRACT

This study utilizes multiple aerosol datasets collected in Metro Manila, Philippines to investigate sea salt aerosol characteristics. This coastal megacity allows for an examination of the impacts of precipitation and mixing of different air masses on sea salt properties, including overall concentration and size-resolved composition, hygroscopicity, and morphology. Intensive size-resolved measurements with a Micro-Orifice Uniform Deposit Impactor (MOUDI) between July-December 2018 revealed the following major results: (i) sea salt levels exhibit wide variability during the wet season, driven primarily by precipitation; (ii) ssNa^+ and Cl^- peaked in concentration between 1.8 – 5.6 μm , with Cl^- depletion varying between 21.3 - 90.7%; (iii) mixing of marine and anthropogenic air masses yielded complex non-spherical shapes with species attached to the outer edges and Na^+ uniformly distributed across particles unlike Cl^- ; (iv) there was significant contamination of sea salt aerosol by a variety of crustal and anthropogenic pollutants (Fe, Al, Ba, Mn, Pb, NO_3^- , V, Zn, NH_4^+); (v) categorization of samples in five different pollutant type categories (Background, Clean, Fire, Continental Pollution and Highest Rain) revealed significant differences in overall Cl^- depletion with enhanced depletion in the submicrometer range versus the supermicrometer range; (vi) κ values ranged from 0.02 to 0.31 with a bimodal profile across all stages, with the highest value coincident with the highest sea salt volume fraction in the 3.2-5.6 μm stage, which is far lower than pure sea salt due to the significant influence of organics and black carbon. Analysis of longer term $\text{PM}_{2.5}$ (particulate matter with aerodynamic diameter less than 2.5 μm) and $\text{PM}_{\text{coarse}}$ ($= \text{PM}_{10} - \text{PM}_{2.5}$) data between August 2005 and October 2007 confirmed findings from the MOUDI data that more Cl^- depletion occurred both in the wet season versus the dry season and on weekdays versus weekend days.

The effectiveness of three different pretreatment processes (Fluidized bed crystallization reactor, Ultrafiltration and ferric chloride coagulation and flocculation) in order to remove scale-forming and fouling substances from the wastewater secondary effluent were

studied. At optimized conditions, fluidized bed crystallization reactor (FBCR) was able to remove >99.9% of magnesium, 97% of calcium and 42% of silica while ultrafiltration (UF) and ferric chloride coagulation were only able to remove 18% and 16% of the silica concentration, respectively. UF was also able to reduce the turbidity of the SE by 93%. Furthermore, the co-precipitation of different mineral salts with organic matter were also discussed using size exclusion chromatography-organic carbon detector (SEC-OCD). At optimized conditions, ferric chloride resulted in the highest natural organic matter (NOM) reduction (56%) compared to FBCR (26%) and UF (13%). Excitation emission matrix-parallel factor (EEM-PARAFAC) analysis were used to characterize the NOM in the SE and the effluent of these pretreatments. Five different components (three humic substance, one fulvic acid and one protein-like) were detected. FBCR (7-100%) and ferric chloride (26-65%) were able to remove from all 5 types of NOM while UF was only able to reduce the concentration of the protein-like NOM (11%).

INTRODUCTION

This dissertation uses a manuscript-based style to discuss 2 studies that will be submitted for publication in peer-reviewed journals.

Chapter one discusses the nature of sea salt aerosol at a coastal megacity: insights from manila, Philippines in southeast Asia. As one of the most abundant aerosol types globally on a mass basis, sea salt has far-reaching impacts on the planet including scattering of light, geochemical cycling of nutrients, exchanging moisture with the atmosphere, and serving as cloud condensation nuclei (CCN) to impact clouds and the water cycle. Chapter one discusses the nature of the sea salt and chloride depletion which negatively affects the CCN.

Chapter two discusses the presence of sea salt as well as other salts in the water that are required to be removed prior to delivering the water as potable water. In this chapter, several treatment options are discussed and their efficiency in removing variety of salts and organic contaminants are discussed.

While the presence of sea salt has positive impact on initiating the CCN, these salts are needed to be removed in the drinking water that is being delivered to point-of-use. Both these matter in aerosol and water are discussed in the following chapters including discussions in formation and mechanisms of removal these salts.

**CHAPTER 1: ON THE NATURE OF SEA SALT AEROSOL AT A
COASTAL MEGACITY: INSIGHTS FROM MANILA, PHILIPPINES
IN SOUTHEAST ASIA**

This chapter is submitted for publication in the journal of atmospheric environment.

Abstract

This study utilizes multiple aerosol datasets collected in Metro Manila, Philippines to investigate sea salt aerosol characteristics. This coastal megacity allows for an examination of the impacts of precipitation and mixing of different air masses on sea salt properties, including overall concentration and size-resolved composition, hygroscopicity, and morphology. Intensive size-resolved measurements with a Micro-Orifice Uniform Deposit Impactor (MOUDI) between July-December 2018 revealed the following major results: (i) sea salt levels exhibit wide variability during the wet season, driven primarily by precipitation; (ii) ssNa^+ and Cl^- peaked in concentration between 1.8 – 5.6 μm , with Cl^- depletion varying between 21.3 - 90.7%; (iii) mixing of marine and anthropogenic air masses yielded complex non-spherical shapes with species attached to the outer edges and Na^+ uniformly distributed across particles unlike Cl^- ; (iv) there was significant contamination of sea salt aerosol by a variety of crustal and anthropogenic pollutants (Fe, Al, Ba, Mn, Pb, NO_3^- , V, Zn, NH_4^+); (v) categorization of samples in five different pollutant type categories (Background, Clean, Fire, Continental Pollution and Highest Rain) revealed significant differences in overall Cl^- depletion with enhanced depletion in the submicrometer range versus the supermicrometer range; (vi) κ values ranged from 0.02 to 0.31 with a bimodal profile across all stages, with the highest value coincident with the highest sea salt volume fraction in the 3.2-5.6 μm stage, which is far lower than pure sea salt due to the significant influence of organics and black carbon. Analysis of longer term $\text{PM}_{2.5}$ (particulate matter with aerodynamic diameter less than 2.5 μm) and $\text{PM}_{\text{coarse}}$ ($= \text{PM}_{10} - \text{PM}_{2.5}$) data between August 2005 and October 2007 confirmed findings from the MOUDI data that more Cl^- depletion occurred both in the wet season versus the dry season and on weekdays versus weekend days. This study demonstrates the importance of accounting for two factors in future studies on sea salt: (i) non-sea salt (nss) sources of Na^+ impact calculations such as for Cl^- depletion that typically assume that total Na^+ concentration is derived from salt; and (ii) a stronger anti-relationship between rainfall

accumulation and sea salt concentration at the study site was observed when rain data was used over a larger spatial domain rather than a point measurement at the study site, indicative of the importance of considering scavenging impacts on salt during its transport to a measurement site.

Introduction

As one of the most abundant aerosol types globally on a mass basis (Liao et al., 2006) sea salt has far-reaching impacts on the planet including scattering of light, geochemical cycling of nutrients, exchanging moisture with the atmosphere, and serving as cloud condensation nuclei (CCN) to impact clouds and the water cycle (Lewis and Schwartz, 2004). Sea salt is also significant with regard to halogen chemistry in the atmosphere as the reactions of acids with sea salt particles can lead to emissions of reactive iodine, bromine, and chlorine (Chameides and Stelson, 1992). Sea salt is estimated to account for ~30% of global aerosol optical depth (Bellouin et al., 2013), with most studies investigating its behavior near the surface or within the boundary layer owing to such low levels in the upper troposphere, which is far-removed from its sources at the surface (Murphy et al., 2019). Sea salt's strong vertical gradient qualifies this aerosol type as especially important for studying wet scavenging processes, which is an area requiring improvement in atmospheric models (MacDonald et al., 2018; Murphy et al., 2019).

Two important aspects of atmospheric sea salt requiring further research are the nature of its mixing with other pollutant types and its sensitivity to precipitation. Southeast Asia is a prime candidate region for the study of these two topics due to extensive precipitation during parts of the year (e.g., Southwest Monsoon (SWM) season), extensive issues with air pollution, and numerous growing coastal megacities in the region. One such coastal megacity is Metro Manila, Philippines, with a population of 12.88 million (Philippine Statistics Authority, 2015). This urban area is impacted by long-range transport from other countries in Southeast and East Asia and has significant local emissions (e.g., vehicular traffic, industrial activity, burning, waste processing, smelting). Studying aerosol properties when these non-marine air masses mix with sea salt is important owing to poorly understood chemical changes in particles upon such mixing. For example, there can be depletion of particulate species (e.g., Fe, Cl) when marine air mixes with plumes from ships and wildfires (Braun et al., 2017; Sorooshian et al., 2013)

while methanesulfonate levels tend to be higher when fire plumes mix with marine air as compared to either air mass type alone (Sorooshian et al., 2015).

The goal of this work is to report on size-resolved properties of aerosol during an intensive period of measurements between July – December 2018, in addition to a longer-term dataset (August 2005 – October 2007) of PM_{2.5} (particulate matter with aerodynamic diameter less than 2.5 μm) and PM₁₀ composition. The following questions will be addressed: (i) how does the concentration of sea salt vary as a function of particle size and what are size-resolved morphological traits of these particles?; (ii) how do sea salt concentrations differ across different temporal scales and as a function of meteorological parameters such as precipitation accumulation?; (iii) how does chloride depletion depend on particle size and what species are most responsible?; (iv) what are the size-resolved hygroscopic properties of sea salt-containing particles?; and (v) what is the general impact of sea salt mixing with other pollutant types? The implications of the subsequently discussed results extend to improved understanding of sea salt properties, their chemical reactivity, and the role of wet scavenging in modifying surface layer PM concentrations in urban regions. These findings are relevant for modeling, remote sensing applications, and for contrasting with other regions to determine how reproducible our results are in other areas.

Materials and Methods

Study Site Description

Measurement data used in this study were collected in Quezon City, Philippines at the Manila Observatory (MO; 14.64° N, 121.08° E) (Figure 1). The site represents a coastal megacity with influence from long-range transport of pollution, marine emissions, and a variety of regional urban sources such as vehicular emissions, industrial activity, waste processing, and burning (Cohen et al., 2009). The study includes data from two different periods, including a longer-term characterization of PM_{2.5} and PM₁₀ between 14 August 2005 – 23 October 2007 and a more intensive period of size-resolved PM measurements between 19 July 2018 – 7 December 2018. The latter period is associated with the year-

long study referred to as the Cloud, Aerosol, and Monsoon Processes Philippines Experiment (CAMP²Ex) weatHER and CompoSition Monitoring (CHECSM) study. For the purposes of subsequent discussion, data are divided between wet (June – October) and dry (November – May) seasons based on the degree of influence from monsoonal precipitation. However, it is noted that there can be variability in the onset and end of these periods (Bagtasa et al., 2018; Cruz et al., 2013).

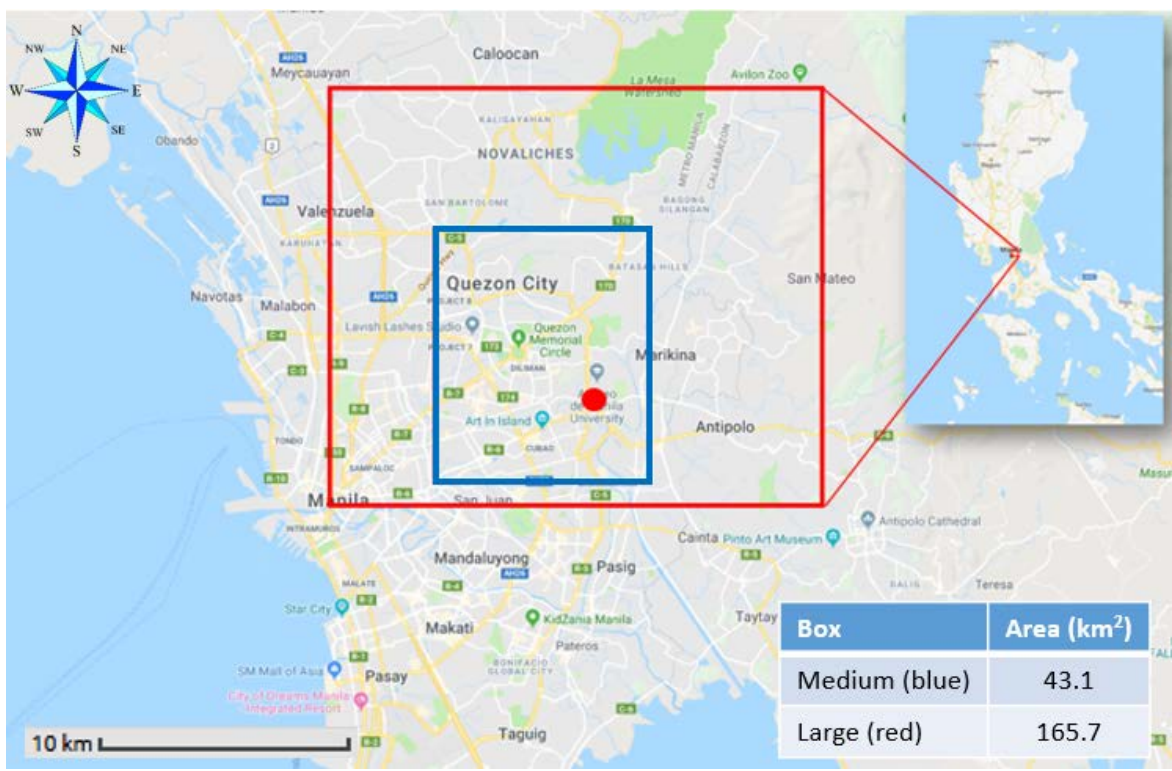


Figure 1 Location of the sample station at the Manila Observatory (MO) marked with red circle in Metro Manila, Philippines, with an additional inset map showing a wider region of the Philippines. The two rectangles represent different spatial domains over which precipitation data were obtained for comparison to the aerosol data collected at MO.

Size-Resolved Aerosol Measurements: July – December 2018

Sample collection and extraction

Between 19 July and 7 December 2018, 21 sets of samples (Table 1) were collected by two separate Micro-Orifice Uniform Deposit Impactors (MOUDI, MSP Corporation) (Marple et al., 2014) on the 3rd floor of the MO office building (~85 m above sea level). These measurements cover the SWM season (MO1 – MO16) and then, beginning with set MO17, the transition into the dry season that typically begins in November. The MOUDIs collected aerosol particles on substrates with the following aerodynamic cutpoint diameters (D_p): 18, 10, 5.6, 3.2, 1.8, 1.0, 0.56, 0.32, 0.18, 0.10, 0.056 μm . For the 21 MOUDI sets, Teflon substrates (PTFE membrane, 2 μm pore, 46.2 mm, Whatman) were used. There were two special instances when two MOUDI sets were simultaneously collected with the two individual MOUDI instruments for the purpose of conducting different types of analyses (i.e., chemical analysis versus gravimetric analysis) on the separate sets of substrates. One additional MOUDI set collected on 1 August 2018 (11:53 – 13:00 local time; not shown in Table 1) was collected using aluminum substrates for the purpose of microscopy analysis.

Table 1 Summary of MOUDI sample set details and associated meteorological conditions, total resolved water-soluble mass concentrations, and sum of ssNa^+ and Cl^- .

<i>Sample set name</i>	Sampling dates	Duration (h)	Flow rate (L/min)	Wind speed (m s⁻¹)	Wind direction (°)	T (°C)	Rain (mm)	Water-soluble mass (µg m⁻³)	ssNa⁺ + Cl⁻ (µg m⁻³)
<i>MO1</i>	Jul 19-20	24	30	3.3	90.1	24.9	29.1	4.6	0.6
<i>MO2</i>	Jul 23-25	54	30	1.3	95.8	26.7	13.1	6.5	0.1
<i>MO3/4</i>	Jul 25-30	119	28/30	1.2	111.8	26.7	16.1	5.2	0.6
<i>MO5</i>	Jul 30-Aug 1	42	29	2.6	98.1	27.5	15.3	9.2	1.1
<i>MO6</i>	Aug 6-8	48	27	0.9	127.5	26.1	40.2	5.1	0.5
<i>MO7</i>	Aug 14-16	48	28	3.0	107.8	27.8	3.3	13.7	2.6
<i>MO8</i>	Aug 22-24	48	29	3.5	108.7	28.1	12.2	12.8	1.5
<i>MO9</i>	Sep 1-3	48	27	0.7	98.6	26.6	44.8	6.2	0.2
<i>MO10</i>	Sep 10-12	48	29	1.0	94.7	26.2	34.1	6.4	0.2
<i>MO11</i>	Sep 18-20	48	27	0.5	290.2	27.8	31.2	2.7	0.4
<i>MO12</i>	Sep 26-28	48	27	1.2	96.3	27.8	4.3	13.5	2.2
<i>MO13/14</i>	Oct 6-8	48	30/26	0.6	108.2	27.8	1.6	16.6	0.6
<i>MO15</i>	Oct 15-17	48	30	0.4	157.7	27	30.5	5.1	0.1
<i>MO16</i>	Oct 23-25	48	29	0.7	229.2	28.1	0	7.2	0.6
<i>MO17</i>	Nov 6-8	48	30	1.3	71.4	27.7	0.1	4.9	1.5
<i>MO18</i>	Nov 10-12	48	29	1.2	68	27.5	20.4	6.1	0.9
<i>MO19</i>	Nov 19-21	48	31	1.5	30.7	27.4	0	4.5	1.1
<i>MO20</i>	Nov 27-29	48	30	1.1	44.3	27.2	0	5.9	1.7
<i>MO21</i>	Dec 5-7	48	31	1.2	94.4	27.8	29.1	4.3	0.6

With the exception of MOUDI sets MO3 and MO13, Teflon substrates were cut in half with one half stored in a freezer and the other half placed in a sealed polypropylene vial with 8 mL of 18.2 M Ω -cm Milli-Q water and sonicated for 30 min.

Sample analyses

The resulting aqueous extract was then chemically analyzed with ion chromatography (IC; Thermo Scientific Dionex ICS - 2100 system) for water-soluble ions and triple quadrupole inductively coupled plasma mass spectrometry (ICP-QQQ; Agilent 8800 Series) for water-soluble elements. All of the reagents and tuning solutions were procured from Agilent. Samples were acidified using 2% nitric acid before analysis. Blank samples were processed the same way as the measurement samples, with blank concentrations subtracted from sample concentrations. The IC species discussed in this work include Na⁺, NH₄⁺, Mg²⁺, Ca²⁺, amines (the sum of dimethylamine, diethylamine, and trimethylamine), methanesulfonate (MSA), pyruvate, adipate, succinate, maleate, oxalate, phthalate, Cl⁻, NO₃⁻, and SO₄²⁻. The ICP species discussed here include K, Al, Fe, Mn, Ti, Ba, Zn, Cu, V, Ni, P, Cr, Co, As, Se, Rb, Sr, Y, Zr, Nb, Mo, Ag, Cd, Sn, Cs, Hf, Tl, and Pb. References in this study to total water-soluble mass refer to the concentration sum of the aforementioned IC and ICP species. Table S1 reports the limit of detection (LOD) of these species as calculated with the method of Miller and Miller (2000). Sets MO3 and MO13 underwent gravimetric analysis with a Sartorius ME5-F microbalance. Details associated with the LODs associated with these measurements are reported by Cruz et al. (2019) for the same dataset.

Aluminum substrates from the one collected microscopy set were analyzed for morphology and elemental composition with a Hitachi S-4800 High Resolution Scanning Electron Microscopy (SEM) equipped with a Thermo Noran system Six Energy Dispersive X-ray Spectrometer (EDX) in the Kuiper Imaging Cores Facility at the University of Arizona. For SEM-EDX analysis, a small section was cut from the center of substrates and taped on a sample stub with double-sided carbon tape. Samples were analyzed under vacuum without sputtering coating. During analysis, particles were randomly selected and

examined by 30 eV acceleration voltage and 100-125 μA probe current under high magnification mode. EDX data were obtained after SEM analysis for determining chemical composition of individual particles. As a blank substrate contains Al (~91.5%), C (~5.4%), Ag (~2.1%), and O (~0.9%), these elements cannot be evaluated for quantitative purposes.

PM_{2.5} and PM_{coarse} Measurements: August 2005 – October 2007

To complement the shorter term MOUDI data, longer term data (14 August 2005 – 23 October 2007) are analyzed here to understand temporally relevant characteristics over the course of an annual cycle. These measurements were collected at 3 m above ground level at MO. Two Airmetrics Minivol samplers were used to simultaneously collect PM_{2.5} and PM₁₀ samples using 47 mm diameter ringed Teflon substrates and an Andersen Dichotomous sampler was used to collect another pair of PM_{2.5} and PM_{coarse} (i.e., PM₁₀-PM_{2.5}) samples using 37 mm diameter ringed Teflon substrates. Samplers were programmed to run for 24 h periods beginning at midnight. Substrate samples were individually extracted in 25 ml of 18.2 M Ω -cm Milli-Q water via sonication for 1 h. A Dionex ICS-1000 ion chromatography system was then used for speciation and quantification of the following ions: F⁻, Cl⁻, NO₂⁻, Br⁻, NO₃⁻, PO₄³⁻, SO₄²⁻, Li⁺, Na⁺, NH₄⁺, K⁺, Mg²⁺, Ca²⁺.

Meteorological Data

Meteorological data were collected using a Davis Vantage Pro 2 Plus weather station co-located with the aerosol measurements at MO. Rain amounts were extracted from the Precipitation Estimation from Remotely Sensed Information using Artificial Neural Networks—Cloud Classification System (PERSIANN-CCS) dataset, which is available from the University of California Irvine Center for Hydrometeorology and Remote Sensing (CHRS) Data Portal (<http://chrsdata.eng.uci.edu>) (Nguyen et al., 2019). The PERSIANN-CCS algorithm extracts local and regional cloud features (coldness,

geometry, texture) from infrared geostationary satellite imagery for estimating rainfall at $0.04^\circ \times 0.04^\circ$ spatial resolution every 30 minutes. More details about PERSIANN-CCS can be found in Hong et al. (2004). Nguyen et al. (2014) showed that PERSIANN-CCS successfully captured heavy rainfall of Typhoon Haiyan over the Philippines in November 2013. In order to study the impact of spatial domain of rain data on aerosol concentrations, data were collected over three spatial domains (Figure 1): point location at MO = 14.64° N, 121.08° E; medium box = $14.61^\circ - 14.69^\circ$ N, $121.02^\circ - 121.10^\circ$ E; large box = $14.60^\circ - 14.74^\circ$ N, $120.98^\circ - 121.16^\circ$ E. Unless otherwise noted, references to rain accumulation are in reference to the latter large box.

Transport Modeling

In order to assess the impacts of synoptic and regional scale transport on sea salt concentration at MO, 96 h back-trajectories were obtained from the Hybrid Single-Particle Lagrangian Integrated Trajectory (HYSPLIT) model (Rolph et al., 2017; Stein et al., 2015) ending 500 m above ground level at the MO (14.64° N, 121.08° E) sampling site. For each sampling period, trajectories were obtained every 6 h using the National Centers for Environmental Prediction/National Center for Atmospheric Research (NCEP/NCAR) reanalysis data with the “Model vertical velocity” method.

κ -Köhler Theory

One of the goals of this study was to quantify relative differences in hygroscopicity as a function of particle diameter with a focus on MOUDI stages most enhanced with sea salt. A common way to quantify hygroscopicity is with the single parameter kappa, κ (Petters and Kreidenweis, 2007). For multicomponent aerosol, an overall κ for each stage of individual MOUDI sets is calculated using a mixing rule approach. More specifically, the Zdanovskii, Stokes, and Robinson (ZSR) method (Stokes and Robinson, 1966; Zdanovskii, 1948) assists in finding κ by weighing each species' κ_i by its volume fraction, ε_i :

$$\kappa = \sum_i \varepsilon_i \kappa_i \quad (1)$$

In the present study, the water-soluble components were measured as individual ions. However, since κ values are documented for compounds, not ions, in the literature, the measured ions needed to be allotted into their original compounds. This was done using an established ion pairing scheme (Gysel et al., 2007), which uses individual species concentrations to derive compound concentrations. In addition to the water-soluble fraction, water-insoluble organics and black carbon (BC) contribute significantly to ambient PM. For set MO13, total mass, BC mass, and water-soluble concentrations were known (Cruz et al., 2019); note that BC was measured with a Multi-wavelength Absorption Black Carbon Instrument (MABI; Australian Nuclear Science and Technology Organisation), which is an optically-based technique from which data were used based on absorption at 870 nm (Cruz et al., 2019) The remaining mass was attributed to water-insoluble organics. In order to derive a κ more representative of ambient PM, probable concentrations of water-insoluble organics and BC were applied to all other MOUDI sets using the relative fractions of these two components found in set MO13. Although such scaling is not fully accurate across all the MOUDI sets, it provides some sense of more realistic values with the assumption that both the relative amount of emissions of all aerosol species (and precursors) and the rates of formation and removal were stable throughout the study period. As noted by Cruz et al. (2019), the qualitative trend in BC concentration across the MOUDI stages was consistent for all sets collected. For inclusion into Equation 1, values of density and κ were adopted from the literature for each pure compound, including water-insoluble organics and BC (Table S2).

Calculations Related to Sea Salt

While in marine environments aerosol Na^+ and Cl^- are typically attributed to marine emissions, due to their abundance in sea salt (ss), there can be non-sea salt (nss) contributions to these species as well. Separation of the ss and nss contributions is especially important for Manila as it is impacted by diverse continental and marine emission sources. Examples of sources other than sea salt for Na^+ include biomass burning (Hudson et al., 2004; Silva et al., 1999), dust (Farren et al., 2019) and biological particles (China et al., 2018), the latter of which accounted for ~69% of total Na^+ mass during the wet season in the Amazon basin. Other sources of Cl^- include biomass burning, fossil fuel combustion, industrial activity, and crustal matter (Artaxo et al., 1994; Sorooshian et al., 2011; Wonaschutz et al., 2011; Ye et al., 2003). Airborne measurements by Lee et al. (2003) off the east coast of Asia near the present study region revealed that Cl^- was likely associated with crustal material aloft. Measurements in Shanghai, China suggested that the Cl^- depleted from salt particles can re-enter the aerosol phase via reactions with bases such as ammonia to form smaller salts (Ye et al., 2003).

Following ideas motivated by others ((Becagli et al., 2005; Boreddy and Kawamura, 2015; Farren et al., 2019)), we simultaneously solved Equations 2-5 to obtain ssNa^+ , nssNa^+ , ssCa^{2+} and nssCa^{2+} concentrations based on the average $\text{Ca}^{2+}:\text{Na}^+$ ratios (on a mass basis) in crustal matter and sea water being 1.78 and 0.038, respectively (Becagli et al., 2005; Boreddy and Kawamura, 2015; Bowen, 1979; Farren et al., 2019). This method allows for a more accurate estimate of nssSO_4^{2-} concentration using ssNa^+ in Equation 6 with knowledge that the mass ratio of $\text{SO}_4^{2-}:\text{Na}^+$ in sea water is 0.253 (Becagli et al., 2005; Boreddy and Kawamura, 2015; Farren et al., 2019). Excess (Ex) SO_4^{2-} is quantified using Equation 7, which is the remaining nssSO_4^{2-} after accounting for the amount forming a salt with NH_4^+ (Braun et al., 2017), with the latter portion referred to as “Neutralized SO_4^{2-} ”.

$$\text{ssNa}^+ = \text{Na}^+ - \text{nssNa}^+ \quad (2)$$

$$\text{nssCa}^{2+} = \text{nssNa}^+ \times \left(\frac{\text{Ca}^{2+}}{\text{Na}^+} \right)_{\text{crust}} \quad (3)$$

$$\text{nssCa}^{2+} = \text{Ca}^{2+} - \text{ssCa}^{2+} \quad (4)$$

$$\text{ssCa}^{2+} = \text{ssNa}^+ \times \left(\frac{\text{Ca}^{2+}}{\text{Na}^+} \right)_{\text{sea water}} \quad (5)$$

$$\text{nssSO}_4^{2-} = \text{SO}_4^{2-} - 0.253 \times \text{ssNa}^+ \quad (6)$$

$$\text{Ex SO}_4^{2-} = \text{nss SO}_4^{2-} - \left(\frac{\text{MW}_{\text{sulfate}}}{\text{MW}_{\text{ammonium}}} \right) \times \frac{\text{NH}_4^+}{2} \quad (7)$$

Using MOUDI data, Figure 2 illustrates the impact of using this new approach (referred to as “New method”) to quantify the fraction of Na^+ associated with sea salt as compared to attributing all of the measured Na^+ to sea salt (“Old method”). The range of mass concentrations for ssNa^+ and nssNa^+ using the “New method” were 0-0.51 $\mu\text{g m}^{-3}$ and 0-0.09 $\mu\text{g m}^{-3}$, respectively, with the average ratio of ssNa^+ to total Na^+ being 0.63 ± 0.36 with minimum and maximum values of 0 and 1, respectively. Therefore, there is a non-negligible difference that has an impact on other calculations, such as those described below.

According to Figure 2, Sets 9, 10 and 11 have shown similar total Na^+ concentration with exactly same ssNa^+ concentration. While using old method would result in categorizing these sets as background due to mid-range % Cl^- depletion, the new method demonstrated a wide difference in % Cl^- depletion in a way that the lowest and highest % Cl^- depletion happens in these sets. The possible reasons for this significant difference in Cl^- depletion for these sets with similar total Na^+ concentration is discussed later.

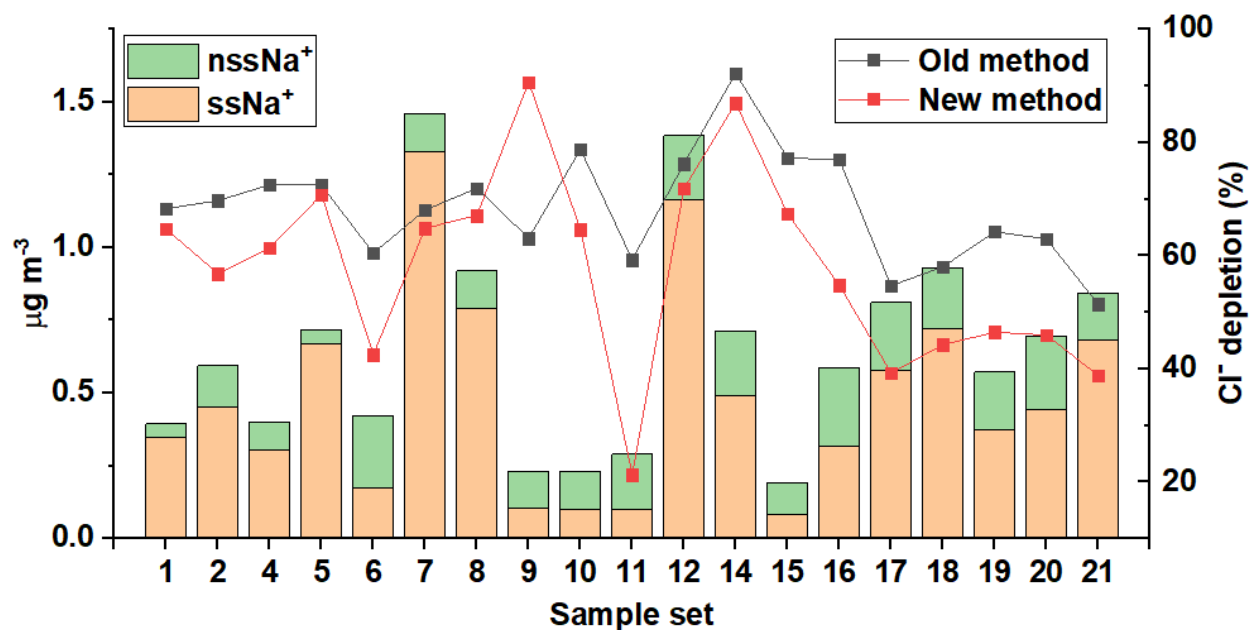


Figure 2 MOUDI set averages of both $nssNa^+$ and $ssNa^+$, as calculated using Equations 2-5. On the right y-axis are % Cl^- depletion values based on using total Na^+ ('Old method') and $ssNa^+$ ('New method').

Marine aerosols often have a lower $Cl^-:ssNa^+$ ratio compared to sea water, which is typically attributed to the release of gaseous Cl to the atmosphere (Martens et al., 1973). An important aspect of this work is quantification of Cl^- depletion owing to reactions of sea salt particles with inorganic and organic acids, leading to the release of gaseous Cl from the aerosol phase. The following equation is used to compute depletion based on the mass ratio of $Cl^-:ssNa^+$ in pure sea water being 1.81 (Martens et al., 1973; Zhao and Gao, 2008):

$$\% Cl^- \text{ depletion} = \frac{(1.81 \times ssNa^+ - Cl^-)}{(1.81 \times ssNa^+)} \times 100\% \quad (8)$$

In instances of the $\text{Cl}^-:\text{ssNa}^+$ ratio exceeding 1.81, $\% \text{Cl}^-$ depletion was considered to be 0% as in other work (Braun et al., 2017). For the MOUDI data analysis, set-averaged $\% \text{Cl}^-$ depletion values reported in this work represent the average of values for individual stages, excluding the first two and last two stages (i.e., 0.056, 0.1, 10, 18 μm) owing to very low ssNa^+ or Cl^- mass concentrations that can result in extreme ratios. Also, if the ssNa^+ value for a given stage was zero, that stage was not considered for calculations of $\% \text{Cl}^-$ depletion, with the presumption that any Cl^- from that stage stemmed from sources other than sea salt. As Cl^- also has nss sources, values of $\% \text{Cl}^-$ depletion discussed subsequently represent a lower bound and thus a conservative value for the degree of sea salt reactivity.

For the longer-term $\text{PM}_{2.5}$ and PM_{10} measurements (Section 2.3), data points with ssNa^+ values equal to 0 were similarly excluded from $\% \text{Cl}^-$ depletion calculations. Furthermore, data points with Cl^- concentrations exceeding a whole set's average plus two times its standard deviation for the entire dataset were also excluded due to the assumption that such samples are biased by nss sources.

The following equation was used to quantify the theoretical maximum amount of Cl^- depletion attributable to specific species (Braun et al., 2017; Song et al., 2018):

$$\% \text{Cl}^- \text{ depletion due to X} = X \times y \times \frac{\left(\frac{\text{MW}_{\text{Cl}^-}}{\text{MW}_X}\right)}{(1.81 \times \text{ssNa}^+ - \text{Cl}^-)} \times 100\% \quad (9)$$

where X is the mass concentration of the acidic species of interest and y signifies the charge of the fully deprotonated conjugate base of X .

Lastly, calculations related to the degree of aging and contamination of sea salt particles were conducted using the following equation for mass-based enrichment factor (EF):

$$\text{Enrichment factor for X} = \frac{\left(\frac{X}{\text{ssNa}^+}\right)_{\text{sample}}}{\left(\frac{X}{\text{ssNa}^+}\right)_{\text{control}}} \quad (10)$$

where X is the species of interest, and ssNa^+ is the reference species. Control values used for the denominator were calculated based on the composition of pure sea water (Seinfeld and Pandis, 2006); for elements with a range of concentrations reported in sea water, the upper bound was used for X in the denominator of Equation 10.

Results and Discussion

Relationships Between Sea Salt and Meteorology

The MOUDI sampling period between 19 July and 7 December 2018 was characterized by widely ranging mass concentrations of sea salt ($0.1 - 2.6 \mu\text{g m}^{-3}$), quantified here as the sum of ssNa^+ and Cl^- for all stages of each MOUDI set (i.e., $D_p \geq 0.056 \mu\text{m}$) (Table 1 and Figure 2). When comparing the MO sets collected in the wet season (July-October; MO1-16) versus subsequent dryer months (November-December; MO17-21), the meteorological parameters in Table 1 exhibiting the largest differences were (wet/dry) rain ($19.7 \pm 15.1/9.9 \pm 13.9 \text{ mm}$) and wind direction ($130 \pm 59/62 \pm 25^\circ$), with less variability in wind speed ($1.35 \pm 1.01/1.26 \pm 0.15 \text{ m s}^{-1}$) and temperature ($27.1 \pm 0.9/27.5 \pm 0.2^\circ \text{C}$). There were three MOUDI sets for which no rain was recorded (MO16, 19, 20). The highest rain accumulation recorded was 44.8 mm for set MO9 (1-3 September). Interestingly, total water-soluble mass was more enhanced in the wet season than the dry season (8.20 ± 4.24 versus $5.14 \pm 0.82 \mu\text{g m}^{-3}$, respectively). In contrast, sea salt showed the opposite behavior (wet season = 0.81 ± 0.78 versus dry season = $1.16 \pm 0.44 \mu\text{g m}^{-3}$), presumably due to factors such as sensitivity of sea salt to wet scavenging (i.e., more removal in wet season). This is further supported by rain accumulation (large box in Figure 1) being less strongly correlated to the overall sum of water-soluble mass ($r = -0.40$) as compared to both sea salt mass ($r = -0.69$) and ssCa^{2+} ($r = -0.72$) (Table S3).

For the three spatial domains in Figure 1 over which precipitation data were collected (point site at MO, medium box, large box), correlations between rain accumulation and sea salt were all significant and negative, with the correlation coefficient

becoming more negative as the domain size grew (MO: $r = -0.51$, $p = 0.03$; medium box: $r = -0.65$, $p < 0.01$; large box: $r = -0.69$, $p < 0.01$). One plausible explanation for the change is that transported PM is impacted by wet scavenging and thus precipitation impacts should be investigated over larger domains rather than with point measurements that are co-located with aerosol monitoring instrumentation.

Sea salt was not well correlated with wind direction ($r = -0.32$, $p = 0.18$), suggesting that local terrain did not lead to significant variability in sea salt levels at MO; note that there are mountains to the east unlike the bay area to the west. Wind speed was positively correlated with sea salt mass ($r = 0.47$, $p = 0.04$) and ssCa^{2+} ($r = 0.96$, $p < 0.01$) (Table S3), which is consistent with what others have observed in different regions (van Pinxteren et al., 2015).

To gain a broader view of air mass transport patterns impacting sea salt rather than local wind speed, Figure 3 shows 96-h back-trajectories colored by ssNa^+ and Cl^- . The trajectories followed a southwesterly flow in the SWM months (July – October), which then transitioned towards northeasterly flow as is typical usually starting in November and extending through the boreal winter months (Bagtasa et al., 2018). The results indicate no preferred direction among the two prevailing trajectory patterns with regard to higher or lower sea salt concentrations. This can be explained by the fact that the source of sea salt surrounds Manila as it is on an island and precipitation (the main sink) extends all around the region.

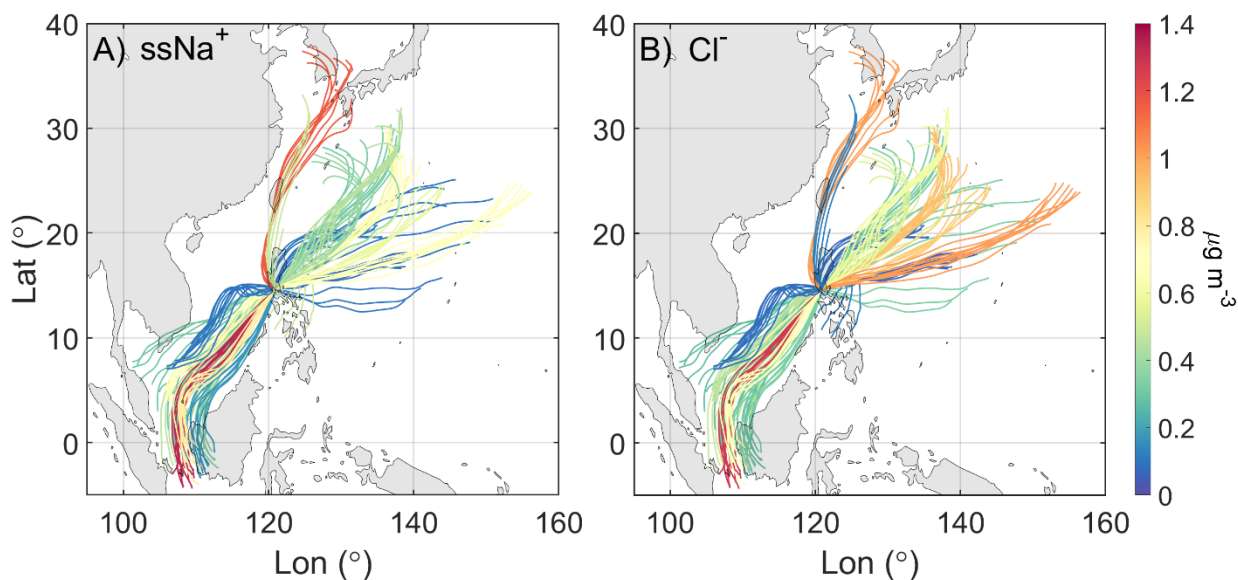


Figure 3 Air mass back-trajectories associated with MOUDI sample sets that are colored by their A) ssNa^+ and B) Cl^- concentrations at the sample site in Metro Manila.

Speciated Mass Size Distributions

Figure 4A reveals that Na^+ and Cl^- were most concentrated in the supermicrometer diameter range with a predominant peak usually between 1.8 – 5.6 μm ; distributions for individual sets are shown in Figure S1. Similar results of sea salt peaking in the supermicrometer diameter range have been demonstrated in a host of other regions such as the Iberian Peninsula, western Europe, the Mediterranean (Quinn et al., 2000), the western coast of the United States (Maudlin et al., 2015; McInnes et al., 1994) and near the Arctic Ocean (Kerminen et al., 1998). Figure 4B shows the mean mass size distributions of the select aerosol-phase acids that can chemically react with sea salt leading to Cl^- depletion. Two of the potential depleting agents (nss SO_4^{2-} and organic acids) exhibited most of their mass in the submicrometer range and peaked between 0.32 – 0.56 μm , while NO_3^- was most concentrated in the supermicrometer range peaking between 1.8 – 3.2 μm .

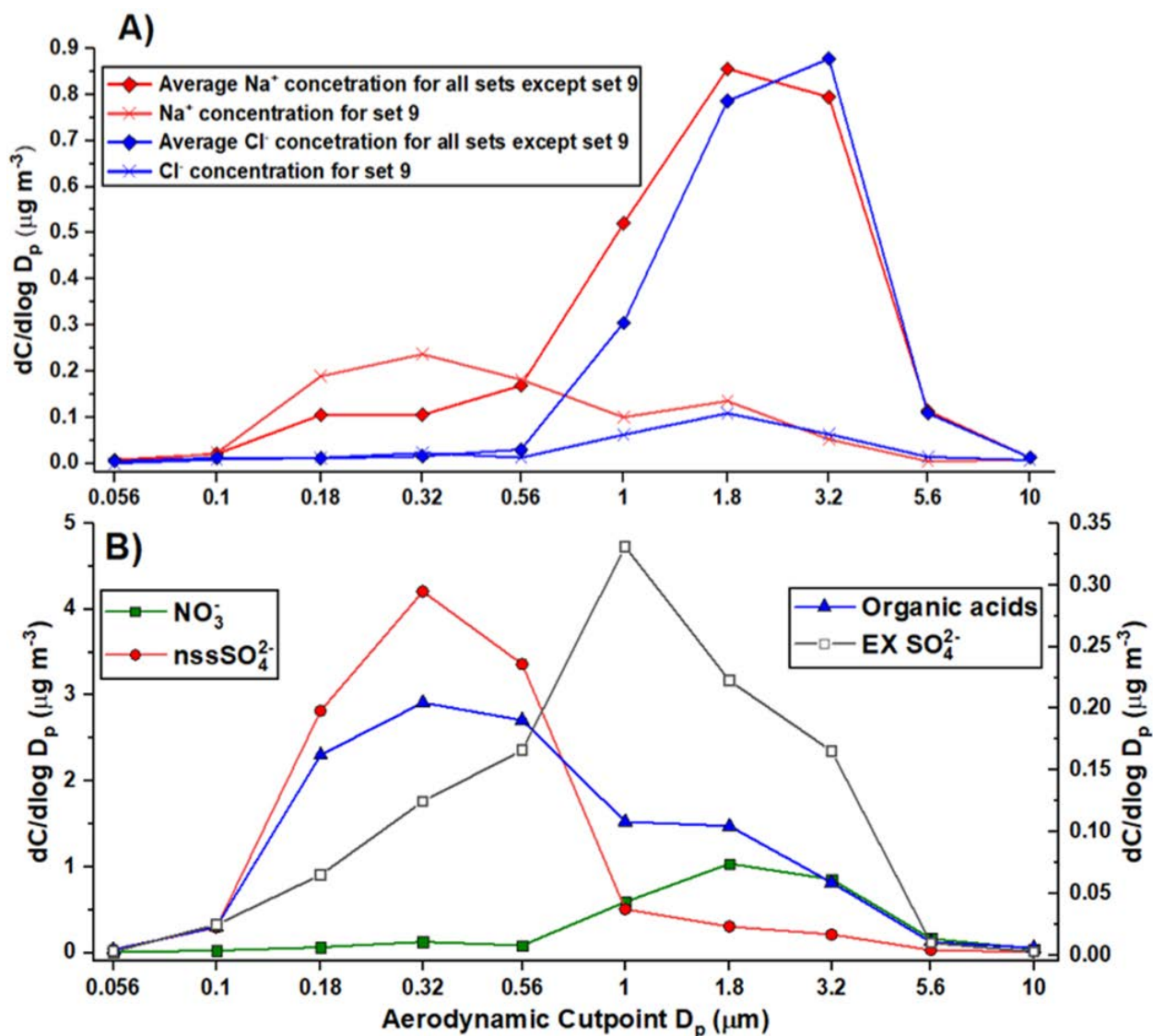


Figure 4 Mass size distributions of A) total Na^+ and Cl^- , and B) acids participating in Cl^- depletion reactions (nss and ex SO_4^{2-} , NO_3^- , organic acids) for all MOUDI sets except set 9. Set MO9 (presented with cross markers in panel A) exhibits peculiarly different behavior with a more pronounced peak in the submicrometer range for Na^+ .

The $\% \text{Cl}^-$ depletion was significant for the entire sampling period with values ranging between 21.3 - 90.7% and a mean value of 57.9% (Figure 2). Although not very large, there was a difference in mean $\% \text{Cl}^-$ depletion values between the wet season ($61.9 \pm 35.3\%$) and dry season ($47.1 \pm 37.4\%$). The higher mean depletion in the wet season can potentially be linked to the combination of a higher combined amount of the acids (NO_3^- ,

Ex SO_4^{2-} , organic acids) participating in Cl^- depletion (wet = $1.21 \pm 0.64 \mu\text{g m}^{-3}$, dry = $1.10 \pm 0.68 \mu\text{g m}^{-3}$) and lower ssNa^+ (wet = $0.46 \pm 0.39 \mu\text{g m}^{-3}$, dry = $0.56 \pm 0.13 \mu\text{g m}^{-3}$).

The mass size distribution of Na^+ was unique for set MO9 with a peak in the submicrometer size range (Figure 4). Characteristics of set MO9 included having one of the lowest sample-averaged wind speeds (0.7 m s^{-1}) and the single highest rain amount (44.8 mm). The combination of a low wind speed and especially high rain (and thus wet scavenging potential) is consistent with factors expected for low ambient sea salt concentrations.

Sea Salt Reactivity

An advantage of the longer duration of the bulk PM measurements as compared to the available MOUDI data was the ability to further examine Cl^- depletion effects between the wet and dry seasons using more data, and to also compare weekday (Mon-Fri) and weekend (Sat-Sun) periods (Table 2). The $\text{Cl}^-:\text{ssNa}^+$ mass ratio was lower for $\text{PM}_{2.5}$ as compared to $\text{PM}_{\text{coarse}}$, regardless of it being the wet (0.32 ± 0.48 vs 1.46 ± 0.46) versus dry (0.59 ± 0.60 vs 1.59 ± 0.43) season, or weekend (0.55 ± 0.54 vs 1.57 ± 0.42) versus weekday (0.43 ± 0.55 vs 1.48 ± 0.47). This is presumably due to the higher concentration of acids relative to Cl^- in $\text{PM}_{2.5}$ as compared to $\text{PM}_{\text{coarse}}$. While organic acid data were unavailable for the long-term bulk PM data, the mass size distributions from MOUDI measurements (Figure 4) reveal that organic acids are generally more enhanced for $\text{PM}_{2.5}$ (similar to SO_4^{2-}) as compared to $\text{PM}_{\text{coarse}}$. Nitrate was enhanced in $\text{PM}_{\text{coarse}}$ relative to $\text{PM}_{2.5}$, and thus NO_3^- was likely most actively involved with depletion in the coarser sea salt-containing particles.

Table 2 Comparison of $\text{Cl}^-:\text{ssNa}^+$ for wet and dry seasons and weekend (Saturday and Sunday) and weekdays (Monday-Friday). Data points with $\text{Ex SO}_4^{2-} < 0$ are excluded for the five columns on the right.

<i>Categories</i>		<i>Data</i>	$Cl^-:ssNa^+$	SO_4^{2-}	$nss\ SO_4^{2-}$	$Ex\ SO_4^{2-}$	NO_3^-
		<i>with Ex</i>		$(\mu g/m^3)$	$(\mu g/m^3)$	$(\mu g/m^3)$	$(\mu g/m^3)$
		$SO_4^{2-}>0$					
		(%)					
<i>PM_{2.5}</i>	Wet season	40	0.32±0.48	2.67±1.54	2.61±1.53	0.95±1.31	0.35±0.26
	Dry season	66	0.59±0.60	2.77±1.90	2.74±1.90	0.35±0.25	0.20±0.21
	Weekday	52	0.43±0.55	3.16±1.95	3.12±1.96	0.75±1.13	0.19±0.22
	Weekend	68	0.55±0.54	2.07±1.13	2.03±1.12	0.38±0.34	0.17±0.26
<i>PM_{coarse}</i>	Wet season	76	1.46±0.46	0.40±0.27	0.31±0.27	0.26±0.20	0.51±0.34
	Dry season	49	1.59±0.43	0.52±0.32	0.44±0.33	0.32±0.17	0.74±0.50
	Weekday	62	1.48±0.47	0.46±0.31	0.37±0.31	0.29±0.20	0.52±0.46
	Weekend	62	1.57±0.42	0.42±0.26	0.34±0.28	0.27±0.18	0.44±0.42

Enhanced Cl^- depletion in the wet season versus the dry season was likely driven by higher $Ex\ SO_4^{2-}$ and NO_3^- concentrations in the wet season, although as will be shown subsequently using MOUDI data, organic acids may also play a large role. The higher Cl^- depletion during weekdays can be explained by more anthropogenic activity yielding more acids in the ambient aerosol, which is more evident for $PM_{2.5}$ due to almost twice as much $Ex\ SO_4^{2-}$ compared to weekends. Future work is warranted to examine such temporal differences in Cl^- depletion effects with more organic acid data in conjunction with SO_4^{2-} and NO_3^- .

To expand on the Cl^- depletion results, the MOUDI sets were further categorized into five separate categories based on pollution characteristics. Using a combination of aerosol composition data, HYSPLIT back-trajectories, and data from the Navy Aerosol Analysis and Prediction System (NAAPS) (<https://www.nrlmry.navy.mil/aerosol/>) (Lynch et al., 2016), the categories were defined as follows along with their associated MOUDI

sets and total water-soluble mass concentrations ($\mu\text{g m}^{-3}$): “Clean” = MO11 (2.7); “Highest Rain” = MO9 (6.2); “Fire” = MO7/8 (13.25 ± 0.45); “Continental Pollution” = MO12/14 (15.05 ± 1.55); “Background” = MO1-2/4-6/10/15-21 (5.77 ± 1.3). “Clean” represents the MO set with the lowest total water-soluble mass. “Highest Rain” is for the set described already with the unusual mass size distribution of Na^+ that exhibits a more dominant peak in the submicrometer mode. “Fire” includes two sets impacted by transported biomass burning emissions from southwest of Manila close to Borneo and Sumatra, as evident from enhanced levels of the biomass burning marker K ($0.40 \pm 0.01 \mu\text{g m}^{-3}$ vs $0.17 \pm 0.05 \mu\text{g m}^{-3}$ for the other categories). “Continental Pollution” includes sets impacted by East Asia air masses that have the highest overall water-soluble mass concentrations of sets not impacted by biomass burning. Lastly, “Background” includes all other sets.

Figure 5 compares the overall composition of the MOUDI sets included in each category along with the mean $\% \text{Cl}^-$ depletion. The least (21.3%) and most depletion (90.7%) occurred in the “Clean” and “Highest Rain” categories, respectively. The “Continental Pollution” category exhibited the second highest Cl^- depletion (79.4%) owing to its elevated cumulative amount of acids (i.e., Ex SO_4^{2-} , NO_3^- , organic acids: $2.28 \mu\text{g m}^{-3}$). In contrast, the “Clean” category only had $0.68 \mu\text{g m}^{-3}$ of those same acids. Worth noting is that all categories except “Highest Rain” ($0.13 \mu\text{g m}^{-3}$) exhibited similar amounts of Ex SO_4^{2-} ($0.26\text{-}0.38 \mu\text{g m}^{-3}$), with the key difference driving the variability in $\% \text{Cl}^-$ depletion being the overall amount of NO_3^- (wider range of $0.24\text{-}1.57 \mu\text{g m}^{-3}$) that is concentrated in the supermicrometer sizes as compared to the other acids (Figure 4B). “Fire” sets exhibited higher Cl^- depletion compared to “Background” sets even though both categories had similar Ex SO_4^{2-} . For these five pollution categories, there was more enhanced Cl^- depletion in the submicrometer stages as compared to larger sizes (Figure 6) coincident with higher concentrations of nssSO_4^{2-} and organic acids (Figure 4B). More specifically, the ratios of $\% \text{Cl}^-$ depletion for submicrometer stages relative to supermicrometer stages were as follows: “Continental Pollution” = 1.58, “Fire” = 2.15,

“Background” = 3.26. “Highest Rain” and “Clean” have no ratios owing to zero ssNa^+ and zero $\% \text{Cl}^-$ depletion in the supermicrometer range, respectively.

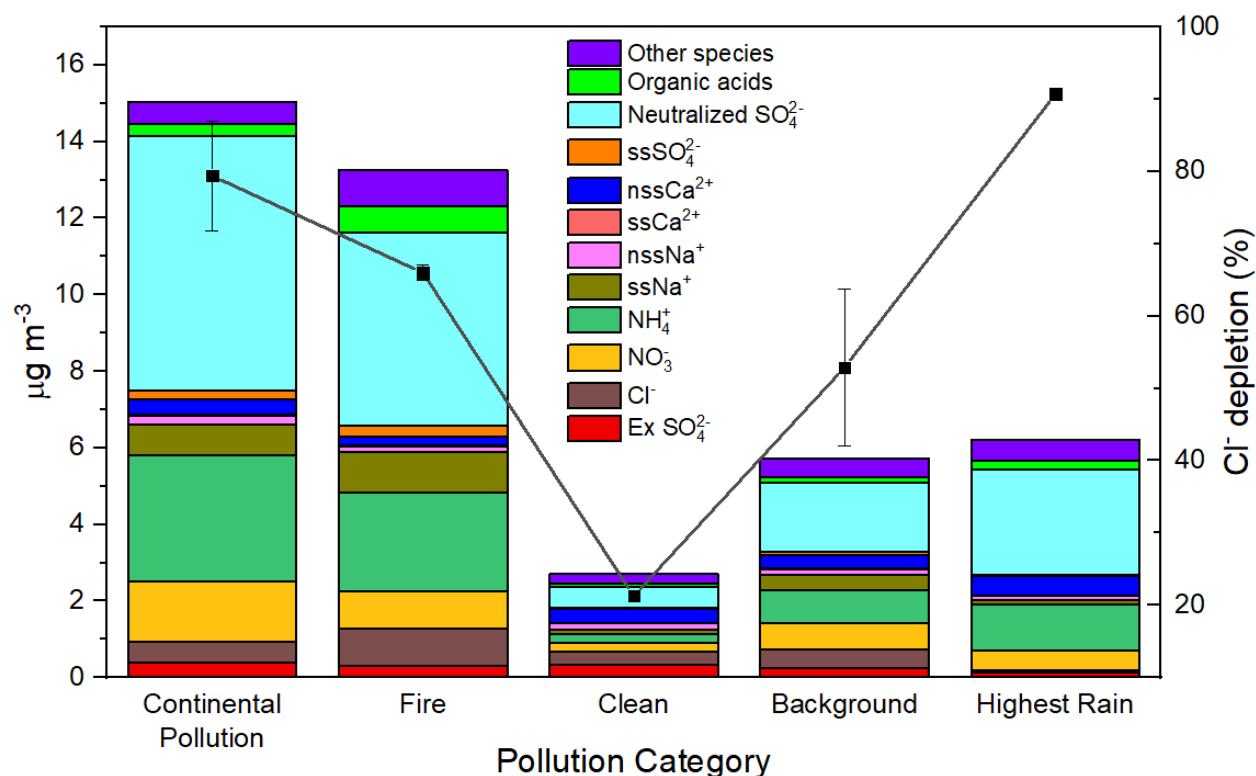


Figure 5 Water-soluble mass concentrations associated with different species categorized based on the five types of pollution characteristics. On the right y-axis is the $\% \text{Cl}^-$ depletion for each category. The ‘organic acids’ category includes carboxylic acids (Pyruvate, Adipate, Succinate, Maleate, Oxalate, Phthalate) and MSA. ‘Other species’ includes all the elements analyzed using IC and ICP-QQQ (listed in Section 2.2) that are not shown in this figure.

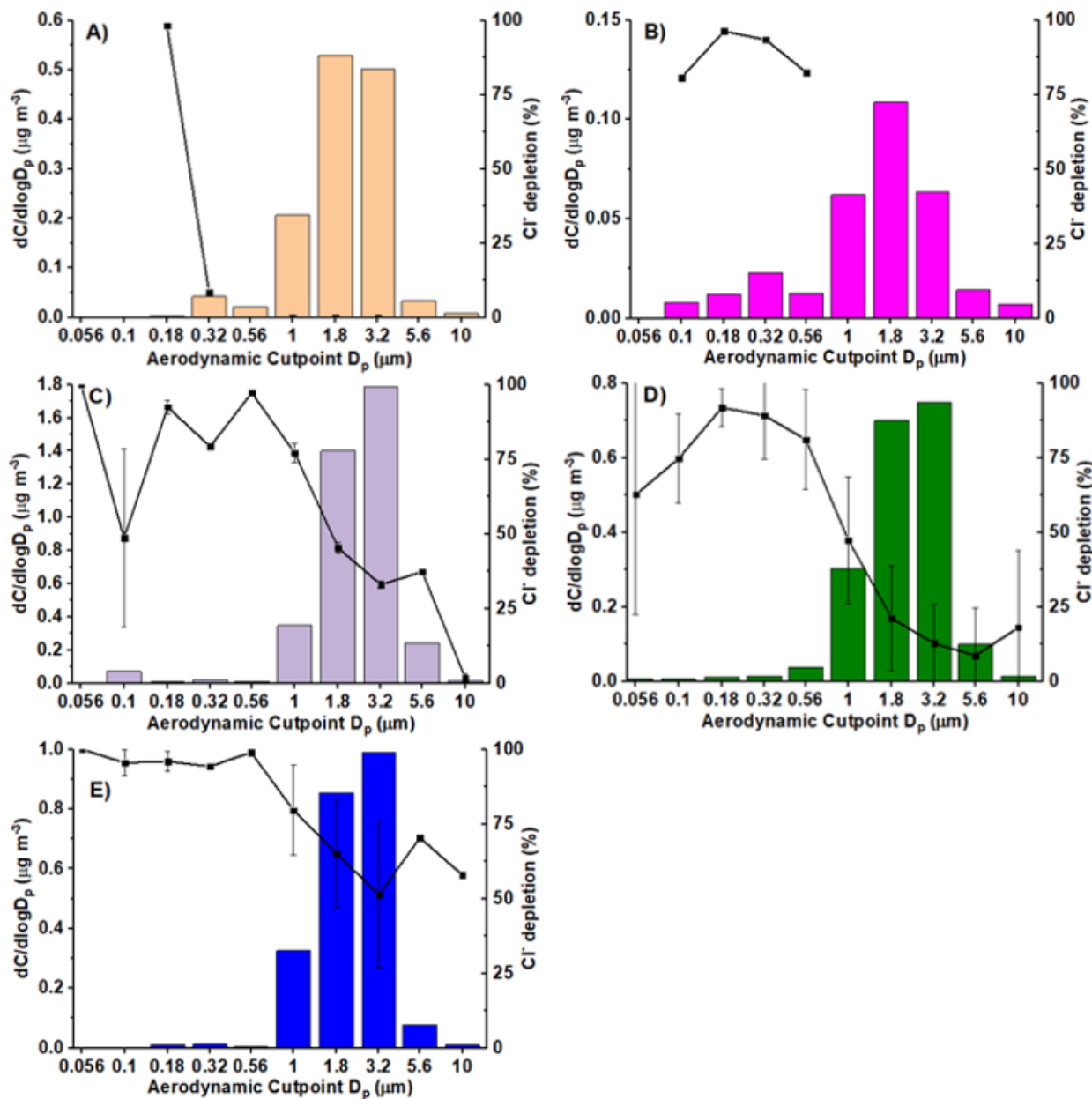


Figure 6 Average mass size distributions for Cl^- and the % Cl^- depletion for the five different pollutant categories: A) Clean, B) Highest Rain, C) Fire, D) Background and E) Continental Pollution. The bars correspond to left y-axis and lines with markers refer to the right y-axis.

For context in relation to a nearby region, Song et al. (2018) examined Cl^- depletion using shipboard total suspended particle (TSP) measurements over the western South China Sea and observed depletion levels of $73 \pm 23\%$ and further showed that Ex SO_4^{2-} and oxalate accounted for the majority of depletion in samples impacted by biomass burning. In contrast, (Hsu et al., 2007) observed mean Cl^- depletion levels of 90% for $\text{PM}_{2.5}$ and reduced levels for $\text{PM}_{\text{coarse}}$ (30%) over the northern South China Sea. These and numerous other studies have demonstrated that Cl^- depletion is a prevalent phenomenon in marine regions caused by a variety of acids such as SO_4^{2-} , NO_3^- , and organic acids.

Table 3 shows the theoretical maximum of Cl^- depletion attributable to inorganic and organic acids (i.e., Equation 9) for sub- and supermicrometer particles. Organic acids show potential to be important agents in Cl^- depletion for the submicrometer range, especially when accounting for the neutralization of SO_4^{2-} by NH_4^+ . NO_3^- could account for the most depletion in the supermicrometer range (up to 86.4%) as expected based on its mass size distribution exhibiting a peak coincident with major sea salt constituents. It also could have a non-negligible impact in the submicrometer range, potentially accounting for 17.6% - 54.8% of the Cl^- depletion observed.

Inorganic acids are more commonly linked to Cl^- depletion, but it is important to also consider organic acids. Sulfate and NO_3^- are stronger acids than organic acids and would be favored for depletion reactions as they deprotonate more readily; however, as they cannot always add up to 100% Cl^- depletion, organic acids can participate in such reactions. Oxalate displayed the highest theoretical contribution to Cl^- depletion among the organic acids measured, consistent with it being the most abundant organic acid. Organic acids (especially the longer-chain organic acids of adipate, succinate, and phthalate) reached high theoretical maximum contributions to Cl^- depletion for the “Fire” category. The effect of organic acids is not just limited to the submicrometer range but can also be seen in the supermicrometer range as evidenced by the “Background” category where organic acids could account for up to 40.4% of the observed supermicrometer Cl^- depletion. Regardless of the pollution category, the organic acids can be influential for Cl^-

depletion as has been demonstrated recently in other regions such as coastal California (Braun et al., 2017) and the South China Sea (Song et al., 2018).

Table 3 The percent contribution attributable to different species to Cl⁻ depletion for different sample set categories based on pollution characteristics.

<i>Acids</i>		Clean	Highest Rain	Background	Fire	Continental Pollution
<i>MSA</i>	≥ 1 μm	0	*	0.2	0	0
	< 1 μm	15	2.1	2.3	7.2	2.5
<i>Pyruvate</i>	≥ 1 μm	0	*	0	0	10.3
	< 1 μm	0	0	0	0.1	0
<i>Adipate</i>	≥ 1 μm	0	*	3.5	0.6	0
	< 1 μm	0	0	1.3	18.4	0
<i>Succinate</i>	≥ 1 μm	0	*	0.4	0.5	0
	< 1 μm	0	1.7	2.2	36.4	1.2
<i>Maleate</i>	≥ 1 μm	0	*	0	0	0
	< 1 μm	50.9	14.4	4.8	7.4	0.6
<i>Oxalate</i>	≥ 1 μm	0	*	35.4	25.6	18.0
	< 1 μm	65.6	62.2	52	74.6	67.9
<i>Phthalate</i>	≥ 1 μm	0	*	1.0	0.1	0.2
	< 1 μm	5.4	0.5	1.7	23.2	3.6
<i>All Organics</i>	≥ 1 μm	0	*	40.4	27.0	28.5
	< 1 μm	100	78.8	61.9	100	73.4

<i>nss</i> SO ₄ ²⁻	≥ 1 μm	0	*	64.0	38.6	52.9
	< 1 μm	100	100	98.3	85.2	100
<i>Ex</i> SO ₄ ²⁻	≥ 1 μm	0	*	42.3	19.4	23.8
	< 1 μm	100	0	22.6	0	11.1
NO ₃ ⁻	≥ 1 μm	0	*	86.4	71.0	84.0
	< 1 μm	54.8	38.9	36.4	17.6	18.8

* ssNa⁺ concentrations were 0 for the “Highest Rain” category for stages with cutpoint $D_p > 1 \mu\text{m}$.

Sea Salt Enrichment Factor Analysis

As a way to quantify the degree of contamination of sea salt particles, enrichment factors (EF) were quantified for a host of species (Table 4). Analysis of sea salt EF values were conducted using concentrations from MOUDI samples for the three stages with the peak in sea salt mass (1-5.6 μm). EF values > 10 often signify species that have a non-sea salt contribution such as from anthropogenic sources, whereas values ≤ 10 have a significant contribution from sea water (Zhang et al., 2015). As expected, key constituents of sea salt exhibited values below 10 (e.g., Cl⁻, Mg²⁺, K). The various forms of SO₄²⁻ (NSS, Ex, total) exhibited values below 10 with a possible explanation that the source in the three supermicrometer stages of interest could be of marine origin (i.e., dimethylsulfide). Most of the remaining species in Table 4 exhibited very high EF levels (Fe, Al, Ba, Mn, Pb, NO₃⁻, V, Zn, NH₄⁺). Some of these species are linked to crustal emissions such as dust (Fe, Al, Mn) (Dadashazar et al., 2019; Ma et al., 2019), whereas others (e.g., Pb, V, Zn) are more linked to urban emissions such as combustion, shipping, water processing, and smelting (Nriagu, 1989; Prabhakar et al., 2014). These results indicate that sea salt-containing particles exhibit high levels of contamination in the study region owing to mixing between marine air and other air masses.

Table 4 Sea salt enrichment factor (ssEF) values calculated using Equation 10. ssNa^+ is used as the reference species in the sample and the control. The concentrations used in this analysis represent the sum from the three MOUDI stages (cutpoint $D_p = 1, 1.8, 3.2 \mu\text{m}$) with the highest sea salt concentrations. MO9 is not shown in the table since the ssNa^+ concentrations for all the cutpoints above $1 \mu\text{m}$ is zero.

	Cl ⁻	Fe	Ex SO ₄ ²⁻	Mg ²⁺	nss SO ₄ ²⁻	SO ₄ ²⁻	K	Ca ²⁺	Al	Ba	Mn	Pb	NO ₃ ⁻	V	Zn	NH ₄ ⁺
MO1	0.5	1256	1.5	1.8	2.0	3.1	4.0	8.6	149	1870	4704	9696	18249	27282	44817	92387
MO2	0.7	47	1.5	1.6	1.6	2.9	3.0	13.7	60	2015	3695	3037	26392	41077	29938	29192
MO4	0.6	881	3.5	1.9	4.1	5.4	3.6	16.3	110	3036	6749	3522	27375	40266	81330	119091
MO5	0.4	72	1.3	1.5	2.1	3.2	3.0	5.1	62	1097	3083	916	24064	15998	8570	154792
MO6	1.4	4924	6.9	4.1	8.0	10.8	13.9	85.8	577	4606	15008	8342	85856	61301	122003	239708
MO7	0.6	1342	1.0	1.5	1.6	2.7	1.7	5.6	127	473	1679	1903	14389	3573	4719	111865
MO8	0.5	1933	1.6	1.7	2.3	3.5	2.0	8.6	177	549	2329	1532	16331	4501	6670	140779
MO10	1.6	13139	24.6	8.9	37.2	42.7	26.7	230.7	1150	22795	43859	132581	237420	365657	926482	2584382
MO11	2.3	10605	5.9	5.0	6.6	9.7	8.8	98.4	1225	5134	22851	5686	42635	70841	56864	162590
MO12	0.6	985	1.3	1.6	1.7	2.9	1.2	9.8	83	860	2632	3601	24672	12169	25384	73718
MO14	0.2	2038	3.2	2.0	5.0	6.6	2.7	26.2	188	1832	5303	7768	56248	28575	39404	384972
MO15	3.1	102033	54.2	22.4	120	121	197.1	836.7	5380	87457	367320	655929	1052907	1700556	7435679	9543761

<i>MO16</i>	0.7	7987	4.4	3.0	5.5	6.6	5.2	50.3	441	6770	16160	17758	51725	34529	116536	235036
<i>MO17</i>	0.9	1932	0.5	1.7	1.4	2.4	2.4	17.4	117	2027	4588	4312	15234	13417	49356	179753
<i>MO18</i>	0.8	1663	0.5	1.5	1.3	2.3	2.0	14.1	113	2352	4319	7712	19011	17995	59924	165428
<i>MO19</i>	0.8	2480	1.5	1.8	1.9	3.0	3.0	22.8	202	1828	4724	3515	18361	9842	9596	191928
<i>MO20</i>	0.8	2013	0.8	1.7	1.8	2.8	1.9	19.8	122	2063	6931	2357	24117	18335	35272	397800
<i>MO21</i>	0.9	824	0.2	1.3	0.5	1.4	1.2	7.8	44	703	1541	611	9463	2853	8560	170280

Hygroscopicity Analysis

The objective of the hygroscopicity analysis is to determine how κ varies across different stages in relationship with composition, especially with a focus on the relative amount of sea salt. Petters and Kreidenweis (2007) give a κ range of 0.1-0.9 for atmospheric aerosol. Values of 0.1 to 0.5 are common for a variety of air mass types (marine, urban, biogenic, biomass burning, remote, free tropospheric) in other regions (Chang et al., 2010; Dusek et al., 2010; Hersey et al., 2013; Sarangi et al., 2019; Shingler et al., 2016; Shinozuka et al., 2009).

For this study, κ ranged from 0.02 to 0.31 among all the stages from individual sets. The low κ values are not surprising given the polluted nature of Manila with high levels of organics and BC, as shown by the size-resolved profile of volume fractions of different aerosol constituents in Figure 7A. More specifically, organics and BC cumulatively accounted for 61% - 99% of the mass concentration across the 11 MOUDI stages when averaged across all MOUDI sets. Figure 7B shows the size-resolved profile of κ based on the cumulative average of all MOUDI sets, where a bimodal profile is evident with peaks in κ at cutpoint diameters of 0.32 μm (0.27) and 3.2 μm (0.30). Expectedly, those two MOUDI stages coincided with the lowest cumulative volume fractions of organics and BC. The 0.32-0.56 μm stage was coincident with the highest volume fraction (0.37) of components categorized as being “high κ Inorganics”: $(\text{NH}_4)_2\text{SO}_4$, K_2SO_4 , $\text{Mg}(\text{NO}_3)_2$, NaNO_3 , Na_2SO_4 , CaCl_2 , MgCl_2 , and $\text{Ca}(\text{NO}_3)_2$. Conversely, the 3.2-5.6 μm stage exhibited the highest volume fraction for sea salt (0.11). Sea salt was also very influential in driving up the value of κ to 0.26 for the 1.8-3.2 μm stage. An important point of this analysis is that the reported values of κ were still much lower than that of pure sea salt (1.24), indicative of the overwhelming influence of other pollution sources mixing with sea salt, especially organics and BC, which were most influential of all aerosol constituents owing to their low assigned κ values and dominant volume fractions across all MOUDI stages. When the analysis in Figure 7B was repeated for each of

the five pollution categories defined in Section 3.3, there was hardly any difference in κ values at fixed sizes (Figure S2), which again speaks to the dominant contribution from organics and BC to κ .

Future work is warranted to take on a more rigorous approach to calculating κ for the organics in this study region as they represent a dominant fraction of the PM across the spectrum of sizes examined here (Figure 7A). For this study, all organics (excluding organic acids) were assigned a κ value of 0.1 as a representative value based on past reports (Dusek et al., 2010; Hersey et al., 2013; Pöschl et al., 2019), but the actual κ values for organics can vary from 0.06 to 0.26 depending on the oxygen to carbon ratio as noted in recent work for a variety of air mass types (Li et al., 2019; Shingler et al., 2016).

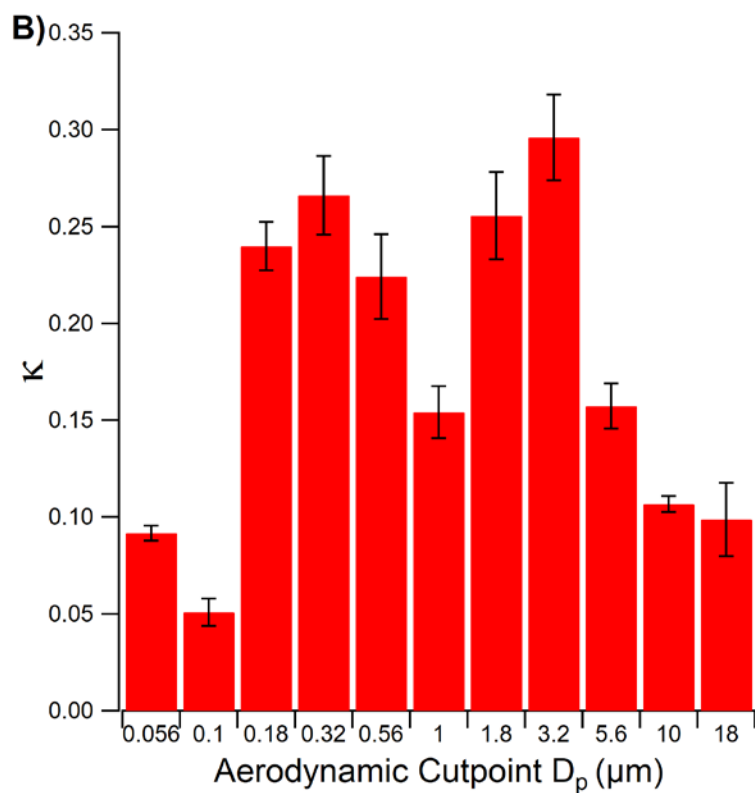
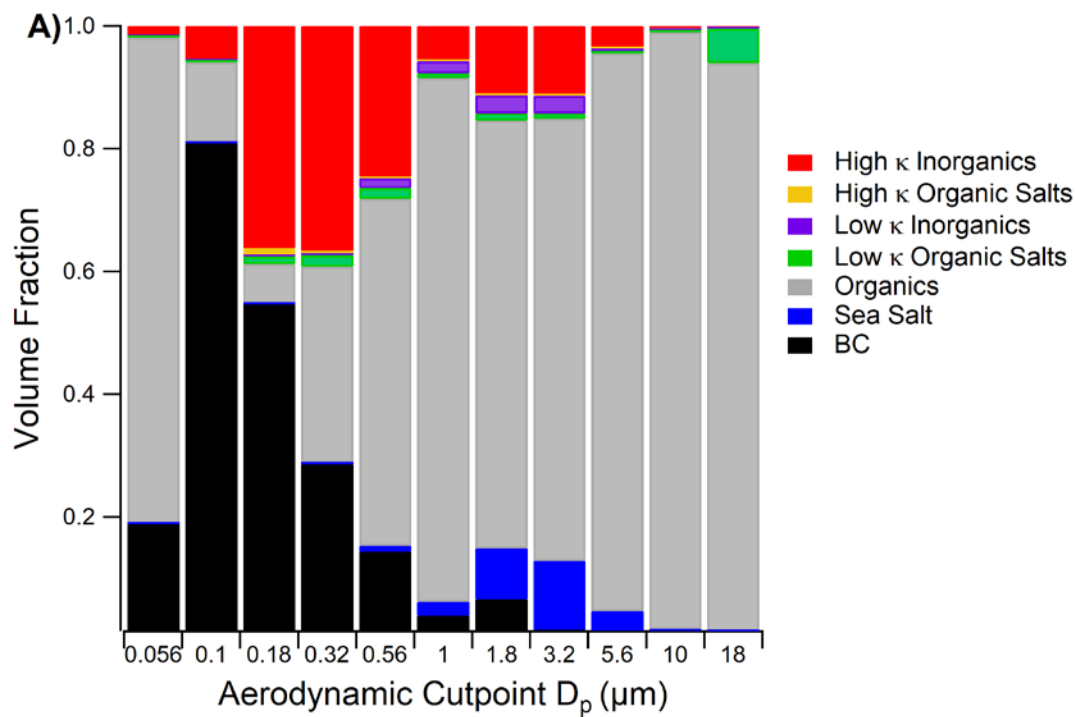


Figure 7 A) Volume fraction of different aerosol constituents for each MOUDI stage based on the cumulative average of all sets in Table 1. B) Corresponding κ

values for each stage as an average of all MOUDI sets. The categories in panel A refer to species defined in Table S2: “Low κ Organic Acids” include CaOxalate, MgOxalate, and ZnOxalate; “High κ Organic Acids” include Na₂Oxalate; “Low κ Inorganics” include Ca₂SO₄ and MgSO₄; “High κ Inorganics” include (NH₄)₂SO₄, K₂SO₄, Mg(NO₃)₂, NaNO₃, Na₂SO₄, CaCl₂, MgCl₂, and Ca(NO₃)₂; and “Organics” include all organics not contained in the two organic acid categories.

Particle Morphology

Previous investigations of sea salt aerosol morphology have shown that the sea salt particles typically are cubic in nature but with certain attributes such as having “halos” of other species in the case of aged sea salt (Hoffman et al., 2004; Laskin et al., 2002; Laskin et al., 2012). Based on EDX evidence of Na^+ and Cl^- enrichment, representative particles containing these elements are shown for three supermicrometer MOUDI stages with aerodynamic cutpoint diameters ranging from 1.8 to 10 μm (Figure 8). The particles shown in the six images all exhibit non-spherical morphology with $\text{Cl}^-:\text{Na}^+$ mass ratios varying from 1.18 to 1.94 with an average of 1.64. The particles in the 1.8 – 3.2 μm stage have a cubical shape but with rounded edges. The particles in the larger stages exhibited more complex morphologies with rounded edges and evidence of holes and other species attached to the outer peripheries. These Na^+ - and Cl^- -containing particles all reveal evidence of mixing with other pollutant types and undergoing chemical processing, which is confirmed by Fe, Mo, and Co being present in the various particles based on EDX analysis. The presence of these elements are shown in Figure S3. The latter three elements have anthropogenic sources in the study region (Cruz et al., 2019). Interestingly for the particles shown in Figure 8B/D/E, O was enriched in areas where Cl^- was not, and vice versa, while Na^+ covered the entire particles. This is in accordance with previous study that discussed the morphology of fresh and aged sea salt in contact with acidic gases (Chi et al., 2015).

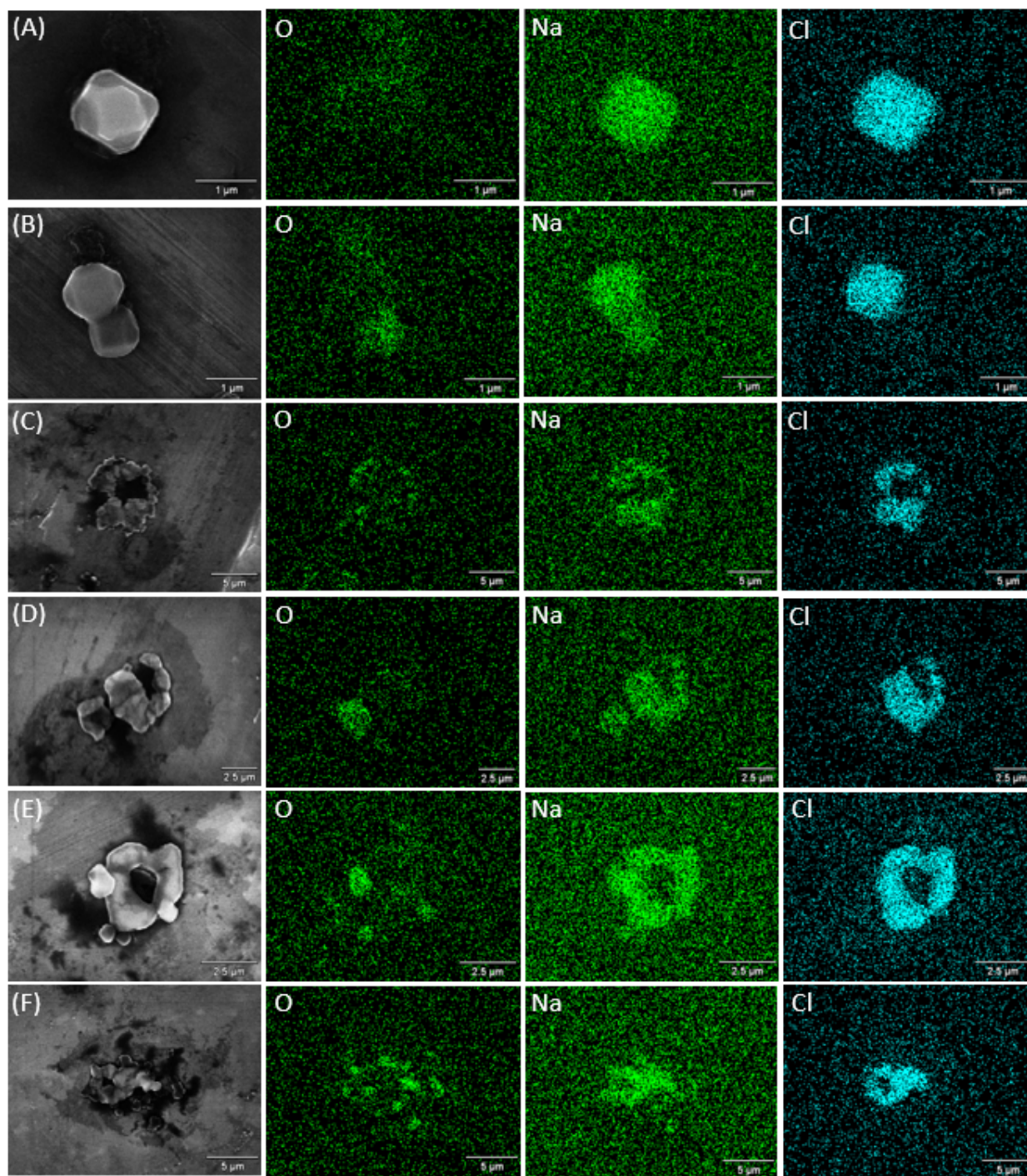


Figure 8 Size-resolved SEM-EDX characterization of representative particles containing Na and Cl collected at MO on 1 August 2018. The panels correspond to MOUDI stages with the following D_p ranges: (A/B) 1.8-3.2 μm ; (C/D) 3.2 – 5.6

μm ; (E/F) 5.6-10 μm . Also shown for each substrate sample are O, Na and Cl distributions in the individual particles based on EDX analysis.

Conclusions

This study reported on different aerosol datasets in Metro Manila with a focus on sea salt characteristics and their dependence on meteorology and mixing with non-marine air masses. Although sea salt is not the most abundant aerosol type measured in Metro Manila, the results of this study have broad relevance to other marine regions and especially coastal cities owing to the insights this study provides for relationships between precipitation and sea salt, impacts of other air masses mixing with marine aerosols, size-resolved characteristics of aerosol, and chemical reactivity of sea salt as a function of size and different temporal scales. The main results of this work are as follows:

- Sea salt variability, especially the large changes during the wet season, is driven largely by precipitation owing to wet scavenging. The analysis revealed a stronger anti-relationship between sea salt and precipitation accumulation when the latter value was integrated over a larger area encompassing the study site as compared to just from the study site.
- There was significant sea salt chemical reactivity in the study region owing to inorganic and organic acids stemming from a wide variety of sources. Chloride depletion was more pronounced in the wet season as compared to dry periods and during weekdays relative to weekend days.
- Enrichment factor analysis showed that sea salt aerosols were highly contaminated with crustal and anthropogenic pollutants (Fe, Al, Ba, Mn, Pb, NO_3^- , V, Zn, NH_4^+). Morphological results revealed complex non-spherical shapes for sea salt-containing particles owing to mixing of sea salt with other pollutants.

- Values of the hygroscopicity parameter, κ , ranged from 0.02 to 0.31 with a bimodal profile across all MOUDI stages. Low values coincided with higher enrichment of BC and water-insoluble organic species in contrast with the highest values being in the stages most enriched with either high- κ inorganic species (0.32-0.56 μm) or sea salt (3.2-5.6 μm). Values are considerably lower than pure sea salt owing to the overwhelming influence of other air masses mixing with sea salt.

CHAPTER 2: PRETREATMENT OF SECONDARY EFFLUENT FOR WATER REUSE

Abstract

The effectiveness of three different pretreatment processes (Fluidized bed crystallization reactor, Ultrafiltration and ferric chloride coagulation and flocculation) in order to remove scale-forming and fouling substances from the wastewater secondary effluent were studied. At optimized conditions, fluidized bed crystallization reactor (FBCR) was able to remove >99.9% of magnesium, 97% of calcium and 42% of silica while ultrafiltration (UF) and ferric chloride coagulation were only able to remove 18% and 16% of the silica concentration, respectively. UF was also able to reduce the turbidity of the SE by 93%. Furthermore, the co-precipitation of different mineral salts with organic matter were also discussed using size exclusion chromatography-organic carbon detector (SEC-OCD). At optimized conditions, ferric chloride resulted in the highest natural organic matter (NOM) reduction (56%) compared to FBCR (26%) and UF (13%). Excitation emission matrix-parallel factor (EEM-PARAFAC) analysis were used to characterize the NOM in the SE and the effluent of these pretreatments. Five different components (three humic substance, one fulvic acid and one protein-like) were detected. FBCR (7-100%) and ferric chloride (26-65%) were able to remove from all 5 types of NOM while UF was only able to reduce the concentration of the protein-like NOM (11%).

Introduction

Potable water scarcity has become an important issue over the last few decades due to rainfall patterns' changes and increasing population. Recent estimations demonstrate that over one billion people do not have access to clean potable water, and approximately 2.3 billion people live in regions with water shortages (Service, 2006). Thus, water reuse and recycling are becoming increasingly necessary to augment potable water supplies (Gerrity et al., 2013).

High pressure membrane processes, such as nanofiltration (NF) and reverse osmosis (RO), are commonly used to produce drinking water from brackish waters. RO and NF processes are able to remove both organic and inorganic contaminants and produce clean water (Rahardianto et al., 2007). These processes have the potential to treat brackish water to potable water, thereby increasing drinking water supplies. However, there are two major limitations to use these processes: membrane fouling and production of a concentrated brine stream.

Membrane fouling and brine generation problems are closely linked in that membrane fouling limits the fraction of the feed water that can be recovered as permeate. Feed waters with low concentrations of potential foulants allow greater permeate recovery, thereby producing smaller volumes of waste brine solutions. Thus, the degree of pretreatment prior to RO or NF controls the amount of membrane fouling and the volume of waste brine solutions that are produced.

The causes of membrane fouling include: 1) microorganisms that grow on the membrane; 2) colloidal material that adsorbs on the membrane; 3) the formation of mineral scale, most commonly divalent cations combined with carbonate and sulfate; and 4) natural organic matter, such as humic and fulvic acids, that adsorb on the membrane. The goal of pretreatment processes is to obtain the highest level of foulant removal that is technically and economically feasible. There is a wide variety of pretreatments that remove scaling and/or fouling precursors which can improve

the permeate water recovery rate in NF or RO. Fluidized bed crystallization reactor (FBCR) and softening are two of main processes that mainly target inorganic salts that may cause scaling on the membrane surface (Aghdam et al., 2016; Graveland et al., 1983; Vanderveen and Graveland, 1988). Coagulation and flocculation process using ferric chloride, Polyaluminum chloride or aluminum chlorohydrate is another pretreatment that targets and removes organic foulants (Ho et al., 2015; Racar et al., 2017). Microfiltration (MF) and Ultrafiltration (UF) are another common pretreatments for high-pressure membrane processes. Depending on its pore sizes, UF is able to achieve several logs removal of pathogens and viruses (Voutchkov, 2017).

FBCR is often a cylindrical column that is filled with some sort of particles such as sand or garnet and the water that needs to be treated enters the column at the bottom. An alkaline chemical is also added from the bottom or injected from the side of this column to increase the pH of the solution promoting a heterogeneous precipitation on the sand or garnet inside the column. On the other hand, softening process takes place in a basin filled with the water that needs to be treated which is continuously mixed with addition of an alkaline chemical. The main method of removing the minerals with this process is through homogeneous precipitation. FBCR has numerous advantages over softening. For non-zero order reactions, a plug-flow reactor obtains a higher conversion per unit volume compared to a continuously stirred-tank reactor (Graveland et al., 1983). Maximum pH values set for softening are limited by Mg precipitation due to bad precipitation characteristics of $Mg(OH)_2$. Therefore, no to low magnesium removal in softening process may cause scaling in the downstream high-pressure membrane processes. While a positive saturation index (SI) indicates precipitation possibility, a certain activation energy is needed to form a nucleus (Graveland et al., 1983). This energy is much lower for FBCR due to presence of precipitation surface and the SI required for commencement of precipitation is lower compared to softening. This means that for similar calcium

and magnesium removal, lower alkaline chemical is needed for FBCR compared to softening. Furthermore, the residence time in FBCR is less than 30 seconds while the mixing time in the softening process can take up to 120 min (Rahardianto et al., 2010). Softening produces relatively small crystals due to formation of many homogeneous nuclei. This makes the solid-liquid separation process difficult since the produced sludge has a considerable amount of adhering solution with high impurities (Sluys et al., 1996). On the other hand, a cylindrical FBCR column results in a particle classification along the length of the fluidized bed and the bigger particles move down due to gravity and can be removed and replaced with fresh particles. The operation and maintenance costs of a FBCR is also significantly lower than other precipitation processes thanks to its reliability and the form of calcium carbonate that is produced (Graveland et al., 1983).

Microfiltration and ultrafiltration are becoming the main pretreatment for RO. Compared to conventional treatments, MF/UF is more robust option and provides cleaner feed for RO (Pearce, 2008). Furthermore, using MF/UF as the pretreatment for RO lowers the overall cost of energy consumption. According to Pearce (2008), the energy cost for MF and RO treatment is 0.5 kWh/m³ while the energy cost for conventional and RO treatment is 1.3 kWh/m³. This higher cost is due to the higher power and cleaning cost for RO when conventional pretreatment is being used. MF and UF are capable of removing turbidity, non-soluble and colloidal organic contaminants in the feed water. Turbidity and SDI₁₅ can be lowered to less than 3 and 0.1 in MF/UF systems (Ishida and Cooper, 2015; Pearce, 2008). There are several parameters that affect the cost of MF/UF system: feed water quality, permeate flowrate and recovery rate. Feed water quality determines the backwash and air scouring frequency while flowrate and recovery rate affect the pumping cost. In other words, membrane fouling is the main parameter for filtration cost. Membrane fouling will increase the backwash and air scouring frequency as well as the pressure required to produce the same permeate flowrate. In MF systems, 80%

of the fouling is due to the blocking of membrane matrix by nanoparticles (Ishida and Cooper, 2015). This phenomenon is responsible for the irreversible fouling of the membrane thereby increasing the cost of treated water. However, UF membrane pores are an order of magnitude smaller therefore, UF pretreatment systems does not face such a problem (Voutchkov, 2010).

Coagulation and flocculation is a cost-effective conventional treatment that can be used prior to high-pressure membrane filtration processes. Coagulation is able to effectively remove acidic and hydrophobic organics, macromolecules, colloidal particles and suspended solids (Racar et al., 2017). As conventional coagulants, ferric or aluminum salts, destabilize the organics and colloidal particles into aggregates removed as sludge at the bottom of settling tank or filtered by sand filtration or microfiltration. The most important parameters for an optimized coagulation process are: type of the coagulant, dose and resulting pH values. Natural organic matter (NOM) is mainly consisted of anionic or nonionic macromolecules and polymers; therefore, cationic coagulants are preferred (Racar et al., 2017). According to Ho et al. (2015), ferric chloride is able to reduce TOC concentration twice as much as Polyaluminum chloride (PACl) and aluminum chlorohydrate (ACH). This is probably due to the fact that PACl and ACH are already polymerized coagulants while ferric chloride hydrolyzes and polymerizes within the solution thereby offering more sites and surface for co-precipitation of organic matter with ferric hydroxide precipitation. Iron salts are able to coagulate at wider pH ranges, result in heavier flocs and pose less health risk in case of an overdose (Aghdam et al., 2016; Ho et al., 2015; Racar et al., 2017). The optimal dose of coagulant depends on the water characteristics, nature of the suspended solids, resulting pH and the water quality that needs to be achieved. Three types of hydrolyzed products of ferric chloride are: monomeric iron molecules (as well as a dimer and a trimer), medium polymeric iron and polymeric or colloidal iron (Dong et al., 2015; Racar et al., 2017). The production and presence of these species results in different organic matter

removal mechanism and efficiency; thus it should be reinvestigated for a specific wastewater (Racar et al., 2017).

In this study, 3 different pretreatment processes (FBCR, UF and FeCl_3 coagulation) are optimized and their applicability based on their removal efficiencies of organic and inorganic foulants are investigated. While there are numerous studies on using softening as a pre or intermediate treatment for a high-pressure membrane filtration processes, there are very limited studies, if any, on treating secondary effluent using FBCR. A pilot scale FBCR is set at 4 different pH values (10.5, 11, 11.5 and 12) in order to investigate the removal efficiencies of variety of scaling and fouling contaminants. A full scale UF system is used for investigating the removal of fouling and scaling contaminants. Based on previous studies, FeCl_3 coagulant is being used and different parameters (coagulant dose, resulting pH and flocculation time) are optimized in order to achieve the highest removal of organic and inorganic foulants. A variety of instrumentation such as size exclusion chromatography-organic carbon detector (SEC-OCD) is being used to investigate the co-precipitation of inorganic and organic contaminants. Furthermore, excitation emission matrix (EEM) and EEM-Parallel factor analysis (PARAFAC) is being used to characterize the NOM and compare the ability of these pretreatment techniques in removing different types of NOM.

Materials and Method

Secondary Effluent

Secondary effluent was delivered through a pipeline from Agua Nueva water reclamation facility to the Water and Energy Sustainable Technology (WEST) center besides it in Tucson, Arizona. Details of its water quality are shown in Table 5.

Table 5 Secondary effluent water quality

<i>Parameters</i>	<i>Concentration (mg/L)</i>
pH	7.2-7.5
Turbidity (NTU)	0.8-1.2
Alkalinity (as CaCO₃)	153-203
Sodium	143-149
Magnesium	15-18
Potassium	16-18
Calcium	87-97
Barium	0.1-0.3
Chloride	134-140
Bromide	0.3-0.5
Sulfate	177-182

Materials

Powdered sodium hydroxide, 37% hydrochloric acid and 40% ferric chloride solution were procured from Hill brothers chemical company in Tucson, Arizona. Garnet sand (#60) for the FBCR were procured from Red Flint Sand & Gravel, LLC.

Equipment

The FBCR reactor consisted of a 280 cm tall and 15.24 cm diameter clear PVC pipe that contains 150 cm long bed for the garnet sand. The secondary effluent was fed from the bottom of the column and the 0.1 M sodium hydroxide solution were injected from 4 equally-distanced injection ports within the bottom half of the bed perpendicular to the column. Secondary effluent flowrate was set to 0.4 gal/min resulting in a 20-25% bed expansion. Secondary effluents exiting the FBCR were passed through a Aquaboon 5 micron 20 inch polypropylene filter contained in standard filter housing.

A full-scale UF system was procured from Applied Membranes. This system is currently being used as a pretreatment for a full-scale RO system in the WEST center. This system uses a DOW IntegraFlux UXA-2680XP module and has not been replaced in the past 18 month of use.

Ferric chloride coagulation and flocculation Experiments were conducted using a jar test apparatus (PB-900 Programmable Jar tester, Phipps & Bird) containing 6 reaction vessels. The dimensions of the vessels were 11.5 cm × 11.5 cm × 21 cm, and each test was conducted on 1 liter of solution. Solutions were mixed at 250 rpm for 3 min immediately after dosing with ferric chloride and then the mixing rate were reduced to 50 rpm for the flocculation period. Precipitates in the solutions were let to settle for 30 minutes prior to sampling from the supernatant.

Analytical Methods

Anions were analyzed using a Metrohm Professional IC (Model 850 Anion HP Gradient). A Metrohm ASUPP7-250 (4 mm ID × 250 mm) column was used for this

purpose. All reagents and standards were prepared in ultrapure water (18M Ω cm). The eluent solution for anions was 3.2 mM of sodium carbonate and 1.2 mM of sodium hydrogen carbonate and the Metrohm Suppression Module (MSM) solutions were 100 mM sulfuric acid for regeneration and ultrapure water for rinsing.

Cations were analyzed using an Agilent 8800 ICP-QQQ. All of the reagents and tuning solutions were procured from Agilent. Samples were acidified using 2% nitric acid before analysis. Alkalinity was measured using Gran Function Plot Method available in U.S. Geological Survey (USGS) online free software.

Apparent molecular weight (AMW) of dissolved organic matter (DOM) was measured using size exclusion chromatography (SEC). HPLC (Agilent 1290) hyphenated with an organic carbon detector (Suez GE Sievers M9 TOC analyzer) was implemented to measure dissolved organic carbon (DOC) at various AMWs. A hydroxylated methacrylic polymer-based column (TOYOPEARL® HW-50S, Tosoh Bioscience LLC; 21 mm x 250 mm) was used. Eluent was prepared with 4 mM phosphate buffer (pH 6.8) and 25 mM sodium sulfate. 500 μ L of sample was injected and the sample run time was 120 min. Polystyrene sulfonates with molecular weights (MWs) of 891, 3420, 6430, 15800, 33500, 65400 and 152000 Da were injected as MW standards (Polymer Standards Service, Mainz, Germany).

TOC and DOC were analyzed using a Shimadzu TOC-L CSH Total Organic Carbon Analyzer. For DOC analyses, Micron's 0.45 μ m polyether sulfone disk filters were used for sample filtration using the method specified in Karanfil et al. (2003) prior to acidification. Approximately 10 mL of the samples were transferred into 20 mL glass vials for TOC and DOC analysis. They were then acidified to pH values lower than 3 using hydrochloric acid (35%, Fisher Scientific). Each sample and calibration curve point were measured five times by the instrument and the average of non-outlier values were reported as the final results.

UV and fluorescence spectra were simultaneously measured by Horiba Aqualog fluorometer (Horiba Scientific). UV spectra as well as UVA₂₅₄ were obtained by

scanning UV absorbance between 200 nm and 580 nm. Excitation-emission matrix (EEM) was obtained by scanning fluorescence from excitation wavelength of 225 nm to 450 nm and from emission wavelength of 250 nm to 580 nm. The UV absorbance of all the samples is greater than 0.05 cm^{-1} ; therefore, the inner filter effects were corrected according to the method described by Lakowicz (2013). Light scattering, including Rayleigh and Tyndall, were removed using three-dimensional interpolation after subtracting the fluorescence spectra of Milli-Q water from the fluorescence spectra of samples (Zepp et al., 2004), then the unit were converted to Raman unit (RU) based on the integrated area of Raman peak of Milli-Q water (Lawaetz and Stedmon, 2009). All the EEM data process and visualization were conducted using MATLAB R2015b (Mathworks).

Scaling indices were calculated using the Phreeqc aqueous phase thermodynamic modeling package from the USGS. The Phreeqc model uses extended Debye–Huckel and the Davies equation for modeling solution phase activity coefficients (Parkhurst and Appelo, 2013).

A Hach turbidity meter was used to measure the turbidity of the samples right after being collected.

Results and Discussion

Treatment Technologies

Fluidized Bed Crystallization Reactor (FBCR)

There are three chemicals used to increase the pH in FBCR: calcium hydroxide, sodium carbonate and sodium hydroxide. Water quality, waste production, temperature, operation and costs are the main factors in order to select the most suitable chemical. Low alkalinity feed requires the use of sodium carbonate while sodium hydroxide is the most suitable for intermediate to high alkalinity. According to previous studies, using sodium hydroxide results in smaller waste production, minimal operation efforts, reliability in low temperatures and applicability in variety of water qualities (Graveland et al., 1983; Vanderveen and Graveland, 1988). Since the alkalinity of the secondary effluent is in the intermediate range, sodium hydroxide is chosen for this study.

Using sodium hydroxide, pH values of secondary effluent is increased to 10.5, 11, 11.5 and 12 in order to promote crystallization in the FBCR. The highest supersaturation levels (supersaturation levels immediately after injection of sodium hydroxide to the column) of mineral solids are presented in Table 6. The saturation index (SI) is calculated using the following equation:

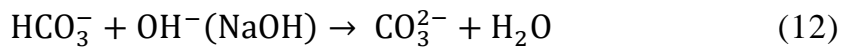
$$SI = \log \frac{\prod a_i^{v_i}}{K_{sp}} \quad (11)$$

where a_i is the activity of ion i , v_i is the stoichiometric coefficient for species i in the mineral dissolution reaction and K_{sp} is the solubility product for the mineral dissolution reaction.

Table 6 Highest SI values and Turbidity for different pH values in FBCR compared to secondary effluent

Parameters	Secondary effluent	pH			
		10.5	11	11.5	12
Turbidity (NTU)	1.1	1.4	1.4	1.3	1.6
SI					
CaCO ₃ (Calcite)	0.07	2.36	2.38	2.41	2.42
CaSO ₄ (Gypsum)	-1.39	-1.81	-1.86	-1.97	-2.10
CaMg (CO ₃) ₂ (Dolomite)	-0.20	4.46	4.52	4.53	4.42
BaSO ₄ (Barite)	0.39	0.22	0.19	0.12	0.01
Mg(OH) ₂ (Brucite)	-5.67	1.40	1.36	2.23	3.02
CaMg ₃ (CO ₃) ₄ (Huntite)	-5.08	4.31	4.45	4.42	4.07
MgCO ₃ (Magnesite)	-0.85	1.52	1.56	1.54	1.41

By increasing the pH values to 11.5, the SI values are increased for calcite, dolomite, Brucite and magnesite which is due to the increase in CO₃²⁻ concentration by the following reaction:



However, the SI values are decreased for gypsum and barite which is because of the ionic activity reduction due to increase in ionic strength of the stream. The SI values are leveled out or decreased for dolomite, Brucite and magnesite when the pH of the stream is increased to 12. This is because of conversion of almost all of the HCO₃⁻ to

CO_3^{2-} while the activity coefficients are decreased due to increase in ionic strength of the stream. However, the SI value for Brucite keeps going up since it is not limited by the CO_3^{2-} content of the stream and sodium hydroxide provides the OH^- .

While the initial (highest) SI values for calcite are above 1.7 (recommended SI value for calcite to prevent spontaneous homogeneous nucleation) (Graveland et al., 1983), the turbidity values demonstrates an insignificant increase compared to a previous study (Harms and Robinson, 1992) verifying a dominant heterogeneous precipitation on the garnet sand. This is due to the injection of sodium hydroxide from 4 different locations throughout the garnet bed minimizing the effect of an extreme SI value at the injection points. Moreover, injecting sodium hydroxide in a 90 degrees angle to the secondary effluent stream results in better mixing, thereby avoiding the microfloc production and solids carryover to the 5 um filter. Using small garnet sand is also beneficial since it provides more surface area and minimizes the possibility of homogenous precipitation.

Figure 9 demonstrates the Calcium, magnesium and silica removal at 4 different pH values (10.5, 11. 11.5 and 12). Calcium is precipitated as calcium carbonate and reaches to 97% removal at pH 12. Magnesium is precipitated as magnesium carbonate or incorporated into the crystal lattice of calcium carbonate at pH 10.5 (Graveland et al., 1983; Russell et al., 2009). It also precipitates as magnesium hydroxide at higher pH values and reaches to >99.9% removal at pH 12.

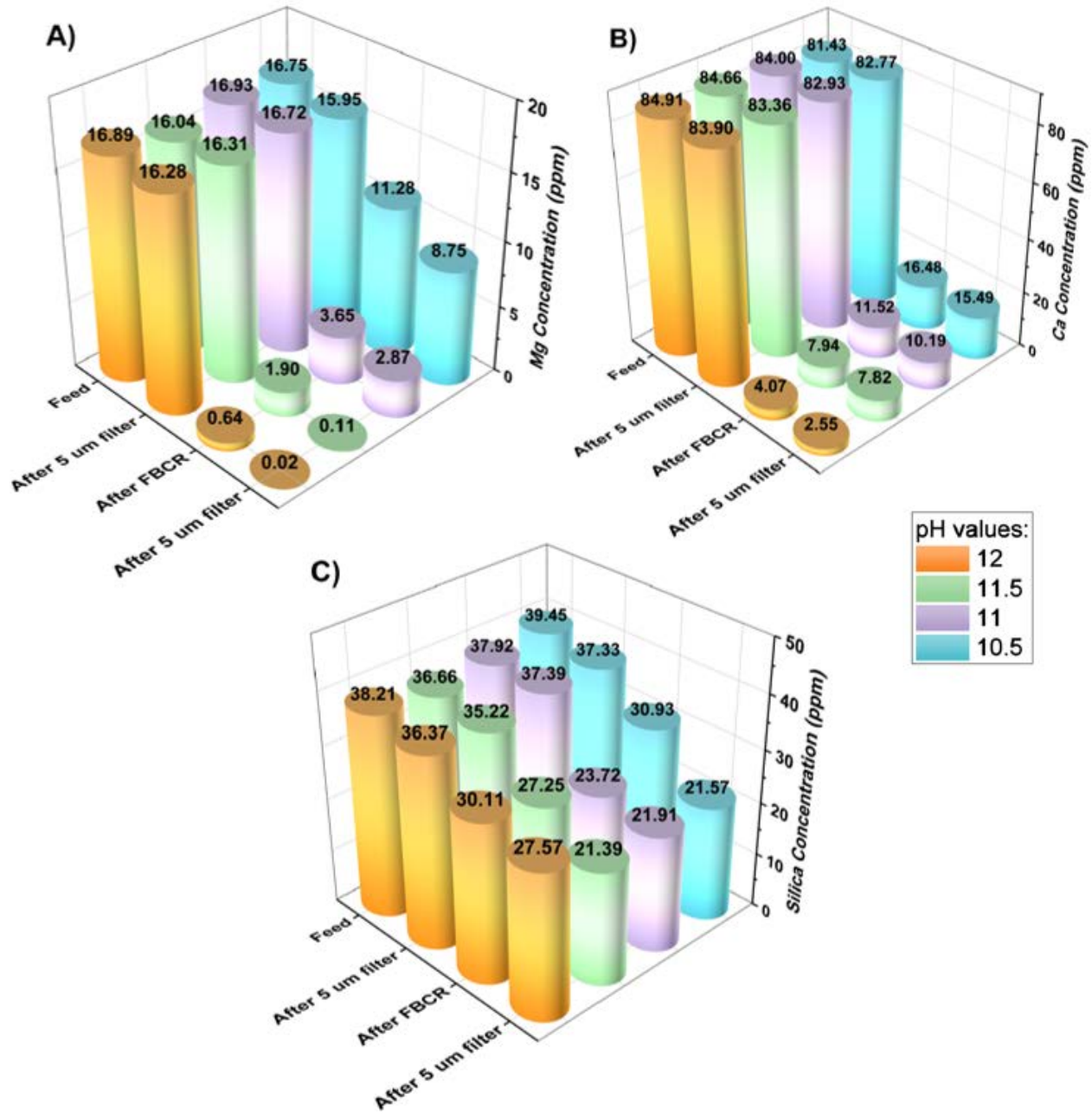


Figure 9 A) Mg, B) Ca and C) Silica removal rates at different pH values in FBCR

It is of high importance to remove silica prior to high-pressure membrane filtration. Silica fouling causes efficiency reduction in membrane processes due to high-pressure drops, un-steady state operation, damage to membranes and increase in overall costs (Sahachaiyunta et al., 2002). Silica is found in three forms in water

supplies: dissolved (reactive) silica, colloidal (unreactive) silica and particulate silica. Colloidal silica is widely thought to be either a silicon polymerized with multiple units of silicon dioxide or a silicon that formed a loose bond with organic or complex inorganic compounds (Sahachaiyunta et al., 2002). Dissolved silica (monosilicic acid) results in a impervious glass-like fouling on the membrane whereas colloidal silica forms a more porous film on the membrane surface (Sheikholeslami and Tan, 1999). Silica fouling is categorized in two forms: precipitation fouling and particulate fouling. Precipitation fouling is defined as polymerization of monomeric silica on the membrane surface whereas particulate fouling characterized as colloids accumulation, previously formed in bulk solution, on the membrane surface (Sheikholeslami and Tan, 1999). In addition to membrane fouling, colloidal silica creates problems for other treatment processes due to its stability as an un-ionized compound, limiting the treatment processes able to remove it.

In addition to membrane processes, lime softening using $Mg(OH)_2$ and FBCR in elevated pHs are able to remove dissolved and colloidal silica. Dissolved silica is removed as $MgO(SiO_2)_x \cdot (H_2O)_x$ and colloidal silica is removed by calcium carbonate co-precipitation or adsorption on garnet sand. According to Figure 9, At pH 11.5, 42% of silica removal can be achieved. The removal rate of silica is reduced at pH value of 12 which is due to homogeneous precipitation promotion at high pH values along with magnesium content depletion.

According to previous studies, natural organic matter (NOM) can be removed by calcium carbonate or magnesium hydroxide co-precipitation during softening (Gerwe, 2003; Liao and Randtke, 1985; Randtke et al., 1982; Russell et al., 2009). NOM removal occurs by surface adsorption to the calcium and magnesium precipitates or by direct precipitation as calcium or magnesium humate or fulvate (Russell et al., 2009). Calcite, the most thermodynamically stable form of calcium carbonate, demonstrates a highly structured rhombohedral shape and possess a

negatively charged surface during softening, although the surface charge depends on aqueous concentrations of Ca^{2+} , HCO_3^- , CO_3^{2-} . As shown in Figure 10, at pH value of 10.5, there is a 7.5% reduction TOC concentration. Even though the negative surface charge of calcite is unfavorable to adsorb negatively charged NOM, incorporation of magnesium in the calcium carbonate crystal as well as presence of calcium ions in the stream results in a positive surface charge (or lesser negative charge) on the calcite precipitates. Therefore, small NOM co-precipitations are seen at pH 10.5. By increasing the pH to higher values, $\text{Mg}(\text{OH})_2$ precipitation becomes favorable. $\text{Mg}(\text{OH})_2$ forms a positively-charged noncrystalline precipitates with higher surface area compared to calcite (Russell et al., 2009). Therefore higher NOM removals (26% removal at pH 12) are being achieved at higher pH values. Furthermore, at high pH values, CaOH^+ and MgOH^+ formation could result in direct precipitation of calcium or magnesium humate or fulvate (Russell et al., 2009). It is important to note that the characteristics of NOM have a substantial influence on its removal rate by FBCR or softening. Generally, hydrophobic and highly aromatic organic matter is the main type of NOM that is being removed by FBCR or softening. The removal rates of UV_{254} and total fluorescence (TF) are presented in Figure S4. Reduction on UV_{254} at high pH values confirms the aromatic compounds removal by FBCR.

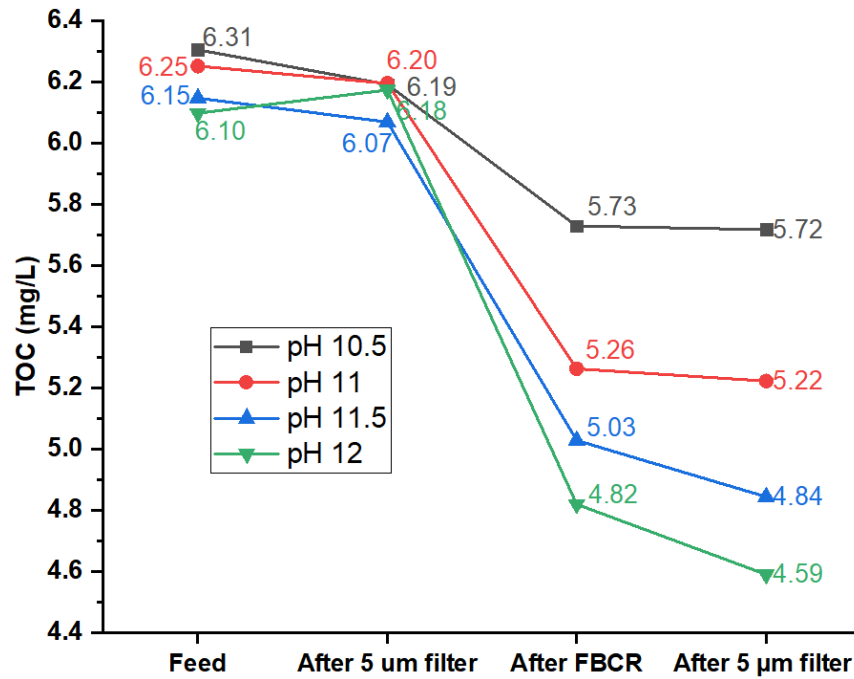
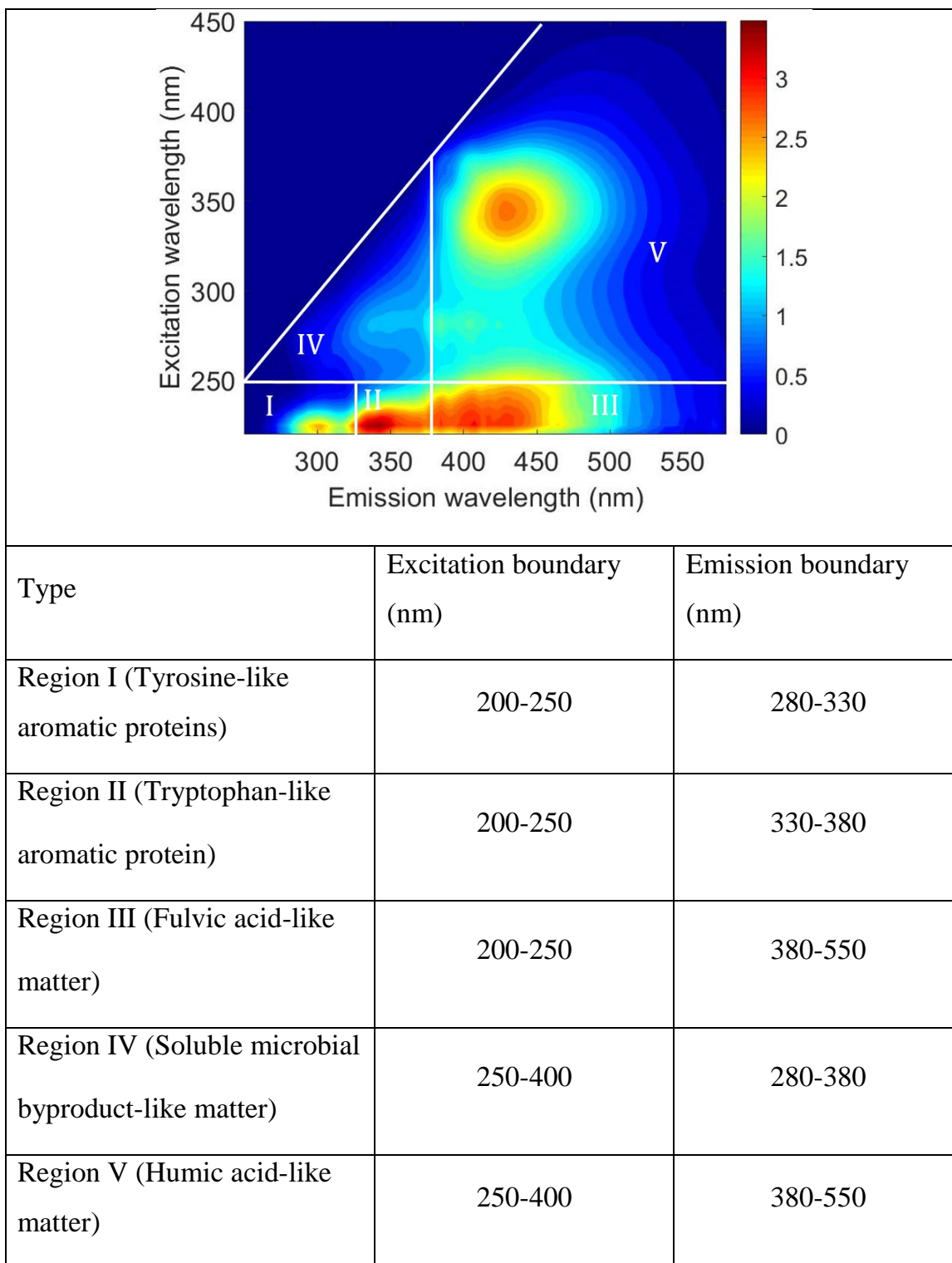


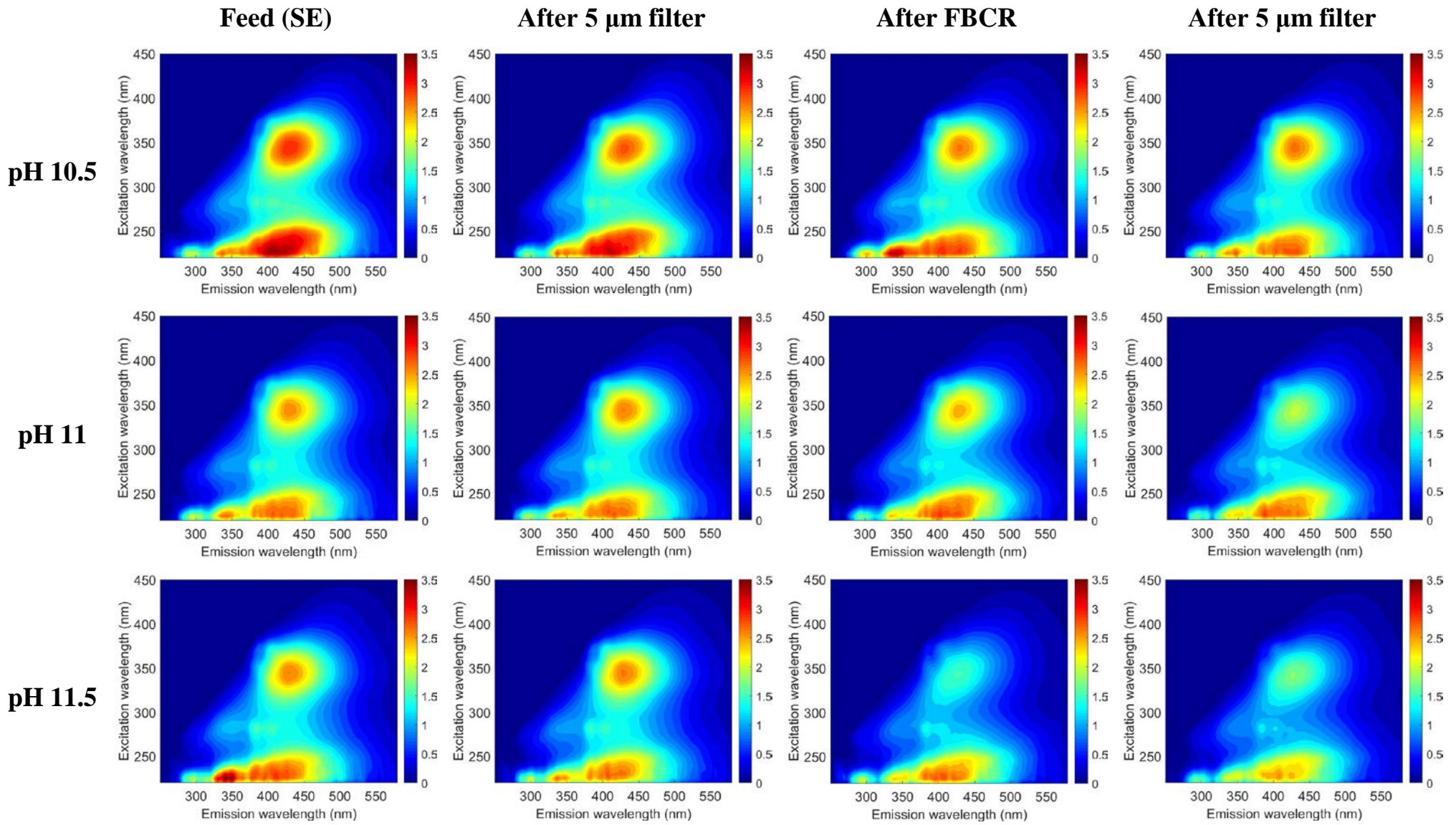
Figure 10 TOC concentrations of secondary effluent treated by FBCR.

According to previous studies, EEM is a useful tool to provide insight regarding the types of NOM that is being removed by treatment processes. There are five regions in every EEM figure (shown in Table 7) that correspond to different types of NOM (Chen et al., 2003; Park and Snyder, 2018).

Table 7 Excitation-emission boundaries for five operationally-defined fluorescence region



EEM figures for the SE after treating by FBCR at different pH values are shown in Figure 11. Based on the EEM spectra shown in this figure, FBCR is capable of reducing the NOM content of SE regardless of its type. It is also noticeable that the humic-like matter (region V) and fulvic-like matter (region III) are mainly reduced at higher pH values.



pH 12

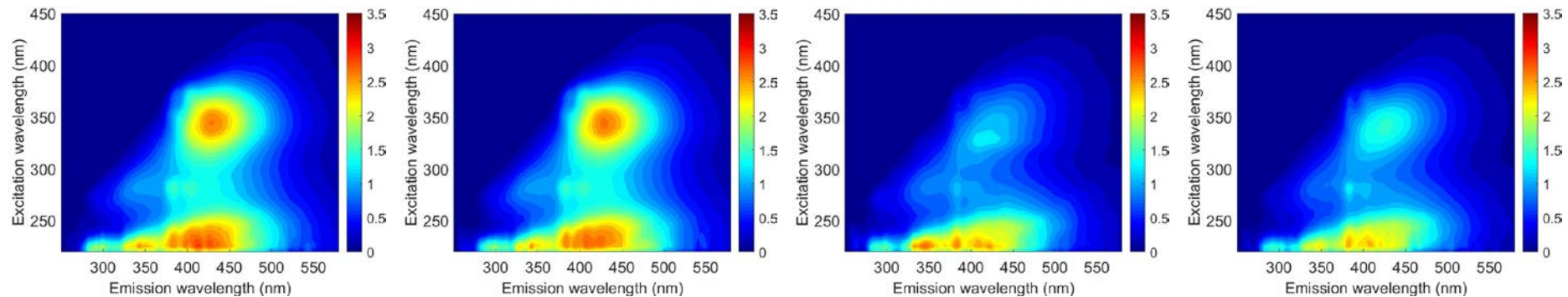


Figure 11 EEM figures for each stage at four different pH values

Figure 12 presents the SEC-OCD results for SE treatment using FBCR. As shown in the figure, there is an overall trend of organic carbon reduction by every increase in pH which is in accordance with the TOC and EEM results. Looking at pH 10.5 and 11, there is an approximately even reduction in all 3 peaks at pH 10.5 while there is slightly higher reduction in smaller molecular weight peak for pH 11. Based on the results presented in Figure 9, comparing the calcium and magnesium removals at pH 10.5 and 11, there is a significant magnesium removal which is due to possible MgCO_3 and Mg(OH)_2 precipitation. These noncrystalline precipitates have much higher surface area compared to calcite and this might be a reason for higher organic carbon reduction at the smallest molecular weight peak. Another possibility is direct precipitation of magnesium as magnesium fulvate or humate which results in smaller molecular size compared to co-precipitation particles.

At pH values of 11.5 and 12, SEC-OCD results demonstrates an increase in the biggest molecular peak for the after FBCR samples which are subsequently being removed by a 5 μm filter. This phenomenon shows that co-precipitation of Mg(OH)_2 (that might include silica) and calcite (that might include magnesium) with NOM is the dominant method of NOM removal compared to direct precipitation.

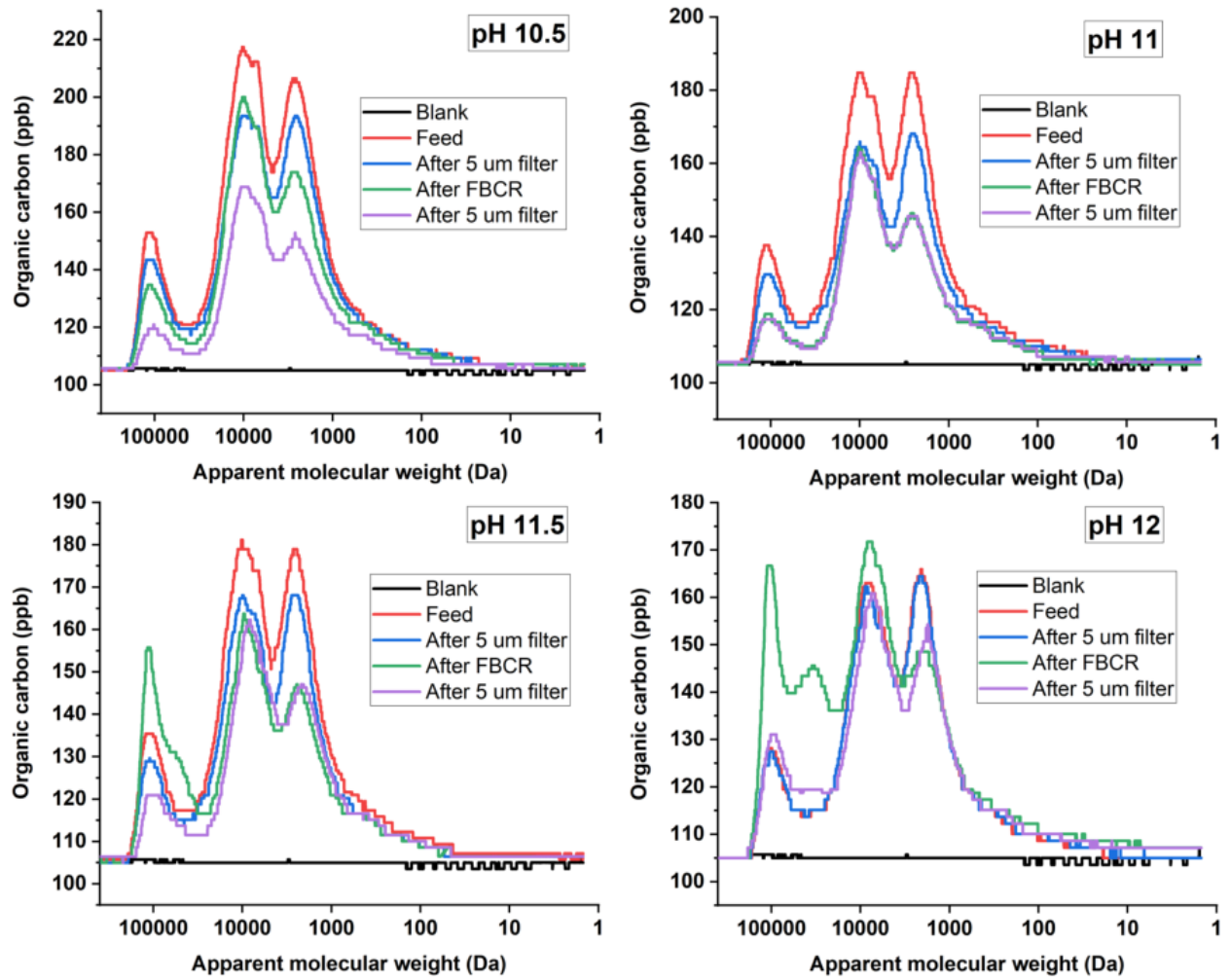


Figure 12 SEC-OCD results for SE treated by FBCR at different pH values

Ultrafiltration (UF)

UF is another common pretreatment for high-pressure membrane processes. UF operates as a physical barrier with pore sizes ranging from 0.002 to 0.1 μm and it is able to achieve over 4 log removal of pathogens such as *Giardia* and *Cryptosporidium* as well as viruses (Voutchkov, 2017). As shown in Table 8, UF is able to remove approximately 93% of turbidity and 18% of colloidal silica. It is also known that UF is incapable of removing inorganic minerals such as calcium and magnesium. It is also shown that UF is able to remove 13% of TOC in the SE.

Table 8 Turbidity, TOC and inorganic cations' concentration in UF treatment

	SE	UF PERMEATE	UF BACKWASH
Turbidity (NTU)	1.1 ± 0.2	0.08 ± 0.01	1.8 ± 0.2
Calcium (mg/L)	86.4 ± 2.2	83.3 ± 3.8	85.4 ± 3.4
Magnesium (mg/L)	18.2 ± 1.1	18 ± 0.8	18.2 ± 1.2
Silica (mg/L)	34.1 ± 4.5	27.9 ± 3.8	39.3 ± 3.4
TOC (mg/L)	6.15 ± 0.3	5.37 ± 0.2	12.97 ± 0.3
DOC (mg/L)	5.10 ± 0.2	4.48 ± 0.1	8.86 ± 0.2

EEM spectra for the UF permeate and UF backwash are shown in Figure 13. By taking the guideline introduced in Table 7 into consideration, UF is mainly capable of removing NOM from region I (Tyrosine-like aromatic proteins), region II (Tryptophan-like aromatic protein) and region IV (Soluble microbial byproduct-like matter) as the fluorescence intensity in these regions are weakened in UF permeate

EEM while these regions have stronger intensity in the UF backwash sample compared to SE EEM spectra. There is an insignificant NOM removal from region III (Fulvic acid-like matter) and region V (Humic acid-like matter) which is due to the smaller size of humic and fulvic acid-like matter compared to proteins present in region I and II.

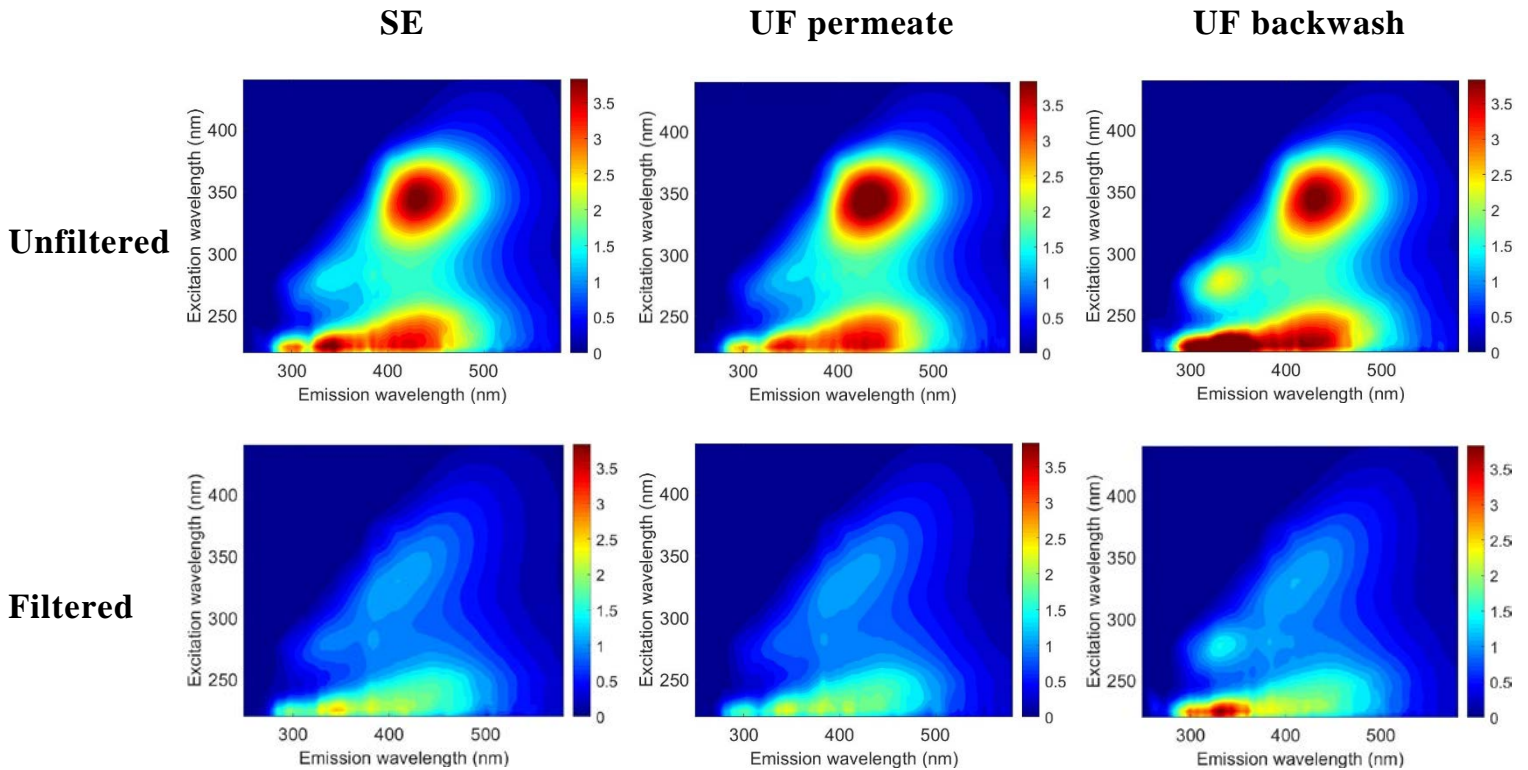


Figure 13 EEM spectra for filtered and unfiltered SE, UF permeate and UF backwash

Ferric Chloride Coagulation and Flocculation

One of the proven methods for membrane fouling reduction is coagulation (Ho et al., 2015; Racar et al., 2017). Ho et al. (2015) studied the removal efficiency of three coagulants: Polyaluminum chloride (PACl), aluminum chlorohydrate (ACH) and ferric chloride (FeCl_3).

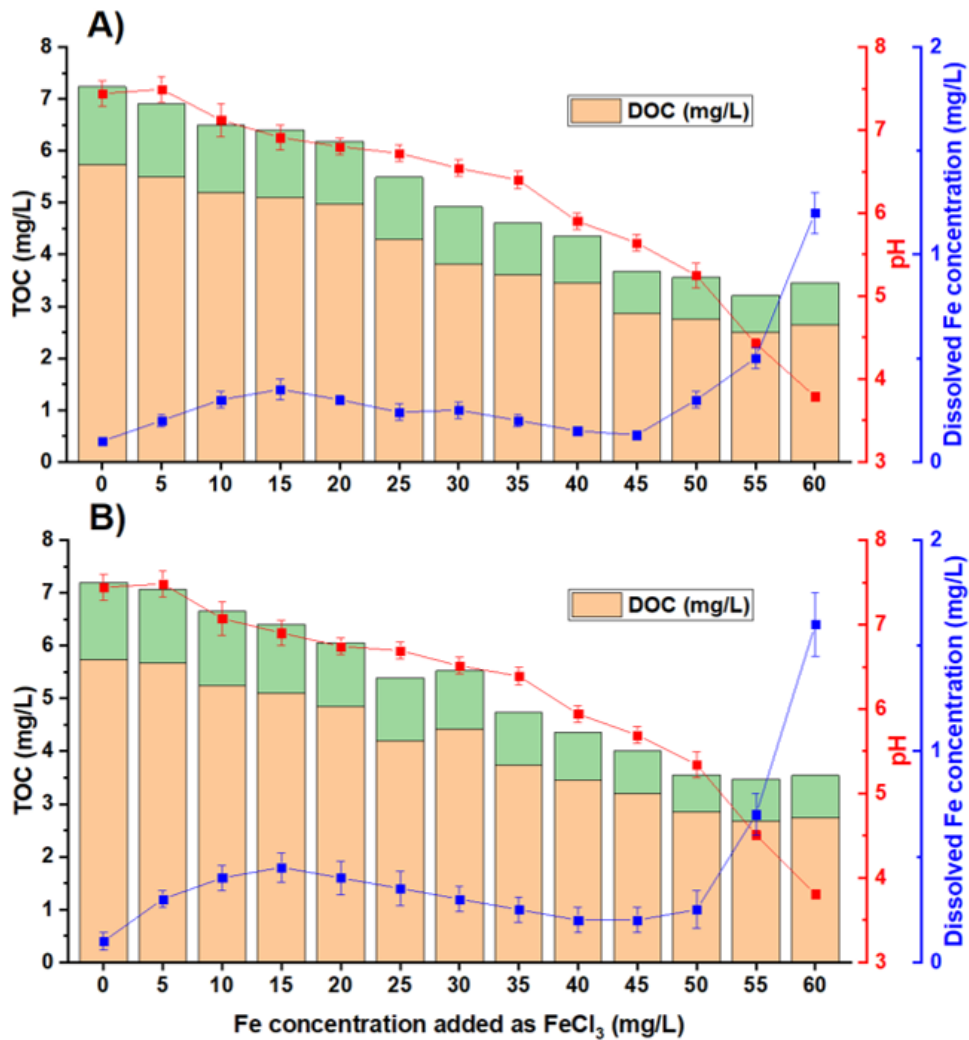


Figure 14 TOC, DOC, pH value and dissolved Fe concentration for different doses of FeCl₃ for A) 20 min flocculation and B) 30 min flocculation

At optimal dose and pH value, FeCl₃ was able to remove 55% of DOC compared to 31% of PACl and 27% of ACH. This significant difference in DOC removal is attributed to the fact that FeCl₃ polymerizes in the solution while the other coagulants are already polymerized, therefore having lesser surface area for adsorption and co-precipitation of NOM. Previous studies also have shown that FeCl₃ is capable of removing 100% of Phosphate at optimal dose and pH values (Aghdam et al., 2016).

As shown in Figure 14, increasing FeCl_3 dose results in TOC concentration reduction up to 55 mg/L for both 20 min and 30 min flocculation. At this dose, 56% and 48% of TOC is removed for 20 min and 30 min of flocculation, respectively. According to Figure 14, dissolved Fe concentration demonstrates a greater increase for 30 min flocculation compared to 20 min flocculation. This sharper dissolved Fe concentration for approximately similar pH values along with lower TOC removal hints a possible destabilization of precipitates at longer mixing time (Ho et al., 2015).

For the purpose of identifying the optimal conditions for FeCl_3 coagulation and flocculation, achieving the lowest dissolved Fe concentration is a higher priority compared to achieving the maximum TOC removal. This is due to the fact that dissolved Fe can cause membrane fouling in very low concentrations. Therefore, the optimal conditions are: 20 min flocculation, 45 mg/L Fe dose and resulting pH of 5.64 for the SE which results in 49% DOC and 16% silica removal leaving 130 $\mu\text{g/L}$ of dissolved Fe concentration in the effluent solution. The turbidity for the effluent of coagulation process at optimized conditions after being filtered with 5 μm polypropylene filter is below 0.1 NTU. The resulting pH of 5.64 is very similar to Racar et al. (2017) study (5.58). This slightly acidic pH results in lesser negative charge on the particles as well as the NOM.

Figure 15 presents the EEM spectra for Fe doses (as FeCl_3) of 15, 30 and 45 mg/L. Unlike the UF, FeCl_3 coagulation and flocculation is able to effectively remove all five types of NOM. The higher NOM removal across all five regions might be due to the polymerization of monomeric Fe^{3+} species into the medium polymer species such as $\text{Fe}_2(\text{OH})_2^{4+}$ and $\text{Fe}_3(\text{OH})_4^{5+}$ that could entrap small humic and fulvic acid-like NOM particles that were too small for UF to filter them.

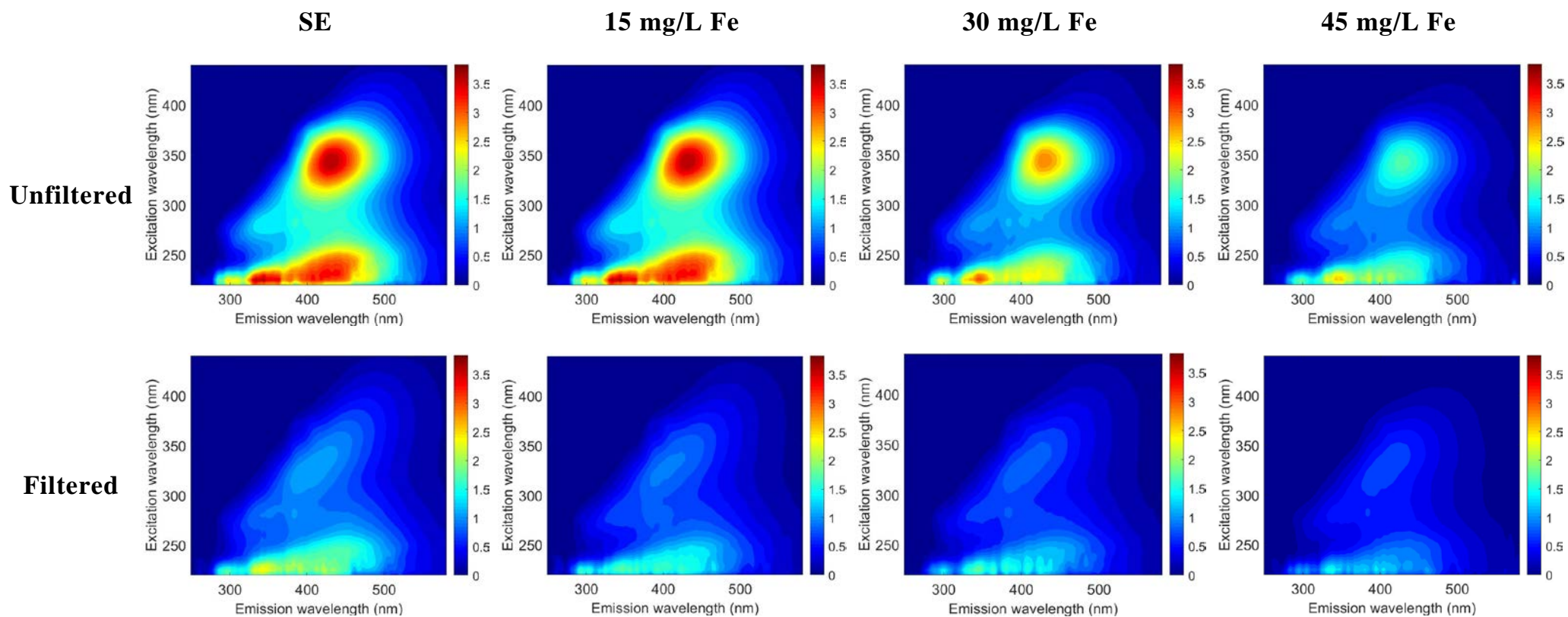


Figure 15 EEM spectra for selected Fe doses as FeCl_3

NOM Characterization for Discussed Treatment Technologies Using Parallel Factor (PARAFAC) Analysis Method

NOM is present in all natural aquatic environments. NOM is one of the biggest sources of biologically active carbon; however, a great portion of it remains uncharacterized (Benner, 2002). This is due to the fact that NOM consists of a complicated mixture of organic matter that varies greatly in molecular weight and is susceptible to degradation and alteration in composition when sample preparation is required to analyze it using traditional chemical techniques (Stedmon and Markager, 2005a). A practical method to characterize and trace NOM (or DOM) dynamics is to measure fluorescence of the fraction of the NOM (or DOM) that fluoresces (Stedmon et al., 2003). A recently refined technique that combines the EEM spectra and parallel factor (PARAFAC) data analysis has shown to be a valuable tool to characterize NOM (or DOM) and trace its many different fractions in natural aquatic environments (Stedmon et al., 2003).

The EEM spectra of previously discussed pretreatments are analyzed by PARAFAC in order to achieve a better understanding of the types of NOM that are present in the wastewater and the efficiency of these treatments in removing them. Figure 16 demonstrates the EEM spectra of five different components found in these samples. The fluorescence spectra of these five components show a resemblance to organic fluorophores by having multiple excitation maxima for a single emission maxima (Stedmon and Markager, 2005a).

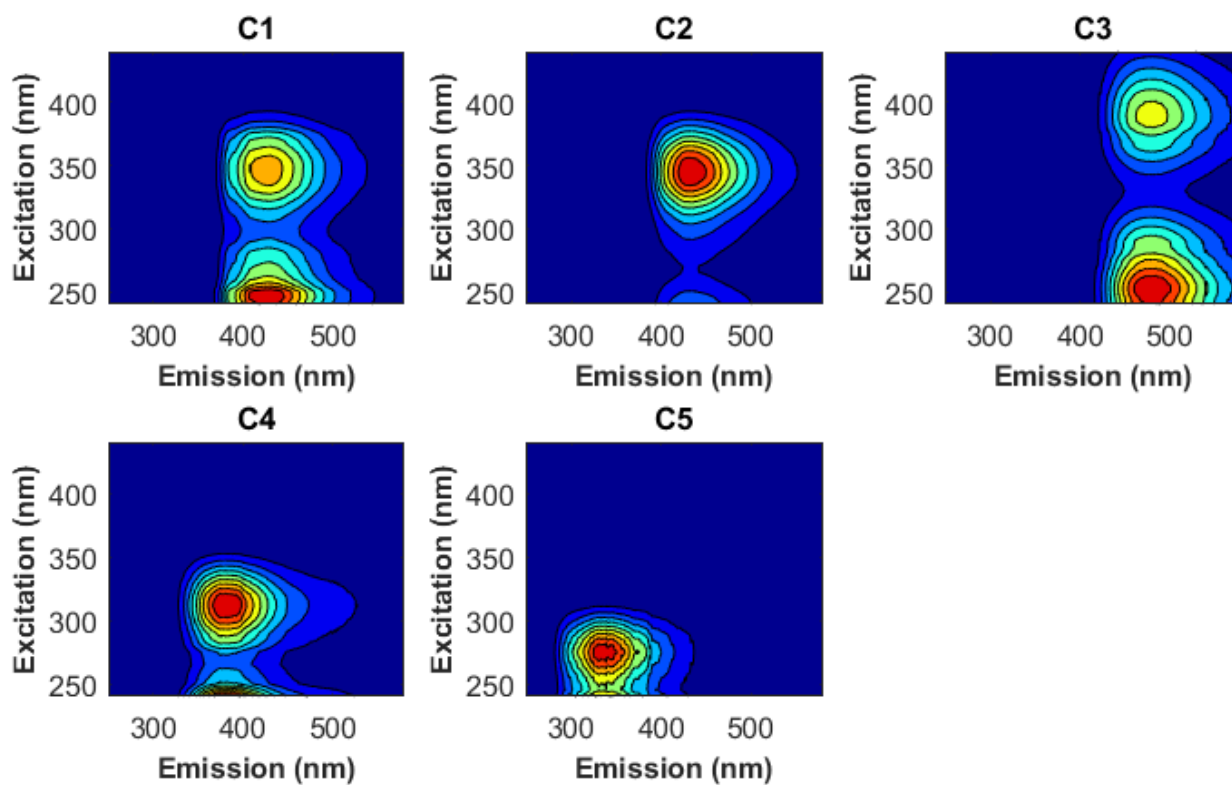


Figure 16 Contour plots of five different components identified from the EEM spectra of FBCR, UF and FeCl₃ coagulation and flocculation samples using PARAFAC

After investigating previous studies, five different components of this study were matched with a probable source and fraction of NOM and the results are shown in Table 9.

Table 9 Comparison of the identified components of this study with previous studies

Component of this study	Excitation/Emission wavelength	Description and probable source of the component (Reference)
C1	255 (350)/420	Common to a wide range of freshwater Environments, Anthropogenic humic

		fluorophore group, (C6), <250 (320)/400 (Stedmon and Markager, 2005a)
		Terrestrial humic substances, (P8), <260 (355)/434 (Murphy et al., 2008)
		Terrestrial humic substances, (C5), 250 (340)/440 (Baghoth et al., 2011)
C2	<250 (350)/440	Terrestrial/autochthonous fulvic acid fluorophore group, (C4), <250 (360)/440 (Stedmon and Markager, 2005a)
C3	260 (390)/492	Terrestrial humic substances, widespread, (P3), <260 (380)/498 (Murphy et al., 2008)
		Terrestrial humic substances, (C1), 260 (360)/480 (Baghoth et al., 2011)
		Terrestrial humic substances, (C3), 270 (360)/478 (Stedmon et al., 2003)
C4	<250 (320)/390	Marine and terrestrial humic substances, (C6), <250 (300)/406
		Microbial humic, (C4), <250 (305)/390 (Yamashita and Jaffe, 2008)
C5	<250 (275)/340	Tryptophan-like, protein-like, (Peak T type) (Coble, 1996)
		Amino acids, free or bound in proteins, (P7), 280/342 (Murphy et al., 2008)
		Amino acids, free or protein bound, (C4), <250 (290)/360

According to Table 9, three of five components are humic-like substances. Comparing the EEM maxima spectra of C4 with C1, Component C1 has higher excitation wavelength for an approximately similar emission. Excitation at higher wavelength for C1 shows that the fluorophores responsible for this fluorescence contain several functional groups or have higher aromaticity (Coble et al., 1998). Comparing C1 with C3 humic substances, component 3 has longer emission wavelength compared to C1. This might be due to presence of more conjugated fluorescing molecules in C3 compared to C1 (Stedmon et al., 2003).

Component 5 is identified as tryptophan-like protein in several studies mentioned in the Table 9. While tyrosine-like proteins were identified and discussed earlier in this study, PARAFAC was not able to assign a component for that type of proteins. This might be due to the fact that the fluorescence of tyrosine can be difficult to detect because of the energy transfer to tryptophan-like proteins as well as quenching by neighboring groups (Stedmon and Markager, 2005b). Another reason is that the number of samples (140 filtered and unfiltered samples) in the dataset might have limited the analysis. This may result in a merger of two fluorophore groups into one group (Stedmon and Markager, 2005a). Component 5 of this study possesses a wide emission maxima and the difference in emission maxima for tyrosine (310 nm) and tryptophan-like (340 nm) is 30 nm (Coble, 1996). Therefore, C5 in this study will be representative of both protein groups.

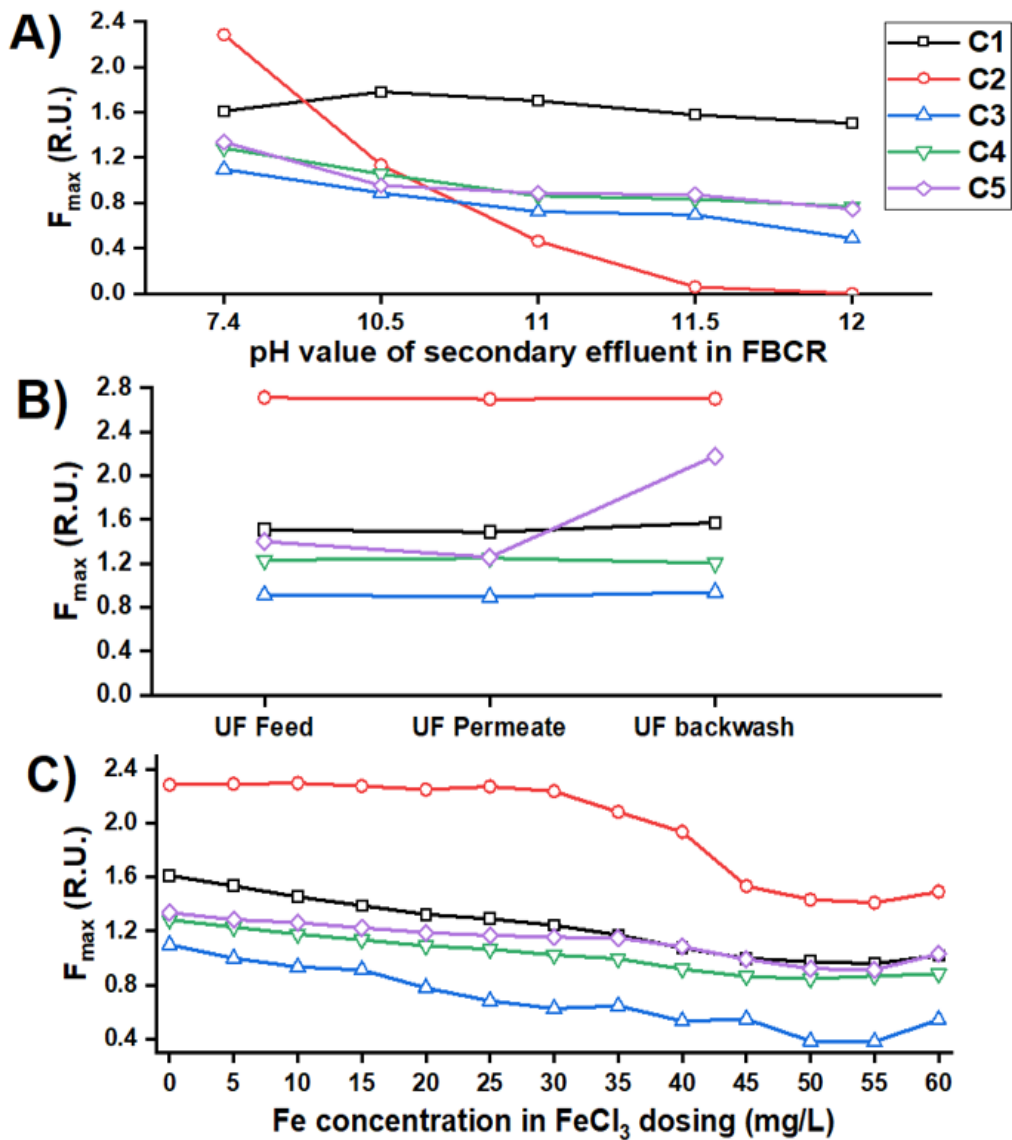


Figure 17 F_{\max} values for different conditions in A) FBCR, B) UF and C) FeCl_3 coagulation and flocculation

Figure 17 demonstrates the maximum fluorescence intensity (F_{\max}) values for different conditions of FBCR and FeCl_3 coagulation and flocculation as well as UF process. F_{\max} provides an estimate of the relative concentrations of each component therefore, direct comparison among the components requires information regarding their quantum efficiency magnitude as well as their individual responses to quenching effects (Baghoth et al., 2011). However, these information is not needed for the purpose of this study due to the fact that this study – as mentioned before –

aims to compare same components' removal in different pretreatments in order to suggest a sustainable pretreatment train that can efficiently remove the scaling and fouling precursors prior to a high-pressure membrane treatment process.

As shown in Figure 17 A), FBCR is able to reduce the F_{\max} value for all five components. FBCR is able to remove 7% of C1, 100% of C2, 55% of C3, 40% of C4 and 44% of C5. Component 1 shows the lowest removal rate among the five groups. Compared to C3, C1 has more functional groups that are deprotonated at high pH values which results in high negative surface charge for these components. As shown in the figure, there is no removal for this component until pH values above 11.5 which might be due to precipitation of $Mg(OH)_2$ which possesses a highly positive surface. Figure 17 B) presents the F_{\max} values for the UF process. UF shows slight to no removal for components 1 to 4. This is due to the fact that all of these components are not big enough in size to be caught by the membrane. However, it is able to remove a portion (11%) of component 5 that represents large amino acid molecules. Unlike UF, $FeCl_3$ coagulation and flocculation is able to remove portions of NOM from all five groups: 40% of C1, 38% of C2, 65% of C3, 34% of C4 and 26% of C5.

Conclusions

This study investigated the efficiency of three different treatments in removing different scale-forming and fouling substances prior to feeding the secondary effluent to a high-pressure membrane filtration process. Furthermore, statistical analyses has been conducted using EEM-PARAFAC in order to characterize the NOM present in the secondary effluent. Following are the main conclusions achieved by this study:

- FBCR is a reliable treatment option compared to softening since the residence time is orders of magnitude lesser compared to the softening process. In this study, more than 99.9% of magnesium, 97% of calcium and 42% of silica was removed thereby, eliminating any chances of scaling in the later stages of the

process. Compared to softening that magnesium precipitation is avoided due to bad settling characteristics, FBCR requires lesser chemical to achieve same pH values in softening due to requirement of lesser saturation index value to initiate the precipitation.

- FBCR was also a prominent process for removing NOM through co-precipitation. As shown by SEC-OCD results, this phenomenon initiates at pH values of 11.5 where the $Mg(OH)_2$ precipitation is dominant. FBCR was able to remove 26% of TOC and it was able to remove portions of TOC from different components identified using EEM-PARAFAC.
- While UF was able to remove 93% of the turbidity, the TOC removal was half of the FBCR. It was also shown by EEM-PARAFAC that UF is only able to remove protein-like NOM and, if used as a pretreatment, the other types of the fouling substances will accumulate on the surface of the membranes operating at high pressures in the later stages. UF is also successful in removing the colloidal portion of silica that later may cause fouling issues for it.
- Ferric chloride has shown to be the superior coagulant for coagulation processes. In this study, 55 mg/L of iron dose resulted in 56% TOC removal. However, in order to minimize the iron dose leaving this pretreatment, 45 mg/L is the optimized concentration. This results in iron residuals as low as 130 $\mu\text{g/L}$. Ferric chloride was also able to reduce the concentration of all five different types of NOM thereby, presenting itself as a strong pretreatment option prior to NF/RO filtration.

Results of this study shows that combination of FBCR and Ferric chloride coagulation would result in highest reduction of scale-forming and fouling substances which will minimize the chance of fouling in the later NF/RO filtration processes. UF has shown high turbidity removal compared to FBCR; however, the effluent of ferric chloride coagulation and flocculation process has shown a similar

values after being filtered by a 5 μm filter which would result in a cost effective process.

APPENDIX A – SUPPLEMENTARY MATERIAL

Table S1. Aqueous limits of detection (LOD) for the elements speciated by ICP-QQQ and water-soluble ions speciated by IC. TMA & DEA represent the sum of trimethylamine and diethylamine.

ICP	ppt	IC	ppm
Ag	0.74	Adipate	0.023
Al	29.47	Ammonium	0.042
As	7.95	Calcium	0.045
Ba	3.70	Chloride	0.002
Cd	4.19	DMA	0.053
Co	0.72	Magnesium	0.037
Cr	1.15	Maleate	0.007
Cs	0.73	MSA	0.012
Cu	1.13	Nitrate	0.009
Fe	1.19	Oxalate	0.012
Hf	0.96	Phthalate	0.021
K	10.48	Pyruvate	0.064
Mn	1.62	Sodium	0.043
Mo	2.26	Succinate	0.011
Nb	0.52	Sulfate	0.012
Ni	2.84	TMA & DEA	0.315
P	770.73		
Pb	0.50		
Rb	1.57		
Se	82.39		
Sn	1.77		
Sr	1.10		
Ti	39.05		
Tl	0.38		
V	1.35		
Y	0.52		
Zn	5.88		
Zr	1.01		

Table S2. Kappa values used with weighted volume fractions to obtain kappa for individual stages of all MOUDI sets. Note that ‘Organics’ refers to the organics that could not be resolved by the IC, which only included specific organic salts. (a = Almeida et al., 2019 and references therein; b = Drozd et al., 2014; c = Hersey et al., 2013; d = Pöschl et al., 2019; e = Dusek et al., 2010; f = Rose et al., 2010; g = Laborde et al., 2012; h = Aldhaif et al., 2018).

Species	Density (g cm⁻³)	κ
(NH ₄) ₂ SO ₄	1.77	0.61 ^a
K ₂ SO ₄	2.66	0.69 ^a
CaSO ₄	2.32	0.00 ^a
NaCl	2.16	1.24 ^a
Mg(NO ₃) ₂	2.30	0.63 ^a
NaNO ₃	2.26	0.87 ^a
Na ₂ SO ₄	2.66	0.76 ^a
MgSO ₄	2.66	0.24 ^a
CaOxalate	2.12	0.02 ^b
MgOxalate	2.45	0.05 ^b
Na ₂ Oxalate	2.34	0.68 ^b
ZnOxalate	2.56	0.02 ^b
CaCl ₂	2.15	0.78 ^a
MgCl ₂	2.32	0.98 ^a
Ca(NO ₃) ₂	2.50	1.10 ^a
Organics	1.40 ^h	0.10 ^{c, d, e}
Black Carbon	2.00 ^h	0.00 ^{f, g}

Table S3. Pearson correlation coefficients (and p-values in parenthesis) between precipitation accumulation at MO, wind speed (WS), and various water-soluble ion concentrations after integration across all MOUDI stages.

Rain amount	1									
WS	-0.15 (0.56)	1								
Na ⁺	-0.72 (<0.01)	0.44 (0.07)	1							
Cl ⁻	-0.64 (<0.01)	0.41 (0.09)	0.88 (<0.01)	1						
ssNa ⁺	-0.66 (<0.01)	0.56 (0.02)	0.98 (<0.01)	0.87 (<0.01)	1					
Ca ²⁺	-0.14 (0.57)	-0.62 (0.01)	0.05 (0.85)	0.06 (0.82)	-0.12 (0.63)	1				
ssNa ⁺ + Cl ⁻	-0.68 (<0.01)	0.50 (0.04)	0.97 (<0.01)	0.97 (<0.01)	0.97 (<0.01)	-0.04 (0.89)	1			
Na ⁺ + Cl ⁻	-0.70 (<0.01)	0.44 (0.07)	0.97 (<0.01)	0.97 (<0.01)	0.95 (<0.01)	0.06 (0.83)	0.99 (<0.01)	1		
ssCa ²⁺	-0.71 (<0.01)	0.51 (0.03)	0.97 (<0.01)	0.88 (<0.01)	0.98 (<0.01)	-0.05 (0.84)	0.96 (<0.01)	0.96 (<0.01)	1	
nssCa ²⁺	-0.09 (0.73)	-0.66 (<0.01)	-0.04 (0.88)	-0.03 (0.91)	-0.21 (0.40)	0.99 (<0.01)	-0.12 (0.62)	-0.03 (0.89)	-0.14 (0.59)	1
Rain amount	WS	Na ⁺	Cl ⁻	ssNa ⁺	Ca ²⁺	ssNa ⁺ + Cl ⁻	Na ⁺ + Cl ⁻	ssCa ²⁺	nssCa ²⁺	

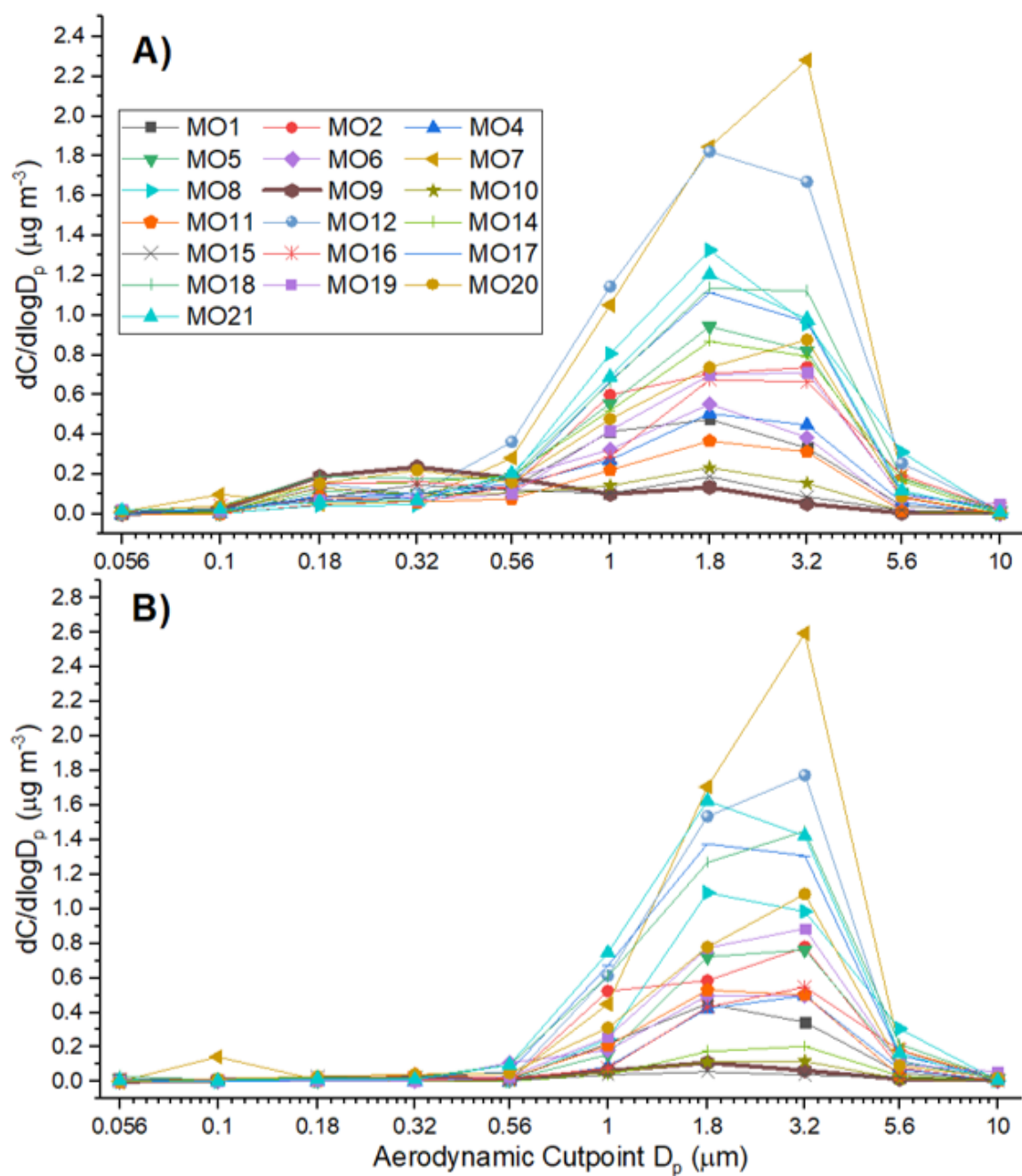


Figure S1. Mass size distribution for A) Na⁺ and B) Cl⁻ in all MOUDI sets. Data for set MO9 is highlighted in both panels as a thicker line in brown.

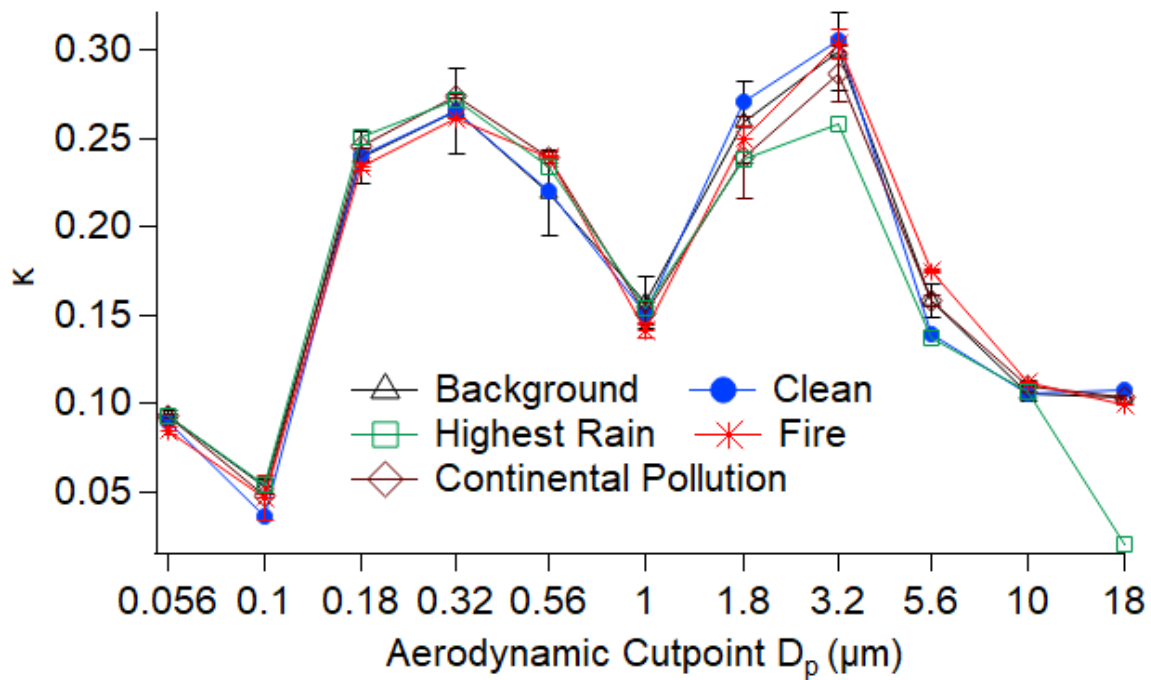


Figure S2. Average κ values for all MOUDI sets at each cutpoint diameter, categorized by pollution categories defined in Section 3.3.

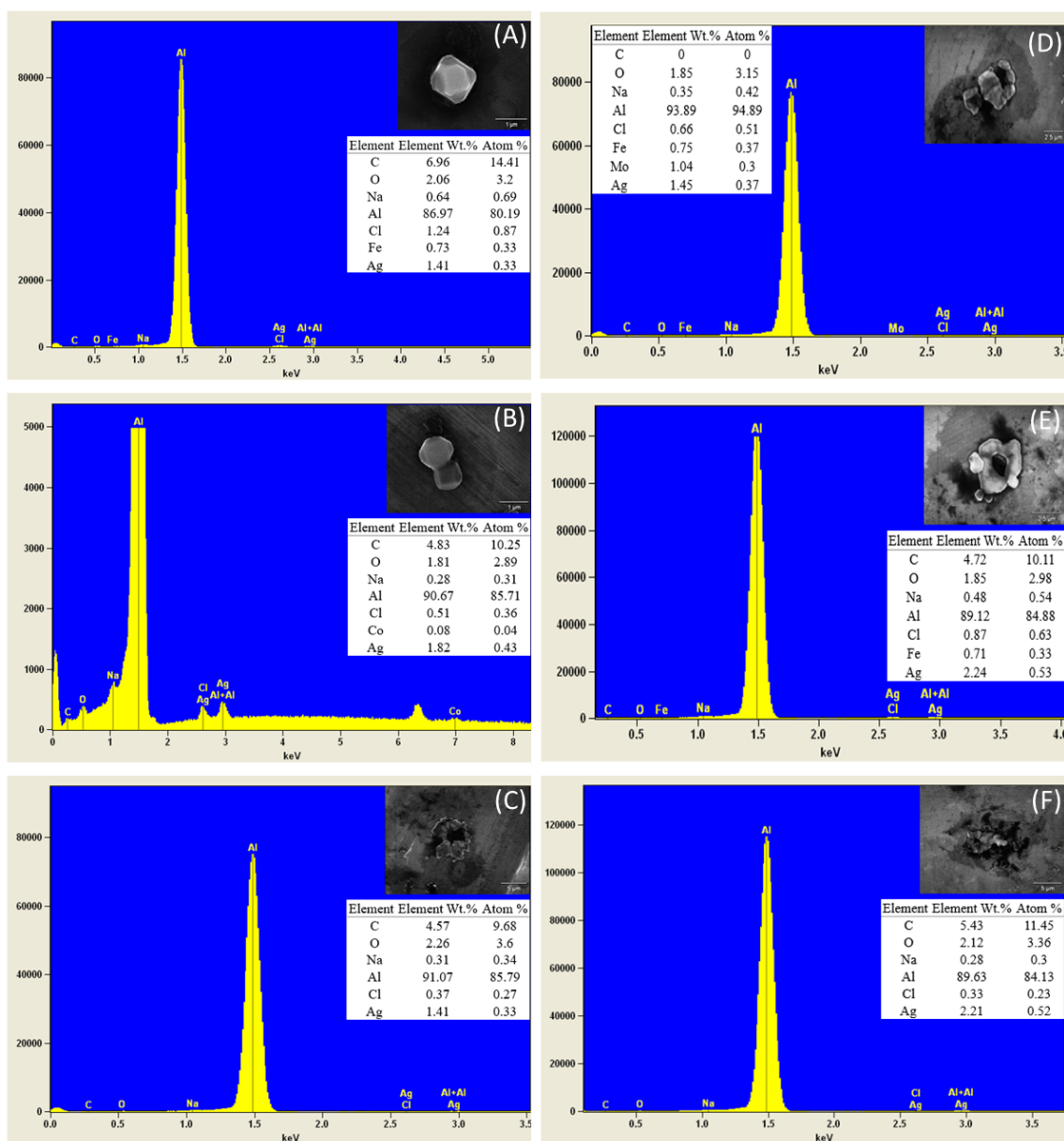


Figure S3. EDX spectra of SEM images shown in Figure 8. The tabulated results reveal that Fe, Mo and Co were present. Due to sampling on aluminum substrate filter, Al was the most abundant element in the examined area.

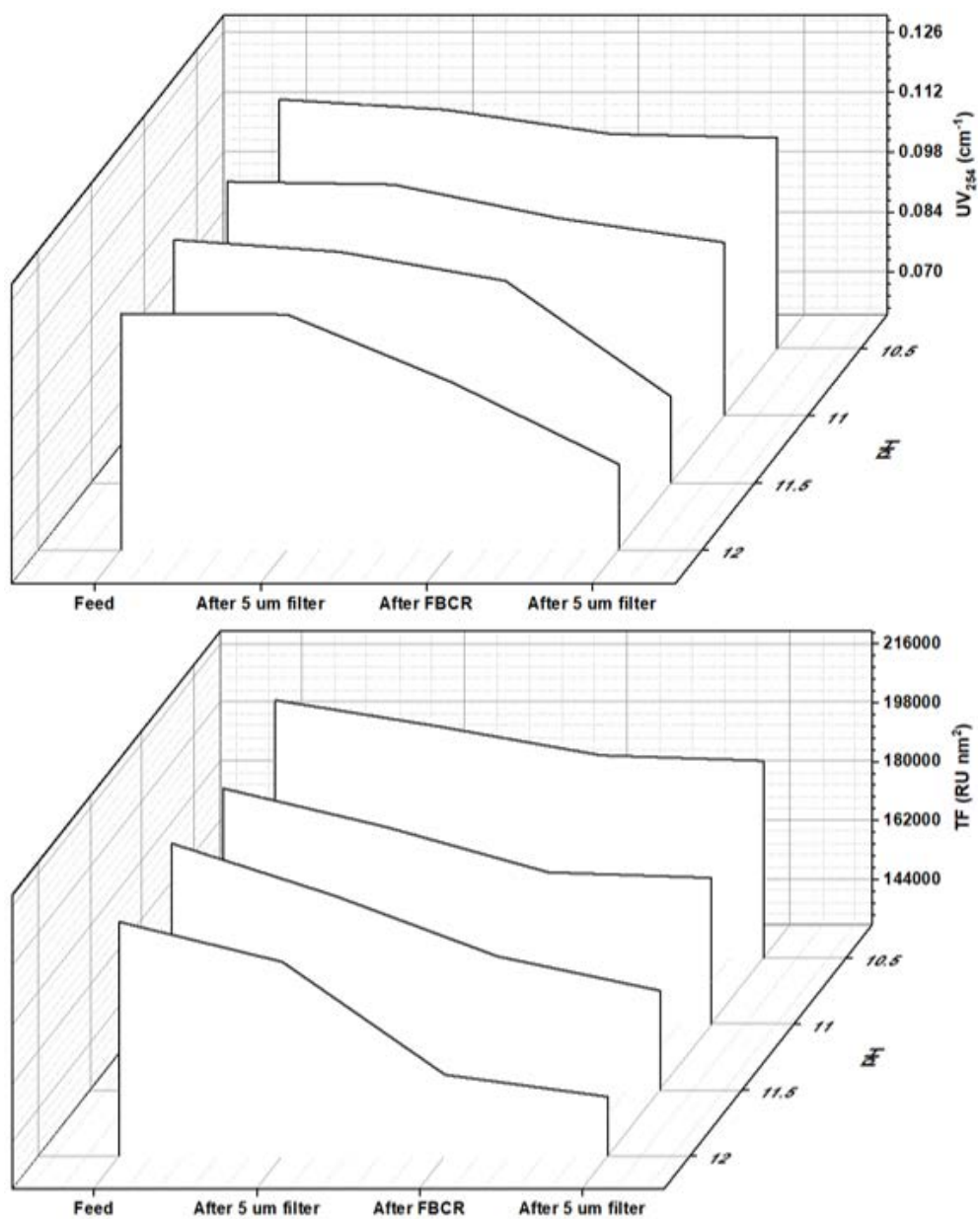


Figure S4 UV₂₅₄ and TF values for FBCR at four pH values.

REFERENCES

2015. Philippine Statistics Authority. <https://psa.gov.ph/content/2015-psa-annual-report>
- Aghdam, M.A., Zraick, F., Simon, J., Farrell, J., Snyder, S.A., 2016. A novel brine precipitation process for higher water recovery. *Desalination* 385, 69-74. 10.1016/j.desal.2016.02.007
- Artaxo, P., Gerab, F., Yamasoe, M.A., Martins, J.V., 1994. Fine Mode Aerosol Composition at 3 Long-Term Atmospheric Monitoring Sites in the Amazon Basin. *J Geophys Res-Atmos* 99, 22857-22868. <https://doi.org/10.1029/94jd01023>
- Baghoth, S.A., Sharma, S.K., Amy, G.L., 2011. Tracking natural organic matter (NOM) in a drinking water treatment plant using fluorescence excitation-emission matrices and PARAFAC. *Water Res* 45, 797-809. 10.1016/j.watres.2010.09.005
- Bagtasa, G., Cayetano, M.G., Yuan, C.S., 2018. Seasonal variation and chemical characterization of PM_{2.5} in northwestern Philippines. *Atmos Chem Phys* 18, 4965-4980. <https://doi.org/10.5194/acp-18-4965-2018>
- Becagli, S., Proposito, M., Benassai, S., Gragnani, R., Magand, O., Traversi, R., Udisti, R., 2005. Spatial distribution of biogenic sulphur compounds (MSA, nssSO₄(2-)) in the northern Victoria Land-Dome C-Wilkes Land, area, East Antarctica. *Ann Glaciol* 41, 23-31. Doi 10.3189/172756405781813384
- Bellouin, N., Quaas, J., Morcrette, J.J., Boucher, O., 2013. Estimates of aerosol radiative forcing from the MACC re-analysis. *Atmos Chem Phys* 13, 2045-2062. <https://doi.org/10.5194/acp-13-2045-2013>
- Benner, R., 2002. *Biogeochemistry of Marine Dissolved Organic Matter*, 2nd Edition.
- Boreddy, S.K.R., Kawamura, K., 2015. A 12-year observation of water-soluble ions in TSP aerosols collected at a remote marine location in the western North Pacific: an outflow region of Asian dust. *Atmos. Chem. Phys.* 15, 6437-6453. 10.5194/acp-15-6437-2015

Bowen, H.J.M., 1979. Environmental chemistry of the elements. Academic Press, London.

Braun, R.A., Dadashazar, H., MacDonald, A.B., Aldhaif, A.M., Maudlin, L.C., Crosbie, E., Aghdam, M.A., Mardi, A.H., Sorooshian, A., 2017. Impact of Wildfire Emissions on Chloride and Bromide Depletion in Marine Aerosol Particles. *Environ Sci Technol* 51, 9013-9021. <https://doi.org/10.1021/acs.est.7b02039>

Chameides, W.L., Stelson, A.W., 1992. Aqueous-Phase Chemical Processes in Deliquescent Sea-Salt Aerosols - a Mechanism That Couples the Atmospheric Cycles of S and Sea Salt. *J Geophys Res-Atmos* 97, 20565-20580. <https://doi.org/10.1029/92jd01923>

Chang, R.Y.W., Slowik, J.G., Shantz, N.C., Vlasenko, A., Liggio, J., Sjostedt, S.J., Leaitch, W.R., Abbatt, J.P.D., 2010. The hygroscopicity parameter (κ) of ambient organic aerosol at a field site subject to biogenic and anthropogenic influences: relationship to degree of aerosol oxidation. *Atmos Chem Phys* 10, 5047-5064. <https://doi.org/10.5194/acp-10-5047-2010>

Chen, W., Westerhoff, P., Leenheer, J.A., Booksh, K., 2003. Fluorescence excitation - Emission matrix regional integration to quantify spectra for dissolved organic matter. *Environ Sci Technol* 37, 5701-5710. DOI 10.1021/es034354c

Chi, J.W., Li, W.J., Zhang, D.Z., Zhang, J.C., Lin, Y.T., Shen, X.J., Sun, J.Y., Chen, J.M., Zhang, X.Y., Zhang, Y.M., Wang, W.X., 2015. Sea salt aerosols as a reactive surface for inorganic and organic acidic gases in the Arctic troposphere. *Atmos Chem Phys* 15, 11341-11353. 10.5194/acp-15-11341-2015

China, S., Burrows, S.M., Wang, B., Harder, T.H., Weis, J., Tanarhte, M., Rizzo, L.V., Brito, J., Cirino, G.G., Ma, P.-L., Cliff, J., Artaxo, P., Gilles, M.K., Laskin, A., 2018. Fungal spores as a source of sodium salt particles in the Amazon basin. *Nat Commun* 9, 4793. <https://doi.org/10.1038/s41467-018-07066-4>

Coble, P.G., 1996. Characterization of marine and terrestrial DOM in seawater using excitation emission matrix spectroscopy. *Mar Chem* 51, 325-346. Doi 10.1016/0304-4203(95)00062-3

Coble, P.G., Del Castillo, C.E., Avril, B., 1998. Distribution and optical properties of CDOM in the Arabian Sea during the 1995 Southwest Monsoon. *Deep-Sea Res Pt II* 45, 2195-2223. Doi [10.1016/S0967-0645\(98\)00068-X](https://doi.org/10.1016/S0967-0645(98)00068-X)

Cohen, D.D., Stelcer, E., Santos, F.L., Prior, M., Thompson, C., Pabroa, P.C.B., 2009. Fingerprinting and source apportionment of fine particle pollution in Manila by IBA and PMF techniques: A 7-year study. *X-Ray Spectrom* 38, 18-25.
<https://doi.org/10.1002/xrs.1112>

Cruz, F.T., Narisma, G.T., Villafuerte, M.Q., Chua, K.U.C., Olaguera, L.M., 2013. A climatological analysis of the southwest monsoon rainfall in the Philippines. *Atmos Res* 122, 609-616. <https://doi.org/10.1016/j.atmosres.2012.06.010>

Cruz, M.T., Bañaga, P.A., Betito, G., Braun, R.A., Stahl, C., Aghdam, M.A., Cambaliza, M.O., Dadashazar, H., Hilario, M.R., Lorenzo, G.R., Ma, L., MacDonald, A.B., Pabroa, P.C., Yee, J.R., Simpas, J.B., Sorooshian, A., 2019. Size-resolved Composition and Morphology of Particulate Matter During the Southwest Monsoon in Metro Manila, Philippines. *Atmos. Chem. Phys. Discuss.* in review. <https://doi.org/10.5194/acp-2019-270>

Dadashazar, H., Ma, L., Sorooshian, A., 2019. Sources of pollution and interrelationships between aerosol and precipitation chemistry at a central California site. *Sci Total Environ* 651, 1776-1787.
<https://doi.org/10.1016/j.scitotenv.2018.10.086>

Dong, H.Y., Gao, B.Y., Yue, Q.Y., Wang, Y., Li, Q., 2015. Effect of pH on floc properties and membrane fouling in coagulation - Ultrafiltration process with ferric chloride and polyferric chloride. *Chemosphere* 130, 90-97.
[10.1016/j.chemosphere.2015.03.049](https://doi.org/10.1016/j.chemosphere.2015.03.049)

Dusek, U., Frank, G.P., Curtius, J., Drewnick, F., Schneider, J., Kurten, A., Rose, D., Andreae, M.O., Borrmann, S., Poschl, U., 2010. Enhanced organic mass fraction and decreased hygroscopicity of cloud condensation nuclei (CCN) during new particle formation events. *Geophys Res Lett* 37.
<https://doi.org/10.1029/2009GL040930>

Farren, N.J., Dunmore, R.E., Mead, M.I., Nadzir, M.S.M., Abu Samah, A., Phang, S.M., Bandy, B.J., Sturges, W.T., Hamilton, J.F., 2019. Chemical characterisation of water-soluble ions in atmospheric particulate matter on the east coast of Peninsular Malaysia. *Atmos Chem Phys* 19, 1537-1553.

<https://doi.org/10.5194/acp-19-1537-2019>

Gerrity, D., Pecson, B., Trussell, R.S., Trussell, R.R., 2013. Potable reuse treatment trains throughout the world. *J Water Supply Res T* 62, 321-338. 10.2166/aqua.2013.041

Gerwe, C.E., 2003. Natural Organic Matter Adsorption Onto and Coprecipitation With Solids Formed During Softening, Civil, Architectural, and Environmental Engineering. University of Texas, Austin.

Graveland, A., Vandijk, J.C., Demoel, P.J., Oomen, J.H.C.M., 1983. Developments in Water Softening by Means of Pellet Reactors. *J Am Water Works Ass* 75, 619-625.

Gysel, M., Crosier, J., Topping, D.O., Whitehead, J.D., Bower, K.N., Cubison, M.J., Williams, P.I., Flynn, M.J., McFiggans, G.B., Coe, H., 2007. Closure study between chemical composition and hygroscopic growth of aerosol particles during TORCH2. *Atmos Chem Phys* 7, 6131-6144. <https://doi.org/10.5194/acp-7-6131-2007>

Harms, W.D., Robinson, R.B., 1992. Softening by Fluidized-Bed Crystallizers. *J Environ Eng-Asce* 118, 513-529. Doi 10.1061/(Asce)0733-9372(1992)118:4(513)

Hersey, S.P., Craven, J.S., Metcalf, A.R., Lin, J., Lathem, T., Suski, K.J., Cahill, J.F., Duong, H.T., Sorooshian, A., Jonsson, H.H., Shiraiwa, M., Zuend, A., Nenes, A., Prather, K.A., Flagan, R.C., Seinfeld, J.H., 2013. Composition and hygroscopicity of the Los Angeles Aerosol: CalNex. *J Geophys Res-Atmos* 118, 3016-3036. <https://doi.org/10.1002/jgrd.50307>

Ho, J.S., Ma, Z., Qin, J.J., Sim, S.H., Toh, C.S., 2015. In line coagulation-ultrafiltration as the pretreatment for reverse osmosis brine treatment and recovery. *Desalination* 365, 242-249. 10.1016/j.desal.2015.03.018

Hoffman, R.C., Laskin, A., Finlayson-Pitts, B.J., 2004. Sodium nitrate particles: physical and chemical properties during hydration and dehydration, and implications for aged sea salt aerosols. *J Aerosol Sci* 35, 869-887.

<https://doi.org/10.1016/j.jaerosci.2004.02.003>

Hong, Y., Hsu, K.L., Sorooshian, S., Gao, X.G., 2004. Precipitation Estimation from Remotely Sensed Imagery using an Artificial Neural Network Cloud Classification System. *J Appl Meteorol* 43, 1834-1852.

<https://doi.org/10.1175/Jam2173.1>

Hsu, S.-C., Liu, S.C., Kao, S.-J., Jeng, W.-L., Huang, Y.-T., Tseng, C.-M., Tsai, F., Tu, J.-Y., Yang, Y., 2007. Water-soluble species in the marine aerosol from the northern South China Sea: High chloride depletion related to air pollution. *Journal of Geophysical Research: Atmospheres* 112. <https://doi.org/10.1029/2007jd008844>

Hudson, P.K., Murphy, D.M., Cziczo, D.J., Thomson, D.S., de Gouw, J.A., Warneke, C., Holloway, J., Jost, H.-J., Hübner, G., 2004. Biomass-burning particle measurements: Characteristic composition and chemical processing. *J. Geophys. Res.* 109. <https://doi.org/10.1029/2003jd004398>

Ishida, K.P., Cooper, W.J., 2015. Analysis of Parameters Affecting Process Efficiency, Energy Consumption, and Carbon Footprint in Water Reuse. WateReuse Research Foundation.

Kerminen, V.M., Teinila, K., Hillamo, R., Pakkanen, T., 1998. Substitution of chloride in sea-salt particles by inorganic and organic anions. *J Aerosol Sci* 29, 929-942. [https://doi.org/10.1016/S0021-8502\(98\)00002-0](https://doi.org/10.1016/S0021-8502(98)00002-0)

Lakowicz, J.R., 2013. Principles of Fluorescence Spectroscopy. Springer Science & Business Media.

Laskin, A., Iedema, M.J., Cowin, J.P., 2002. Quantitative time-resolved monitoring of nitrate formation in sea salt particles using a CCSEM/EDX single particle analysis. *Environ Sci Technol* 36, 4948-4955. <https://doi.org/10.1021/es020551k>

Laskin, A., Moffet, R.C., Gilles, M.K., Fast, J.D., Zaveri, R.A., Wang, B., Nigge, P., Shutthanandan, J., 2012. Tropospheric chemistry of internally mixed sea salt

and organic particles: Surprising reactivity of NaCl with weak organic acids.

Journal of Geophysical Research: Atmospheres 117.

<https://doi.org/10.1029/2012jd017743>

Lawaetz, A.J., Stedmon, C.A., 2009. Fluorescence Intensity Calibration Using the Raman Scatter Peak of Water. Appl Spectrosc 63, 936-940. Doi 10.1366/000370209788964548

Lee, Y.-N., Weber, R., Ma, Y., Orsini, D., Maxwell-Meier, K., Blake, D., Meinardi, S., Sachse, G., Harward, C., Chen, T.-Y., Thornton, D., Tu, F.-H., Bandy, A., 2003. Airborne measurement of inorganic ionic components of fine aerosol particles using the particle-into-liquid sampler coupled to ion chromatography technique during ACE-Asia and TRACE-P. Journal of Geophysical Research: Atmospheres 108. <https://doi.org/10.1029/2002jd003265>

Lewis, E., Schwartz, S., 2004. Sea Salt Aerosol Production: Mechanisms, Methods, Measurements, and Models—A Critical Review. <https://doi.org/10.1029/GM152>

Li, X., Song, S., Zhou, W., Hao, J., Worsnop, D.R., Jiang, J., 2019. Interactions between aerosol organic components and liquid water content during haze episodes in Beijing. Atmos. Chem. Phys. Discuss. in review. <https://doi.org/10.5194/acp-2019-316>

Liao, H., Chen, W.-T., Seinfeld, J.H., 2006. Role of climate change in global predictions of future tropospheric ozone and aerosols. Journal of Geophysical Research: Atmospheres 111. <https://doi.org/10.1029/2005jd006852>

Liao, M.Y., Randtke, S.J., 1985. Removing Fulvic-Acid by Lime Softening. J Am Water Works Ass 77, 78-88.

Lynch, P., Reid, J.S., Westphal, D.L., Zhang, J.L., Hogan, T.F., Hyer, E.J., Curtis, C.A., Hegg, D.A., Shi, Y.X., Campbell, J.R., Rubin, J.I., Sessions, W.R., Turk, F.J., Walker, A.L., 2016. An 11-year global gridded aerosol optical thickness reanalysis (v1.0) for atmospheric and climate sciences. Geosci Model Dev 9, 1489-1522. <https://doi.org/10.5194/gmd-9-1489-2016>

Ma, L., Dadashazar, H., Braun, R.A., MacDonald, A.B., Aghdam, M.A., Maudlin, L.C., Sorooshian, A., 2019. Size-resolved characteristics of water-soluble particulate elements in a coastal area: Source identification, influence of wildfires, and diurnal variability. *Atmos Environ* 206, 72-84. <https://doi.org/10.1016/j.atmosenv.2019.02.045>

MacDonald, A.B., Dadashazar, H., Chuang, P.Y., Crosbie, E., Wang, H.L., Wang, Z., Jonsson, H.H., Flagan, R.C., Seinfeld, J.H., Sorooshian, A., 2018. Characteristic Vertical Profiles of Cloud Water Composition in Marine Stratocumulus Clouds and Relationships With Precipitation. *J Geophys Res-Atmos* 123, 3704-3723. <https://doi.org/10.1002/2017jd027900>

Marple, V., Olson, B., Romay, F., Hudak, G., Geerts, S.M., Lundgren, D., 2014. Second Generation Micro-Orifice Uniform Deposit Impactor, 120 MOUDI-II: Design, Evaluation, and Application to Long-Term Ambient Sampling. *Aerosol Sci Tech* 48, 427-433. <https://doi.org/10.1080/02786826.2014.884274>

Martens, C.S., Wesolowski, J.J., Harriss, R.C., Kaifer, R., 1973. Chlorine Loss from Puerto-Rican and San-Francisco-Bay Area Marine Aerosols. *J Geophys Res* 78, 8778-8792. <https://doi.org/10.1029/JC078i036p08778>

Maudlin, L.C., Wang, Z., Jonsson, H.H., Sorooshian, A., 2015. Impact of wildfires on size-resolved aerosol composition at a coastal California site. *Atmos Environ* 119, 59-68. <https://doi.org/10.1016/j.atmosenv.2015.08.039>

McInnes, L.M., Covert, D.S., Quinn, P.K., Germani, M.S., 1994. Measurements of Chloride Depletion and Sulfur Enrichment in Individual Sea-Salt Particles Collected from the Remote Marine Boundary-Layer. *J Geophys Res-Atmos* 99, 8257-8268. <https://doi.org/10.1029/93jd03453>

Miller, J.N., Miller, J.C., 2000. *Statistics and Chemometrics for Analytical Chemistry*. Prentice Hall.

Murphy, D.M., Froyd, K.D., Bian, H.S., Brock, C.A., Dibb, J.E., DiGangi, J.P., Diskin, G., Dollner, M., Kupc, A., Scheuer, E.M., Schill, G.P., Weinzierl, B., Williamson, C.J., Yu, P.F., 2019. The distribution of sea-salt aerosol in the global

troposphere. *Atmos Chem Phys* 19, 4093-4104. <https://doi.org/10.5194/acp-19-4093-2019>

Murphy, K.R., Stedmon, C.A., Waite, T.D., Ruiz, G.M., 2008. Distinguishing between terrestrial and autochthonous organic matter sources in marine environments using fluorescence spectroscopy. *Mar Chem* 108, 40-58.

10.1016/j.marchem.2007.10.003

Nguyen, P., Sellars, S., Thorstensen, A., Tao, Y.M., Ashouri, H., Braithwaite, D., Hsu, K.L., Sorooshian, S., 2014. Satellites track precipitation of Super Typhoon Haiyan, *Eos*, pp. 133-135. <https://doi.org/10.1002/2014EO160002>,

Nguyen, P., Shearer, E.J., Tran, H., Ombadi, M., Hayatbini, N., Palacios, T., Huynh, P., Braithwaite, D., Updegraff, G., Hsu, K., Kuligowski, B., Logan, W.S., Sorooshian, S., 2019. The CHRS Data Portal, an easily accessible public repository for PERSIANN global satellite precipitation data. *Sci Data* 6, 180296.

<https://doi.org/10.1038/sdata.2018.296>

Nriagu, J.O., 1989. A Global Assessment of Natural Sources of Atmospheric Trace-Metals. *Nature* 338, 47-49. <https://doi.org/10.1038/338047a0>

Park, M., Snyder, S.A., 2018. Sample handling and data processing for fluorescent excitation-emission matrix (EEM) of dissolved organic matter (DOM).

Chemosphere 193, 530-537. 10.1016/j.chemosphere.2017.11.069

Parkhurst, D.L., Appelo, C.A.J., 2013. Description of input and examples for PHREEQC version 3—a computer program for speciation, batch-reaction, one-dimensional transport, and inverse geochemical calculations. U.S. Geological Survey Techniques and Methods.

Pearce, G.K., 2008. UF/MF pre-treatment to RO in seawater and wastewater reuse applications: a comparison of energy costs. *Desalination* 222, 66-73.

10.1016/j.desal.2007.05.029

Petters, M.D., Kreidenweis, S.M., 2007. A single parameter representation of hygroscopic growth and cloud condensation nucleus activity. *Atmos Chem Phys* 7, 1961-1971. <https://doi.org/10.5194/acp-7-1961-2007>

Prabhakar, G., Sorooshian, A., Toffol, E., Arellano, A.F., Betterton, E.A., 2014. Spatiotemporal distribution of airborne particulate metals and metalloids in a populated arid region. *Atmos Environ* 92, 339-347.

<https://doi.org/10.1016/j.atmosenv.2014.04.044>

Quinn, P.K., Bates, T.S., Coffman, D.J., Miller, T.L., Johnson, J.E., Covert, D.S., Putaud, J.P., Neususs, C., Novakov, T., 2000. A comparison of aerosol chemical and optical properties from the 1st and 2nd Aerosol Characterization Experiments. *Tellus B* 52, 239-257. <https://doi.org/10.1034/j.1600-0889.2000.00033.x>

Racar, M., Dolar, D., Spehar, A., Kras, A., Kosutic, K., 2017. Optimization of coagulation with ferric chloride as a pretreatment for fouling reduction during nanofiltration of rendering plant secondary effluent. *Chemosphere* 181, 485-491. 10.1016/j.chemosphere.2017.04.108

Rahardianto, A., Gao, J.B., Gabelich, C.J., Williams, M.D., Cohen, Y., 2007. High recovery membrane desalting of low-salinity brackish water: Integration of accelerated precipitation softening with membrane RO. *J Membrane Sci* 289, 123-137. 10.1016/j.memsci.2006.11.043

Rahardianto, A., McCool, B.C., Cohen, Y., 2010. Accelerated desupersaturation of reverse osmosis concentrate by chemically-enhanced seeded precipitation. *Desalination* 264, 256-267. 10.1016/j.desal.2010.06.018

Randtke, S.J., Thiel, C.E., Liao, M.Y., Yamaya, C.N., 1982. Removing soluble organic contaminants by lime-softening. *Journal - American Water Works Association* 74, 192-202. 10.1002/j.1551-8833.1982.tb04888.x

Rolph, G., Stein, A., Stunder, B., 2017. Real-time Environmental Applications and Display system: READY. *Environ Modell Softw* 95, 210-228.

<https://doi.org/10.1016/j.envsoft.2017.06.025>

Russell, C.G., Lawler, D.F., Speitel, G.E., 2009. NOM coprecipitation with solids formed during softening. *J Am Water Works Ass* 101, 112-+.

Sahachaiyunta, P., Koo, T., Sheikholeslami, R., 2002. Effect of several inorganic species on silica fouling in RO membranes. *Desalination* 144, 373-378. Doi 10.1016/S0011-9164(02)00346-6

Sarang, B., Ramachandran, S., Rajesh, T.A., Dhaker, V.K., 2019. Black carbon linked aerosol hygroscopic growth: Size and mixing state are crucial. *Atmos Environ* 200, 110-118. <https://doi.org/10.1016/j.atmosenv.2018.12.001>

Seinfeld, J.H., Pandis, S.N., 2006. *Atmospheric chemistry and physics : from air pollution to climate change*, 2nd ed. Wiley, New York.

Service, R.F., 2006. Desalination freshens up. *Science* 313, 1088-1090. DOI 10.1126/science.313.5790.1088

Sheikholeslami, R., Tan, S., 1999. Effects of water quality on silica fouling of desalination plants. *Desalination* 126, 267-280. [https://doi.org/10.1016/S0011-9164\(99\)00182-4](https://doi.org/10.1016/S0011-9164(99)00182-4)

Shingler, T., Crosbie, E., Ortega, A., Shiraiwa, M., Zuend, A., Beyersdorf, A., Ziemba, L., Anderson, B., Thornhill, L., Perring, A.E., Schwarz, J.P., Campuzano-Jost, P., Day, D.A., Jimenez, J.L., Hair, J.W., Mikoviny, T., Wisthaler, A., Sorooshian, A., 2016. Airborne characterization of subsaturated aerosol hygroscopicity and dry refractive index from the surface to 6.5km during the SEAC(4)RS campaign. *J Geophys Res-Atmos* 121, 4188-4210. <https://doi.org/10.1002/2015jd024498>

Shinozuka, Y., Clarke, A.D., DeCarlo, P.F., Jimenez, J.L., Dunlea, E.J., Roberts, G.C., Tomlinson, J.M., Collins, D.R., Howell, S.G., Kapustin, V.N., McNaughton, C.S., Zhou, J., 2009. Aerosol optical properties relevant to regional remote sensing of CCN activity and links to their organic mass fraction: airborne observations over Central Mexico and the US West Coast during MILAGRO/INTEX-B. *Atmos Chem Phys* 9, 6727-6742. <https://doi.org/10.5194/acp-9-6727-2009>

Silva, P.J., Liu, D.Y., Noble, C.A., Prather, K.A., 1999. Size and chemical characterization of individual particles resulting from biomass burning of local

Southern California species. *Environ Sci Technol* 33, 3068-3076.

<https://doi.org/10.1021/es980544p>

Sluys, J.T.M., Verdoes, D., Hanemaaijer, J.H., 1996. Water treatment in a membrane-assisted crystallizer (MAC). *Desalination* 104, 135-139. Doi 10.1016/0011-9164(96)00036-7

Song, J.W., Zhao, Y., Zhang, Y.Y., Fu, P.Q., Zheng, L.S., Yuan, Q., Wang, S., Huang, X.F., Xu, W.H., Cao, Z.X., Gromov, S., Lai, S.C., 2018. Influence of biomass burning on atmospheric aerosols over the western South China Sea: Insights from ions, carbonaceous fractions and stable carbon isotope ratios. *Environ Pollut* 242, 1800-1809. <https://doi.org/10.1016/j.envpol.2018.07.088>

Sorooshian, A., Crosbie, E., Maudlin, L.C., Youn, J.S., Wang, Z., Shingler, T., Ortega, A.M., Hersey, S., Woods, R.K., 2015. Surface and airborne measurements of organosulfur and methanesulfonate over the western United States and coastal areas. *J Geophys Res-Atmos* 120, 8535-8548.

<https://doi.org/10.1002/2015jd023822>

Sorooshian, A., Wang, Z., Coggon, M.M., Jonsson, H.H., Ervens, B., 2013. Observations of Sharp Oxalate Reductions in Stratocumulus Clouds at Variable Altitudes: Organic Acid and Metal Measurements During the 2011 E-PEACE Campaign. *Environ Sci Technol* 47, 7747-7756. <https://doi.org/10.1021/es4012383>

Sorooshian, A., Wonaschütz, A., Jarjour, E.G., Hashimoto, B.I., Schichtel, B.A., Betterton, E.A., 2011. An aerosol climatology for a rapidly growing arid region (southern Arizona): Major aerosol species and remotely sensed aerosol properties. *J. Geophys. Res.* 116. <https://doi.org/10.1029/2011jd016197>

Stedmon, C.A., Markager, S., 2005a. Resolving the variability in dissolved organic matter fluorescence in a temperate estuary and its catchment using PARAFAC analysis. *Limnol Oceanogr* 50, 686-697. DOI 10.4319/lo.2005.50.2.0686

Stedmon, C.A., Markager, S., 2005b. Tracing the production and degradation of autochthonous fractions of dissolved organic matter by fluorescence analysis. *Limnol Oceanogr* 50, 1415-1426. DOI 10.4319/lo.2005.50.5.1415

Stedmon, C.A., Markager, S., Bro, R., 2003. Tracing dissolved organic matter in aquatic environments using a new approach to fluorescence spectroscopy. *Mar Chem* 82, 239-254. [10.1016/S0304-4203\(03\)00072-0](https://doi.org/10.1016/S0304-4203(03)00072-0)

Stein, A.F., Draxler, R.R., Rolph, G.D., Stunder, B.J.B., Cohen, M.D., Ngan, F., 2015. Noaa's Hysplit Atmospheric Transport and Dispersion Modeling System. *B Am Meteorol Soc* 96, 2059-2077. <https://doi.org/10.1175/Bams-D-14-00110.1>

Stokes, R.H., Robinson, R.A., 1966. Interactions in Aqueous Nonelectrolyte Solutions .I. Solute-Solvent Equilibria. *J Phys Chem-U.S* 70, 2126-&. <https://doi.org/10.1021/j100879a010>

van Pinxteren, M., Fiedler, B., van Pinxteren, D., Iinuma, Y., Kortzinger, A., Herrmann, H., 2015. Chemical characterization of sub-micrometer aerosol particles in the tropical Atlantic Ocean: marine and biomass burning influences. *J Atmos Chem* 72, 105-125. <https://doi.org/10.1007/s10874-015-9307-3>

Vanderveen, C., Graveland, A., 1988. Central Softening by Crystallization in a Fluidized-Bed Process. *J Am Water Works Ass* 80, 51-58.

Voutchkov, N., 2010. Considerations for selection of seawater filtration pretreatment system. *Desalination* 261, 354-364. [10.1016/j.desal.2010.07.002](https://doi.org/10.1016/j.desal.2010.07.002)

Voutchkov, N., 2017. Pretreatment for Reverse Osmosis Desalination. Elsevier.

Wonaschutz, A., Hersey, S.P., Sorooshian, A., Craven, J.S., Metcalf, A.R., Flagan, R.C., Seinfeld, J.H., 2011. Impact of a large wildfire on water-soluble organic aerosol in a major urban area: the 2009 Station Fire in Los Angeles County. *Atmos Chem Phys* 11, 8257-8270. <https://doi.org/10.5194/acp-11-8257-2011>

Yamashita, Y., Jaffe, R., 2008. Characterizing the interactions between trace metals and dissolved organic matter using excitation-emission matrix and parallel factor analysis. *Environ Sci Technol* 42, 7374-7379. [10.1021/es801357h](https://doi.org/10.1021/es801357h)

Ye, B., Ji, X., Yang, H., Yao, X., Chan, C.K., Cadle, S.H., Chan, T., Mulawa, P.A., 2003. Concentration and chemical composition of PM_{2.5} in Shanghai for a 1-year period. *Atmos Environ* 37, 499-510. [https://doi.org/10.1016/S1352-2310\(02\)00918-4](https://doi.org/10.1016/S1352-2310(02)00918-4)

- Zdanovskii, A.B., 1948. Novyi Metod Rascheta Rastvorimostei Elektrolitov V Mnogokomponentnykh Sistemakh .2. Zh Fiz Khim+ 22, 1486-1495.
- Zepp, R.G., Sheldon, W.M., Moran, M.A., 2004. Dissolved organic fluorophores in southeastern US coastal waters: correction method for eliminating Rayleigh and Raman scattering peaks in excitation-emission matrices. Mar Chem 89, 15-36.
10.1016/j.marchem.2004.02.006
- Zhang, Y., Zhang, H.H., Yang, G.P., Liu, Q.L., 2015. Chemical Characteristics and Source Analysis of Aerosol Composition over the Bohai Sea and the Yellow Sea in Spring and Autumn. J Atmos Sci 72, 3563-3573. <https://doi.org/10.1175/Jas-D-14-0372.1>
- Zhao, Y.L., Gao, Y., 2008. Acidic species and chloride depletion in coarse aerosol particles in the US east coast. Sci Total Environ 407, 541-547.
<https://doi.org/10.1016/j.scitotenv.2008.09.002>